Unravelling the collagen network of the arterial wall

Jan-Willem M. Beenakker

Stellingen

behorende bij het proefschrift
Unravelling the collagen network of the arterial wall

1. De verzwakking van de aortawand bij aneurysma's van de abdominale aorta is niet het gevolg van een verminderde collageen depositie, maar wel van een verstoorde organisatie van het collageen netwerk. Hoofdstuk 4 van dit proefschrift

2. Het enzym lysyl-oxidase, dat collageen fibers met elkaar verbindt, wordt geassocieerd met een stabieler phenotype van atherosclerotische plaques. Hoofdstuk 5 van dit proefschrift

3. Het effect van de inhoud van geactiveerde neurofielen op de mechanische eigenschappen van de extracellulaire matrix van de aortawand, suggereert dat neutrofielen lokaal de aorta wand dusdanig veranderen, dat dit op de lange termijn de organisatie en stabiliteit van het weefsel aantast. Hoofdstuk 7 van dit proefschrift

4. Voor het volledig doorgronden van veel ziektes aan het bindweefsel, is vaak een gedetailleerde studie naar de organisatie en eigenschappen van de extracellulaire matrix van het weefsel noodzakelijk. De atomaire krachtmicroscoop kan hieraan een waardevolle bijdrage leveren. Dit proefschrift

5. Hoewel diermodellen bijdragen aan het begrijpen van een ziektebeeld, is het noodzakelijk om de vindingen uit deze modellen te verifiëren in de kliniek, een stap die helaas vaak niet wordt gezet. A. Finn et al. Arterioscler. Thromb. Vasc. Biol (2010)
Ook: referentencommentaar bij weigering artikel: "Wij zien wat u beschrijft [over menselijk weefsel] niet terug bij onze muizen."

6. De huidige theoretische studies naar netwerken van biologische fibers, zoals een studie naar netwerken met verschillende soorten fibers, komen steeds dichter bij de opbouw van realistische weefsels. Het zou echter waardevol zijn als deze studies, die veelal het effect van schuifvervormingen op weefsels bestuderen, worden uitgebreid zodat deze ook voor indentatie experimenten bruikbaar worden. E. Huisman et al. Phys. Rev. Lett. (2010)

7. Hoewel de huidige klinische richtlijn, om een aneurysma te opereren indien zijn diameter groter is dan 5.5 cm, te simpel is, gaat eindige elementen analyse hier geen verbetering in aanbrengen, omdat de weefsel eigenschappen van aneurysma's onderling teveel verschillen en alleen invasief te bepalen zijn.
A. Maier et al. Ann. Biomed. Eng. (2010), M. Fillinger et al. J. Vasc. Surg. (2003)

8. Om het verschil in vasculaire remodelering bij atherosclerose, die in de abdominale aorta meestal naar buiten en bij de halsslagader meestal naar binnen is, te begrijpen, moet de stijfheid van het omliggende weefsel zeker meegenomen worden.

9. De huidige economische crisis is niet zozeer het resultaat van enkele morele misstanden aan de kant van financiele instellingen. Het is eerder het resultaat van de "financialisering" die in de jaren 70 begonnen is. Dit heeft uiteindelijk geleidt tot een misconceptie van waardecreatie door bedrijven en markten.
Toespraak van P.Y. Gomez; "Why we went into a depression" op het 6th Roman Symposium

Jan-Willem M. Beenakker
Leiden, 5 juni 2012

Unravelling the collagen network of the arterial wall

Unravelling the collagen network of the arterial wall

Proefschrift

ter verkrijging van
de graad van Doctor aan de Universiteit Leiden,
op gezag van Rector Magnificus prof. mr. P. F. van der Heijden,
volgens besluit van het College voor Promoties
te verdedigen op dinsdag 5 juni 2012
klokke 16:15 uur

door

Jan Willem Maria Beenakker

geboren te Leiden
in 1984

Promotiecommissie

Promotor:	Prof. dr. ir. T. H. Oosterkamp
Co-promotor:	Dr. J. H. Lindeman *(Leids Universitair Medisch Centrum)*
Overige leden:	Prof. dr. E. R. Eliel
	Prof. dr. P. Eriksson *(Karolinska Institutet, Zweden)*
	Prof. dr. J. W. M. Frenken
	Prof. dr. G. H. Koenderink *(Vrije Universiteit Amsterdam, AMOLF)*
	Dr. ir. S. J. T. van Noort
	Dr. C. Storm *(Technische Universiteit Eindhoven)*

Casimir PhD series, Delft-Leiden 2012-11 ISBN 978-90-8593-123-2

An electronic version of this thesis can be found at https://openaccess.leidenuniv.nl
The work described in this thesis was performed at the Huygens Laboratory, Leiden Institute of Physics, Leiden University, The Netherlands, and was financially supported by a Netherlands SmartMix grant and the NIMIC partner organizations.

ad majorem Dei gloriam

Contents

1 Introduction

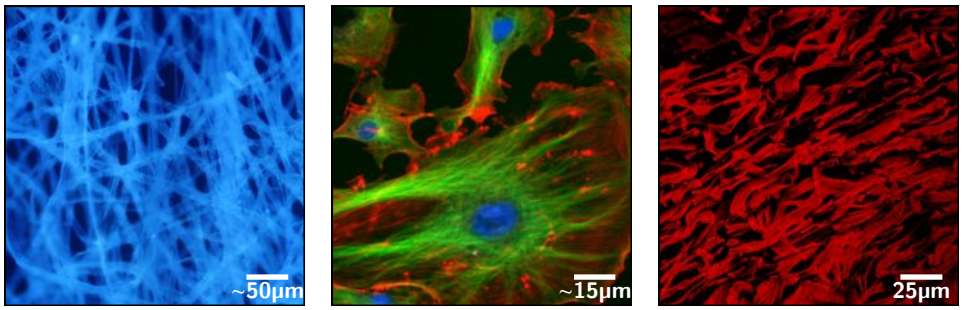

(a) Paper (b) Cell (c) Aortic wall

Figure 1.1:
(a) Network of moist fibers in paper illuminated by ultraviolet light.[1]
(b) The cytoskeletal network of endothelial cells. Actin filaments are shown in red, microtubules in green, and nuclei in blue.[1]
(c) Network of collagen fibers in the outer layer of the aortic wall.

Networks are all around us (see fig. 1.1). Our clothes are made out of a network of cotton fibers, the paper of this book is made out of a dense network of moist fibers, but also most of our organs are composed of a network of various fibers. The inner structure of cells is made of a network of microtubules, actin filaments and many other types of filaments. In addition to this intracellular network, the cells are embedded in a much larger network which determines the characteristics of the whole organ. A blood vessel, for example, is constructed from a network containing both stiff and flexible fibers, which together make it possible for the vessel wall to expand when the blood pressure increases, but prevent a stretch that would cause the vessel wall to weaken and eventually to rupture.

One of the remarkable properties of those networks is that by changing the way the fibers are interlaced, it is possible to make networks with different properties while using the same type of fiber. This property is much used for woven fabrics, where many different types of weaves have been developed. A few of those textile weaves are depicted in fig. 1.2. The plain weave is the most simple type of construction. In this type of fabric each weft yarn goes alternatively over and under the other warp yarn. The twill weave is similar to the plain weave, but allows for a more closely woven fabric. This makes the cloth heavier and stronger than plain weaves with the same type of fiber. The twill weave is also more resistant to wrinkles. The satin weave uses a minimum number of interfacings in the fabric, which results in a much softer and shinier fabric.

[1] The paper image is adopted from www.wikipedia.org and fluorescent image of a cell is taken from Molecular Probes. The scale bars in (a) and (b) are approximate.

(a) Damask tablecloth

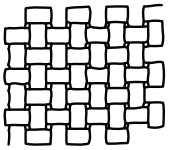

(b) Plain weave

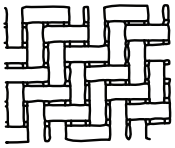

(c) Twill weave

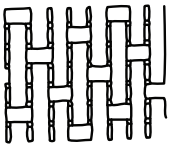

(d) Satin weave

Figure 1.2:
(a) Damask is a technique in which different weaving techniques are combined (right inset), with just one type of cotton fiber (left inset), to produce patterns.
(b,c,d) Various commonly used weaving patterns.

This method of producing materials with different properties but with the same type of fibers is also used in biology. During pregnancy and delivery, for example, the collagen network of the cervix, the lower part of the uterus, changes in such a way that the initial stiff tissue becomes soft, making it possible for the infant to be delivered. Such a network remodeling is, however, not alway advantageous. Scar tissue is, for example, the result of a highly disorganized collagen network, which results in a stiffer tissue that is much more vulnerable to rupture than the original skin.

In this thesis I look with the eye of a physicist at biological networks. I will use the physics of networks in order to gain a better understanding of the mechanics of tissues and how these mechanics are impaired in certain pathologies. I will do this by imaging these networks using various types of microscopy techniques and by measuring their mechanical response to deformation with the atomic force microscope. By combining the physical characteristics with clinical observations, I hope to gain a better understanding of the working of the tissue in general and, specifically, its mechanical properties.

2 Background

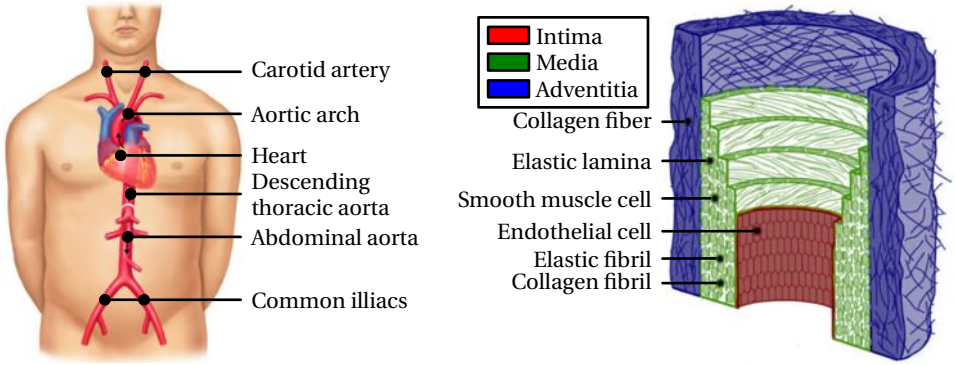

(a) Cardiovascular system (b) Aortic wall

Figure 2.1: Anatomy of the human cardiovascular system (a) and the aortic wall (b).[1]

2.1 The aorta

The aorta, the largest artery in the human body, originates from the left ventricle of the heart and extends down to the abdomen where it branches into two smaller arteries, the common iliacs. It is now well recognized that, beyond serving a conduit function, the aorta undertakes through its mechanical properties important roles in regulating left ventricular performance and the arterial function of the entire cardiovascular system.[2–4]

The mechanical properties of the aorta allow it to serve as an elastic reservoir.[5] The aorta expands with blood each time the heart contracts (systole) and then recoils elastically to continue the supply of blood to the small peripheral vessels while the heart is refilling (diastole). This phenomenon is often described by the windkessel model[6–8], but this model has been also criticized widely for being too simple and not useful to describe various diseased states.[4, 9, 10]

2.1.1 Anatomy of the aorta

The human aortic wall consists of three distinct layers, depicted in fig. 2.1b, which, together, give rise to its mechanical properties. The innermost layer, the tunica intima, consists of a thin layer of endothelial cells and is supported by the internal elastic lamina. These endothelial cells are in direct contact with the blood flow. The intima is particularly important in the disease of atherosclerosis (chapter 6).

The middle layer, the tunica media, is mainly composed of smooth muscle cells and elastin. The elastin is arranged into lamellae, between which collagen fibers,

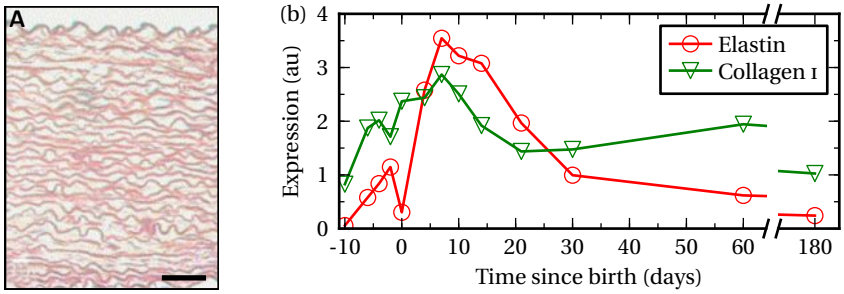

Figure 2.2:
(A) Circumferential section of the aortic wall showing the wavy elastin fibers (Verhoeff's elastica, scale bar is approximate 100 µm).[14]
(b) Collagen and elastin expression in the developing mouse aorta, showing a decrease in the elastin expression a few weeks after birth. Collagen, however, remains expressed during the whole lifespan.[15]

proteoglycans and smooth muscle cells are found. Thin elastic fibers connect the lamellae into a three-dimensional continuous network.[11, 12] Interestingly, the number of lamellae does not change after birth.[5]

The outermost layer of the vessel wall, the adventitia, starts next to the external elastic lamina. This layer consists of a collagen-rich extra cellular matrix and helps to prevent vascular rupture at extremely high pressures.[13] The adventitia of the aorta also contains the vasa vasorum, a network of small blood vessels that provide oxygen and nourishment to the cells in the vessel wall.

2.1.2 The extra cellular matrix of the aorta

The mechanical characteristics of blood vessels are determined by both active and passive components. The extra cellular matrix (ECM), a network composed mainly of collagen, elastin and proteoglycans, is responsible for the passive part, whereas smooth muscle cells are responsible for the active part. The macromolecules of the ECM are synthesized by three vascular cell types: intimal endothelial cells, medial smooth muscle cells and adventitial fibroblasts.

Elastin

In tissues where elastic recoil is necessary, elastic fibers consisting mainly of elastin are present in the extra cellular matrix. In the aorta, elastin constitutes as much as 40% of the total dry weight.[5, 16] Elastin is synthesized by the cells in the vessel wall as a soluble precursor molecule tropoelastin and is cross-linked by lysyl oxidase.[17] The elastic fibers of the aorta are composed of an elastin core

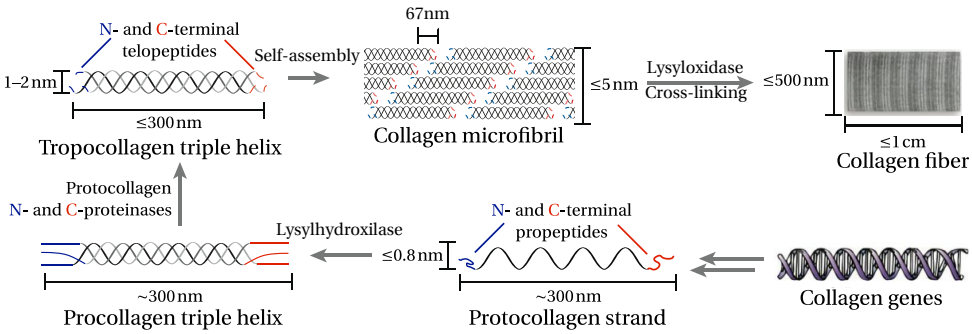

Figure 2.3: The assembly of collagen fibers.[23]

and are surrounded by a mantle of fibrillin-rich microfibrils.[18] Elastin contains a high number of cross-links per monomer, 15–20 compared to 1–4 cross-links per collagen monomer,[5] which is important for its recoil properties.

When the elastic lamellae in the aortic wall are unpressurised, they appear wavy in longitudinal and transverse sections, as is shown in fig. 2.2A. With increasing pressure and distention, there is a progressive straightening of the lamellae and the inter-lamellar distance decreases. At 10 kPa (75 mm Hg), the low end of the physiological pressure range, the lamellae are straight and give the appearance of regular concentric cylinders.[1]

The high degree of cross-linking is also responsible for the fibres longevity. Shapiro et al. showed, using ^{14}C turnover and aspartic acid racemization, that the elastin fibre is a metabolically stable unit over the human lifespan.[19] Other studies suggest that less than 1% of the total body elastin pool turns over in a year.[20]

In most tissues elastin expression occurs over a narrow window of development, starting in mid gestation and ending in the postnatal period,[21, 22] see fig. 2.2b. This explains the incomplete repair of elastin during adult life which is a key element in many diseases. The extensive loss of medial elastin, for example, is traditionally considered the hallmark of aneurysm formation, although it is now acknowledged that aneurysmal growth is also related to an impaired collagen homeostasis (see chapter 4).

Collagen

Collagen is the main constituent of the extra cellular matrix of animal connective tissues, compromising one-third of the total proteins in humans. In contrast to elastin, collagen fibers are rather stiff polymers.[24, 25] Currently twenty-eight different types of collagens have been identified.[26, 27] Collagen types I and III

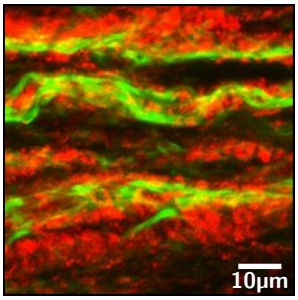

(a) Media

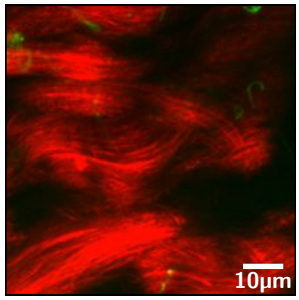

(b) Adventitia

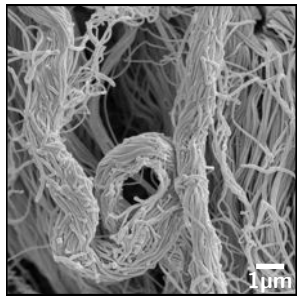

(c) SEM

Figure 2.4:
(a), (b) Multi-photon images of the porcine aortic wall showing the elastin (green) and collagen (red) fibers. In the media (a) the collagen fibers appear to be located around the elastin fibers, while they form a intertwined network in the adventita (b).
(c) SEM image of collagen fibers in the adventita of the human arterial wall shows a highly organized network (5.0 kV, 7000×).

are the major collagens in blood vessels, representing 60% and 30% of vascular collagens respectively.[28–30]

In vivo, individual collagen triple helices, known as tropocollagen, assemble in a complex, hierarchical manner that ultimately leads to the macroscopic fibers and networks observed in tissue, bone, and the vascular wall (fig. 2.3). This process is very dependent on the specific amino acids and a minor mutation can therefore already cause serious diseases such as the Ehlers-Danlos syndrome.[31, 32]

Collagen deposition in the medial layer is best characterized by small, interdispersed collagen fibrils that run mainly parallel to the main axis of the smooth muscle cells as well as to the streaks of elastin protruding from the elastic lamellae (fig. 2.4a).[12] Adventitial collagen, on the other hand, is arranged in a loose knitting of highly organized ribbon-like collagen bands that brace the medial and intimal layers of the vessel wall, fig. 2.4b. These different architectures appear optimal for realizing the different functionalities for the aortic medial and adventitial layers, elastic recoil and resilience, respectively.[33, 34] At physiological pressure, less than 10% of the collagen fibers are engaged, whereas at higher pressures, the vessel becomes progressively less distensible as more collagen fibers are being stretched.[35]

Proteoglycans

Proteoglycans are a group of diverse macromolecules that contain core proteins to which one or more glycosaminoglycans are covalently attached. The proteo-

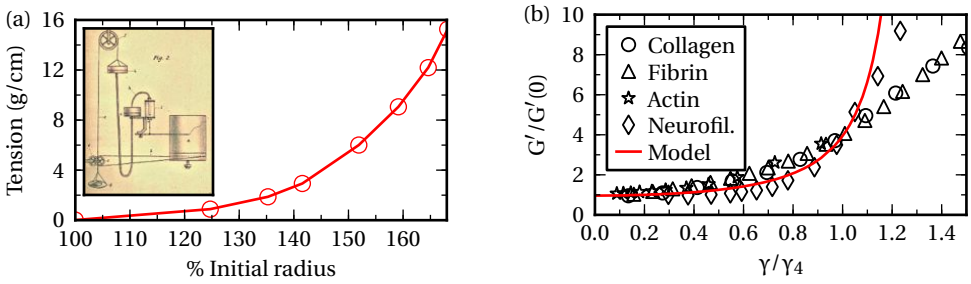

Figure 2.5:
(a) The mechanical response of the human iliac artery to inflation, showing its non-linear response to stress.[48]
(a inset) Schematic representation of the setup with which Charles Roy studied the elasticity of the aorta.[49] A detailed explanation of the setup can be found in ref. [1].
(b) Scaled modulus-strain curves for various biopolymer networks compared to model proposed by Storm et al. The shear moduli of the networks of collagen, fibrin, F-actin and neurofilaments are measured in a strain-controlled rheometer.[50]

glycans found in greatest abundance in the vessel wall can be categorized into two classes: large proteoglycans, that form an interconnected polymeric network by interactions with hyaluron, and small leucine-rich proteoglycans.[5] Electron microscopy and immunofluorescence studies strongly suggest the association of proteoglycans with specific regions of the banding pattern of collagen fibrils and also indicate that proteoglycans can form bridges between fibrils.[36–40]

Although proteoglycans constitute a minor component of vascular tissue (2% to 5% by dry weight),[41] they have an important influence on the mechanical properties of the tissue. Proteoglycans have a net negative charge under physiological conditions and produce a swelling stress which depends on the ionic strength of their environment.[42, 43] The inhomogenous distribution of proteoglycans across the vessel wall, showing a higher concentration in the intimal and medial layers than in the adventitia,[44, 45] gives rise to a residual stress in the aortic wall.[46, 47]

2.2 The physics of networks

One of the remarkable physical properties of many different types of biological tissues is its non-linear behavior under stress. The harder the tissue is strained, the stiffer it becomes. This strain-stiffening behavior allows for small deformations of tissues like the skin,[51] aorta[1] and blood clots,[52] but prevents large deformations that could threaten tissue integrity. The earliest quantitative study of vascular elasticity appears to be the work of Charles Roy (1881).[49] He con-

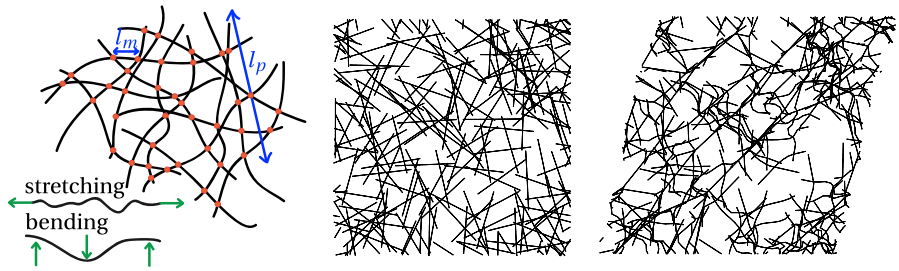

(a) Model (b) No strain (c) Large strain

Figure 2.6:
The model proposed by Onck et al., describes the network as fibers with a long persistence length, l_p, compared to the mesh size of the network, l_m, e.g. a network of collagen fibers. This renders the effect of entropic stiffening minimal compared to the penalty of bending, resulting in non-affine deformations of the network during strain. Images adopted from ref. [58, 59].

structed an ingenious gravity-driven apparatus, shown in the inset of fig. 2.5a, that performed in vitro inflation of blood vessel segments, measured instantaneous pressure and volume change, and plotted the resulting P – V curves to a rotating smoked-drum kymograph.

In recent years many different experimental and theoretical studies have shed a first light on the physical principles that determine the mechanical properties of tissues. Most experimental studies comprise of an in vitro system in which one or two different isolated components of the extra cellular matrix are combined to make a gel and reveal a rich interplay between fibers, linkers and cells.[53–55] Rheological measurements on, for example, reconstituted, collagen showed that these gels exhibit a similar strain-stiffening behavior as has been observed in vivo.[56, 57]

2.2.1 Theoretical models

Experimental observations such as the ones described in the previous section are the input of many different theoretical studies, which make an effort to explain the observed mechanical response. In 2005, C. Storm et al. proposed a model in which the force-response of networks is dominated by entropy.[50] In this model all the fibers react individually to the applied deformation. Because there are many curled-up configurations of a fiber and there is only one perfectly straight configuration, stretching a flexible filament reduces its conformational entropy and thus produces an opposing force.[50, 60–62] The collective non-linear behavior of this tissue model is due to the sum of nonlinear response of all the individual fibers.

The model proposed by Onck et al. argues that the entropic contributions to

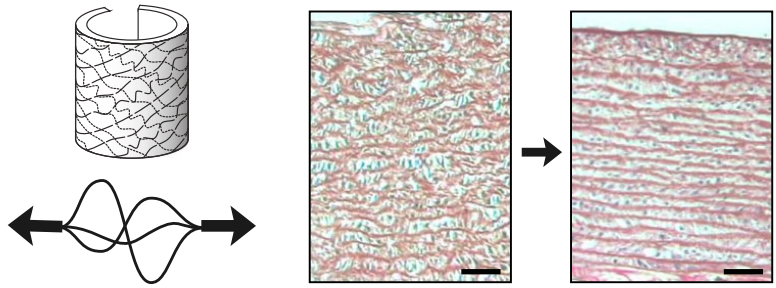

(a) Model (b) Input from histology

Figure 2.7:
The model proposed (a) by Fonk et al. describes the vessel wall as an elastic medium in which fibers of different lengths are embedded. As the vessel wall is stretched (b), the fibers are sequentially recruited which causes the stiffness of the tissue to increase. Many of the different parameters of this model are obtained from histological experiments. Scale bars are approximate 100µm. Images are adopted from ref. [14, 69].

the stiffness of the tissue are of minor importance compared to the nonaffine network rearrangements that occur during strain, fig. 2.6.[59] This model shows a strain-stiffening behavior can be the result of a transition from a bending-dominated response at small strains to a stretching-dominated response at higher strains.[58, 59, 63–65]

The long thermal persistence length of collagen fibers, ~1cm, compared to a typical cross-link spacing of ~2µm, renders the entropic stiffening effects in collagen gels to be minimal.[53] However, for other biopolymers such as actin, where the persistence length of the filaments is in the order of the distance between cross-links, entropic stiffening of the individual fibers is more likely to be an important component. Other recent studies have shown that the specific details of the individual cross-links also play an important role in the mechanics of the whole system.[53, 66–68] A system composed of randomly oriented rods connected by flexible cross-links, for example, already represents nonlinear network behavior.[66]

A theoretical model of the aortic wall

The models mentioned above describe the behavior of polymer gels composed of filaments and cross-links. These models predict the response measured in different in vitro systems, but these models still lack the complexity of real tissues in which not only many different components are present, but in which also the specific spatial organization of the different fibers greatly contributes to the mechanical response.[70, 71]

Another class of models, specifically developed for the vessel wall, describes the elastin fibers as an elastic reservoir in which collagen fibers of varying length are embedded.[14, 69, 71–77] As the stress increases, the collagen fibers are sequentially recruited causing an increasing stiffness of the tissue, as is illustrated in fig. 2.7. This model nicely fits the measured strain-stiffening of the arterial wall and has been used to study the effect of elastin degradation[74] and aging[73] on vessel mechanics. This mean-field approach, however, lacks the details of the interactions between the different components at the fiber level as is described by the earlier models and is therefor unable to describe the ECM remodeling occurring in many diseases.

2.3 The approach of this thesis

In this thesis we present our study of how the different components of the ECM determine the mechanical properties of the aortic wall and how they are related to different diseases. By this study we also hope to contribute to the process which is currently made to get a better understanding of the physics of tissues at the fiber level. We do this by locally probing the mechanical properties with the Atomic Force Microscope, while different optical techniques will be used to link these findings to the network structure of the tissue. The different techniques used in the thesis are described in chapter 3.

Aneurysms of the abdominal aorta

Aneurysms are localized dilatations of the vessel wall that are caused by a segmental weakening of the vessel wall, fig. 2.8a.[78, 79] Although aneurysms generally are without clinical symptoms, larger aneurysms may rupture, and bleeding from a ruptured aneurysm is responsible for more than 15,000 annual deaths in the United States alone.[80]

Aneurysm formation relates to defects in the extra cellular matrix resulting in attenuation and ultimate failure of the vessel wall.[81] Remarkably, although numerous studies have looked for putative quantitative changes in aortic collagen, results reported to date are controversial.[82–84] With the exception of rare mutations in the collagen III gene, such as the vascular type of Ehlers-Danlos syndrome, no clear association between impaired collagen homeostasis and aneurysm growth and/or rupture has been identified.

In this thesis the aortic wall of an healthy individual is compared to an aneurysm of the abdominal aorta (AAA) and to the aortic wall of a patient with the Marfan syndrome. The Marfan syndrome is a systemic disorder caused by mutations in the ECM protein fibrillin-1.[85–88] Fibrillin-1 microfibrils are thought

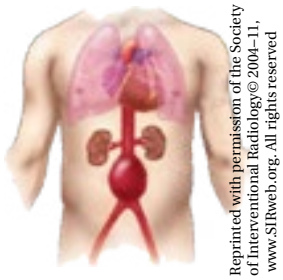

(a) AAA

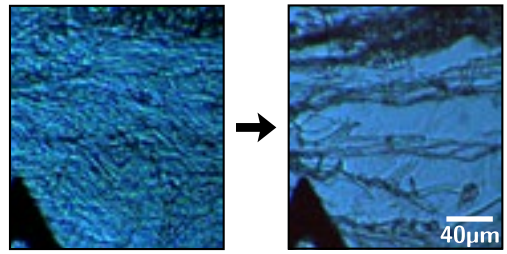

(b) Tissue digestions

Figure 2.8:
(a) An aneurysm of the abdominal aorta (AAA) is a localized dilatation of the arterial wall.[91]
(b) The effect of collagenase treatment on the adventitia of the arterial wall. In the lower left corner of the image the AFM cantilever, used for the mechanical probing, is visible.

to confer important biomechanical properties in connecting, anchoring and maintaining tissues and organs.[86] The clinical manifestations of Marfan are varied in range and involve many organs.[89] The majority of anomalies are found in the cardiovascular, respiratory, ocular and skeletal system. Aortic dilatation is the most common cause of morbidity and mortality under Marfan patients.[90]

In search of the collagen defect(s) underlying aneurysm formation, we applied an integrated approach of biochemical analyses, multiple imaging modalities, and mechanical analysis to identify the putative collagen defect in AAA and in Marfan syndrome. Results of this evaluation, chapter 4, show that advanced stages of aneurysmal disease are characterized by distinct defects in the network structure of adventitial collagen rather than by purely biochemical defects.

Proteolytic alterations of the arterial wall

The behaviour of cells is largely influenced by their surroundings.[92–94] While the biochemical interaction between cells and their environment has been widely studied in different systems, more recently different studies have shown the importance of the physical interaction of the cells with their surroundings, for example its mechanical properties. Fibroblastic cells, for example, spread less on a soft substrate[95] and have been observed to migrate toward stiffer substrates.[96]

Cells are not only able to respond to mechanical cues in their local environment, they are also able to change the mechanical properties of the same environment. The highly remodeled vessel wall of aneurysms, are, for example, linked with a highly elevated number of neutrophils.[97–99] One of the questions is whether the structural rearrangements of the aorta cause the inflammation or are a result of the inflammation.

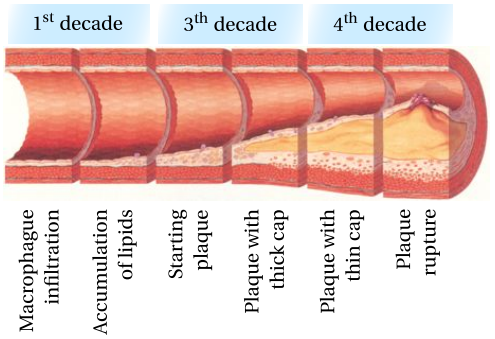

(a) Atherosclerosis

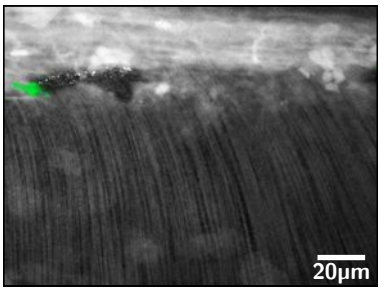

(b) Migrating neutrophil

Figure 2.9:
(a) The timeline of atherosclerosis starts with endothelial dysfunction which causes an inflammatory response due to the infiltration of lipids into the vessel wall. The onset of the disease already starts at the first decade, while its clinical manifestations start from the fourth decade.[100]
(b) Migrating neutrophils (green) alter the collagen network (white) in a zebrafish cancer model.

In chapter 5, we examine the effects of enzymatic digestion of the extra cellular matrix of the aortic wall, e.g. due to the contents of neutrophils, in order to better understand how cells change the mechanical properties of their environment. By starting with real tissue and selectively removing different elements, we are able to measure the contribution of the different constituents of the ECM to the mechanical properties of the whole tissue.

We do not only show that enzymatic treatment of the aortic wall greatly reduces its stiffness, but also that a simple treatment with the contents of neutrophils is able to mimic the in chapter 4 observed change in mechanical response from a healthy aorta to an aneurysm.

Atherosclerotic plaques

Atherosclerosis is a leading cause of death in the western world and is responsible for coronary heart disease, the majority of strokes and limb ischemia.[101] In atherosclerosis, cholesterol and components of the immune system accumulate in the vessel wall. Although luminal narrowing by such an atherosclerotic plaque contributes to some of the clinical manifestations, it is the rupture of such a plaque, followed by the formation of a blood clot, that causes the most acute and serious clinical manifestations of this disease.[102, 103]

Atherosclerosis typically starts in early adolescence and is usually found in most major arteries. Figure 2.9a schematically show the progression of the disease. The main cause of atherosclerosis is still a topic of many studies, but

the common thought is that the process is initiated by the infiltration of LDL cholesterol in the vessel wall due to endothelial dysfunction.[104] The presence of these lipids in the vessel wall leads to an inflammatory response, triggering macrophages to enter the vessel wall. The macrophages absorb the lipids, but are not able to process them, and will eventually rupture. This results in a greater amount of inflammatory signals, triggering the recruitment of more macrophages, continuing the cycle.

The contents of the ruptured macrophages are highly thrombogenic and contain many ECM degrading enzymes.[101, 105] The blood is protected from this so called necrotic core by a thick layer of collagen, which is secreted by smooth muscle cells. During the progression of the disease, the collagen cap gets thinner by the loss of the collagen producing smooth muscle cells on the one hand, and the ECM degrading enzymes inside the core on the other. A plaque with such a thin collagen cap can eventually rupture, bringing the highly thrombogenic core into contact with the blood. This triggers the formation of a thrombus (blood clot), which can block the blood supply and give rise to many lethal complications.[101, 103, 105, 106]

The combination of an altered ECM synthesis and degradation in the collagen cap leads to a remodeling of the collagen network, which affects the mechanical stability of the plaque.[105] Lysyl oxidase (LOX) is an extracellular enzyme that catalyzes the cross-linking of collagen fibrils, which results in the stabilization of extracellular collagen.[107, 108] In chapter 6 we show that higher LOX MRNA and protein levels are associated with a more stable phenotype of atherosclerotic plaques. This suggests that by promoting collagen cross-linking and the formation of thick collagen fibers with high tensile strength or an increased resistance to degradation by enzymes in the core, LOX may reduce the risk for plaque rupture and the development of lethal complications of atherosclerosis.

Migrating neutrophils in a zebrafish cancer model

The interactions between malignant tumor cells and their micro environment have a central role on tumor progression.[109, 110] The zebrafish, Danio rerio, has become an import animal model for cancer and immune research over the last decade.[111, 112] Many molecular and cellular components that operate during tumorigenesis are conserved between zebrafish and mammals.[113] The transparency of zebrafish, in combination with the availability of various tissue specific fluorescent reporter transgenic lines, allow for high resolution analysis of the tumor progression and the interactions between the tumor cells and the host microenvironment in vivo. Several tumor transplantation assays with human and mammalian cells have been developed to study different aspects of tumor

malignancies in embryo and adult zebrafish, such as tumor cell invasion.[114–117]

We have adopted the currently available multi-photon imaging techniques to be used on zebrafish. In chapter 7 we also present the results of a novel xenograft model that allows the visualization of all tumor development hallmarks. This new model elucidates how the transmigration of neutrophils remodels the collagen matrix, fig. 2.9b, and facilitates the invasion of tumor cells.

2.4 References

[1] R. E. Shadwick. Mechanical design in arteries. *J. Exp. Biol.*, 202:3305, 1999.

[2] D. P. Sokolis. Passive mechanical properties and structure of the aorta: segmental analysis. *Acta Physiol.*, 190:277, 2007.

[3] H. Boudoulas and C. F. Wooley. Aortic function. *J. Heart Valve Dis.*, 5 Suppl 3:S258, 1996.

[4] W. W. Nichols, M. F. O'Rourke, and C. Vlachopoulos. *McDonald's Blood Flow in Arteries, 6th ed: Theoretical, Experimental and Clinical Principles* (Hodder Arnold Publishers, 2011), 6 edition.

[5] J. E. Wagenseil and R. P. Mecham. Vascular Extracellular Matrix and Arterial Mechanics. *Physiol. Rev.*, 89:957, 2009.

[6] O. Frank. Der puls in den Arterien. *Zeitschrift für Biologie*, 45:441, 1905.

[7] P. B. Dobrin. Mechanical properties of arterises. *Physiol. Rev.*, 58:397, 1978.

[8] N. Westerhof, J.-W. Lankhaar, and B. E. Westerhof. The arterial Windkessel. *Med. Biol. Eng. Comp.*, 47:131, 2009.

[9] D. A. McDonald and M. G. Taylor. An investigation of the arterial system using a hydraulic oscillator. *J. Physiol. (Lond.)*, 133:74, 1956.

[10] G. Birkhoff. *Hydrodynamics* (Princeton: University Press, 1960).

[11] M. O'Connell, et al. The three-dimensional micro- and nanostructure of the aortic medial lamellar unit measured using 3D confocal and electron microscopy imaging. *Matrix Biol.*, 27:171, 2008.

[12] K. P. Dingemans, P. Teeling, J. H. Lagendijk, and A. E. Becker. Extracellular matrix of the human aortic media: an ultrastructural histochemical and immunohistochemical study of the adult aortic media. *Anat. Rec.*, 258:1, 2000.

[13] A. C. Burton. Relation of structure to function of the tissues of the wall of blood vessels. *Physiol. Rev.*, 34:619, 1954.

[14] D. P. Sokolis, et al. A structural basis for the aortic stress-strain relation in uniaxial tension. *J. Biomech.*, 39:1651, 2006.

[15] C. M. Kelleher, S. E. McLean, and R. P. Mecham. Vascular extracellular matrix and aortic development. *Curr. Top. Dev. Biol.*, 62:153, 2004.

[16] G. Hass. Method for the isolation of elastic tissues. *Arch. Patho.*, 34:807, 1942.

[17] S. Robins. Functional properties of collagen and elastin. *Baillière's Clinical Rheumatology*, 2:1, 1988.

[18] C. Kielty, M. Sherratt, and C. A. Shuttleworth. Elastic fibres. *J. Cell. Sci.*, 115:2817, 2002.

[19] S. D. Shapiro, et al. Marked longevity of human lung parenchymal elastic fibers deduced from prevalence of D-aspartate and nuclear weapons-related radiocarbon. *J. Clin. Invest.*, 87:1828, 1991.

[20] B. C. Starcher. Elastin and the lung. *Thorax*, 41:577, 1986.

[21] M. P. Bendeck, F. W. W. Keeley, and B. L. Langille. Perinatal accumulation of arterial wall constituents: relation to hemodynamic changes at birth. *Am. J. Physiol.*, 267:H2268, 1994.

[22] M. P. Bendeck and B. L. Langille. Rapid accumulation of elastin and collagen in the aortas of sheep in the immediate perinatal period. *Circ. res.*, 69:1165, 1991.

[23] M. D. Shoulders and R. T. Raines. Collagen structure and stability. *Annu. rev. biochem.*, 78:929, 2009.

[24] J. A. J. van der Rijt, et al. Micromechanical testing of individual collagen fibrils. *Macromol. Biosci.*, 6:697, 2006.

[25] L. Yang, et al. Mechanical properties of native and cross-linked type I collagen fibrils. *Biophys. J.*, 94:2204, 2008.

[26] J. Brinckmann. Collagens at a glance. *Top. Curr. Chem.*, 247:1, 2005.

[27] G. Veit, et al. Collagen XXVIII, a novel von Willebrand factor A domain-containing protein with many imperfections in the collagenous domain. *J. Biol. Chem.*, 281:3494, 2006.

[28] D. J. Prockop and K. I. Kivirikko. Collagens: molecular biology, diseases, and potentials for therapy. *Annu. rev. biochem.*, 64:403, 1995.

[29] M. van der Rest and R. Garrone. Collagen family of proteins. *FASEB J.*, 5:2814, 1991.

[30] R. Mayne. Collagenous proteins of blood vessels. *Arterioscler.*, 6:585, 1986.

[31] D. J. Prockop. What holds us together? Why do some of us fall apart? What can we do about it? *Matrix Biol.*, 16:519, 1998.

[32] F. Malfait and A. De Paepe. Molecular genetics in classic Ehlers-Danlos syndrome. *Am. J. Med. Genet. C. Semin. Med. Genet.*, 139C:17, 2005.

[33] P. B. Dobrin, W. H. Baker, and W. C. Gley. Elastolytic and collagenolytic studies of arteries. Implications for the mechanical properties of aneurysms. *Arch. surg.*, 119:405, 1984.

[34] T. Inahara. Eversion endarterectomy for aortoiliofemoral occlusive disease. A 16 year experience. *Am. J. Surg.*, 138:196, 1979.

[35] S. E. Greenwald, et al. Experimental investigation of the distribution of residual strains in the artery wall. *J. Biomech. Eng.*, 119:438, 1997.

[36] J. E. Scott. Proteoglycan: collagen interactions in connective tissues. Ultrastructural, biochemical, functional and evolutionary aspects. *Int. J. Biol. Macromol.*, 13:157, 1991.

[37] J. S. Bartholomew and J. C. Anderson. Investigation of relationships between collagens, elastin and proteoglycans in bovine thoracic aorta by immunofluorescence techniques. *Histochem. J.*, 15:1177, 1983.

[38] A. Serafini-Fracassini and P. Wells. *Studies on the interaction between glycosaminoglycans and fibrillar collagen*, volume 2 (Chemistry and Molecular Biology of the Intercellular Matrix, London, New York, 1970).

[39] R. Eisenstein and K. Kuettner. The ground substance of the arterial wall. Part 2. Electronmicroscopic studies. *Atheroscler.*, 24:37, 1976.

[40] D. B. Myers, T. C. Highton, and D. G. Rayns. Ruthenium red-positive filaments interconnecting collagen fibrils. *J. Ultrastruct. Res.*, 42:87, 1973.

[41] T. N. Wight. Cell biology of arterial proteoglycans. *Arterioscler.*, 9:1, 1989.

[42] W. M. Lai, J. S. Hou, and V. C. Mow. A Triphasic Theory for the Swelling and Deformation Behaviors of Articular Cartilage. *J. Biomech. Eng.*, 113:245, 1991.

[43] A. I. Maroudas. Balance between swelling pressure and collagen tension in normal and degenerate cartilage. *Nature*, 260:808, 1976.

[44] T. N. Wight. Vessel proteoglycans and thrombogenesis. *PNAS*, 5:1, 1980.

[45] L. Y. Yao, et al. Identification of the proteoglycan versican in aorta and smooth muscle cells by DNA sequence analysis, in situ hybridization and immunohistochemistry. *Matrix Biol.*,

14:213, 1994.

[46] X. Guo, Y. Lanir, and G. S. Kassab. Effect of osmolarity on the zero-stress state and mechanical properties of aorta. *Am. J. Physiol. Heart Circ. Physiol.*, 293:H2328, 2007.

[47] E. U. Azeloglu, et al. Heterogeneous transmural proteoglycan distribution provides a mechanism for regulating residual stresses in the aorta. *Am. J. Physiol. Heart Circ. Physiol.*, 294:H1197, 2008.

[48] M. R. Roach and A. C. Burton. The reason for the shape of the distensibility curves of arteries. *Can. J. Biochem. Physiol.*, 35:681, 1957.

[49] C. S. Roy. The Elastic Properties of the Arterial Wall. *J. Physiol. (Lond.)*, 3:125, 1881.

[50] C. Storm, et al. Nonlinear elasticity in biological gels. *Nature*, 435:191, 2005.

[51] C. H. Daly and G. F. Odland. Age-related changes in the mechanical properties of human skin. *J. Invest. Dermatol.*, 73:84, 1979.

[52] J. Shah and P. A. Janmey. Strain hardening of fibrin gels and plasma clots. *Rheol. Acta.*, 36:262, 1997.

[53] A. M. Stein, D. A. Vader, D. A. Weitz, and L. M. Sander. The Micromechanics of Three-Dimensional Collagen-I Gels. *Complexity*, 16:22, 2011.

[54] I. K. Piechocka, A. S. G. van Oosten, R. G. M. Breuls, and G. H. Koenderink. Rheology of heterotypic collagen networks. *Biomacromolecules*, 12:2797, 2011.

[55] F. Backouche, L. Haviv, D. Groswasser, and A. Bernheim-Groswasser. Active gels: dynamics of patterning and self-organization. *Phys. Biol*, 3:264, 2006.

[56] D. Aronson. Cross-linking of glycated collagen in the pathogenesis of arterial and myocardial stiffening of aging and diabetes. *J. Hypertens.*, 21:3, 2003.

[57] T. Sims, L. Rasmussen, H. Oxlund, and A. Bailey. The role of glycation cross-links in diabetic vascular stiffening. *Diabetologia*, 39:946, 1996.

[58] C. Heussinger, B. Schaefer, and E. Frey. Nonaffine rubber elasticity for stiff polymer networks. *Phys. Rev. E.*, 76:031906, 2007.

[59] P. R. Onck, T. Koeman, T. Van Dillen, and E. van der Giessen. Alternative explanation of stiffening in cross-linked semiflexible networks. *Phys. Rev. Lett.*, 95:178102, 2005.

[60] F. C. MacKintosh, J. Käs, and P. A. Janmey. Elasticity of semiflexible biopolymer networks. *Phys. Rev. Lett.*, 75:4425, 1995.

[61] E. M. Huisman, C. Storm, and G. T. Barkema. Frequency-dependent stiffening of semiflexible networks: a dynamical nonaffine to affine transition. *Phys. Rev. E.*, 82:061902, 2010.

[62] E. M. Huisman, C. Heussinger, C. Storm, and G. T. Barkema. Semiflexible filamentous composites. *Phys. Rev. Lett.*, 105:118101, 2010.

[63] E. M. Huisman, T. Van Dillen, P. R. Onck, and E. van der Giessen. Three-dimensional cross-linked F-actin networks: relation between network architecture and mechanical behavior. *Phys. Rev. Lett.*, 99:208103, 2007.

[64] T. Van Dillen, P. R. Onck, and E. van der Giessen. Models for stiffening in cross-linked biopolymer networks: A comparative study. *J. Mech. Phys. Solids*, 56:2240, 2008.

[65] C. P. Broedersz, M. Sheinman, and F. C. MacKintosh. Length-Controlled Elasticity in 3D Fiber Networks. *arXiv*, cond-mat.soft, 2011.

[66] C. P. Broedersz, C. Storm, and F. C. MacKintosh. Effective-medium approach for stiff polymer networks with flexible cross-links. *Phys. Rev. E.*, 79:061914, 2009.

[67] C. P. Broedersz, C. Storm, and F. C. MacKintosh. Nonlinear elasticity of composite networks of stiff biopolymers with flexible linkers. *Phys. Rev. Lett.*, 101:118103, 2008.

[68] M. L. Gardel, et al. Prestressed F-actin networks cross-linked by hinged filamins replicate mechanical properties of cells. *PNAS*, 103:1762, 2006.

[69] M. A. Zulliger, P. Fridez, K. Hayashi, and N. Stergiopulos. A strain energy function for arteries accounting for wall composition and structure. *J. Biomech.*, 37:989, 2004.

[70] M. Stolz, et al. Dynamic elastic modulus of porcine articular cartilage determined at two different levels of tissue organization by indentation-type atomic force microscopy. *Biophys. J.*, 86:3269, 2004.

[71] D. P. Sokolis. Passive mechanical properties and constitutive modeling of blood vessels in relation to microstructure. *Med. Biol. Eng. Comp.*, 46:1187, 2008.

[72] G. A. Holzapfel, T. C. Gasser, and R. W. Ogden. A new constitutive framework for arterial wall mechanics and a comparative study of material models. *J. Elasticity*, 61:1, 2000.

[73] M. A. Zulliger and N. Stergiopulos. Structural strain energy function applied to the ageing of the human aorta. *J. Biomech.*, 40:3061, 2007.

[74] E. Fonck, et al. Effect of elastin degradation on carotid wall mechanics as assessed by a constituent-based biomechanical model. *Am. J. Physiol. Heart Circ. Physiol.*, 292:H2754, 2007.

[75] M. A. Zulliger, A. Rachev, and N. Stergiopulos. A constitutive formulation of arterial mechanics including vascular smooth muscle tone. *Am. J. Physiol. Heart Circ. Physiol.*, 287:H1335, 2004.

[76] P. N. Watton, Y. Ventikos, and G. A. Holzapfel. Modelling the mechanical response of elastin for arterial tissue. *J. Biomech.*, 42:1320, 2009.

[77] D. P. Sokolis. A passive strain-energy function for elastic and muscular arteries: correlation of material parameters with histological data. *Med. Biol. Eng. Comp.*, 48:507, 2010.

[78] C. Crawford, K. Hurtgen-Grace, E. Talarico, and J. Marley. Abdominal aortic aneurysm: An illustrated narrative review. *J. Manip. Physiol. Ther.*, 26:184, 2003.

[79] D. A. Vorp. Biomechanics of abdominal aortic aneurysm. *J. Biomech.*, 40:1887, 2007.

[80] N. Sakalihasan, R. Limet, and O. Defawe. Abdominal aortic aneurysm. *Lancet*, 365:1577, 2005.

[81] R. W. Thompson, P. J. Geraghty, and J. Lee. Abdominal aortic aneurysms: Basic mechanisms and clinical implications. *Curr. Prob. Surg.*, 39:98, 2002.

[82] G. McGee, et al. Aneurysm or occlusive disease - factors determining the clinical course of atherosclerosis of the infrarenal aorta. *Surgery*, 110:370, 1991.

[83] R. J. Rizzo, et al. Collagen types and matrix protein content in human abdominal aortic aneurysms. *J. Vasc. Surg.*, 10:365, 1989.

[84] S. Menashi, J. S. Campa, R. M. Greenhalgh, and J. T. Powell. Collagen in abdominal aortic aneurysm: typing, content, and degradation. *J. Vasc. Surg.*, 6:578, 1987.

[85] A. B. Marfan. Un cas de déformation congénitale des quatre membres plus prononcée aux extremites caractérisée par l'allongement des os avec un certain degré d'amincissement. *Bull. Mêm. Soc. Méd. Hôp. Paris.*, 13:220, 1986.

[86] F. Ramirez. Fibrillin mutations in Marfan syndrome and related phenotypes. *Curr. Opin. Genet. Dev.*, 6:309, 1996.

[87] N. C. Y. Ho, J. R. Tran, and A. Bektas. Marfan's syndrome. *Lancet*, 366:1978, 2005.

[88] H. C. Dietz and R. E. Pyeritz. Mutations in the human gene for fibrillin-1 (FBN1) in the Marfan syndrome and related disorders. *Hum. Mol. Genet.*, 4 Spec No:1799, 1995.

[89] A. McBride and M. Gargan. Marfan syndrome. *Curr. Orthop.*, 20:418, 2006.

[90] G. J. Nollen and B. J. M. Mulder. What is new in the Marfan syndrome? *Int. J. Cardiol.*, 97 Suppl 1:103, 2004.

[91] Society of Interventional Radiology, http://www.SIRweb.org.

[92] E. Cukierman, R. Pankov, and K. M. Yamada. Cell interactions with three-dimensional ma-

trices. *Cur. op. cell biol.*, 14:633, 2002.

[93] P. M. Gilbert, et al. Substrate elasticity regulates skeletal muscle stem cell self-renewal in culture. *Science*, 329:1078, 2010.

[94] D. Discher, P. A. Janmey, and Y. Wang. Tissue cells feel and respond to the stiffness of their substrate. *Science*, 310:1139, 2005.

[95] R. J. Pelham and Y. l. Wang. Cell locomotion and focal adhesions are regulated by substrate flexibility. *PNAS*, 94:13661, 1997.

[96] C. M. Lo, H. B. Wang, M. Dembo, and Y. l. Wang. Cell movement is guided by the rigidity of the substrate. *Biophys. J.*, 79:144, 2000.

[97] J. R. Cohen, et al. Role of the neutrophil in abdominal aortic aneurysm development. *Cardiovasc. Surg.*, 1:373, 1993.

[98] M. B. Pagano, et al. Complement-dependent neutrophil recruitment is critical for the development of elastase-induced abdominal aortic aneurysm. *Circulation*, 119:1805, 2009.

[99] J. Eliason, et al. Neutrophil depletion inhibits experimental abdominal aortic aneurysm formation. *Circulation*, 112:232, 2005.

[100] C. J. Pepine. The effects of angiotensin-converting enzyme inhibition on endothelial dysfunction: potential role in myocardial ischemia. *Am. J. Cardiol.*, 82:23S, 1998.

[101] P. Shah. Mechanisms of plaque vulnerability and rupture. *J. Am. Coll. Card.*, 41:15S, 2003.

[102] V. Fuster, et al. Atherothrombosis and high-risk plaque: part I: evolving concepts. *J. Am. Coll. Card.*, 46:937, 2005.

[103] R. Virmani, et al. Lessons from sudden coronary death - A comprehensive morphological classification scheme for atherosclerotic lesions. *Arterioscler. Thromb. Vasc. Biol.*, 20:1262, 2000.

[104] K. J. Williams and I. Tabas. The response-to-retention hypothesis of early atherogenesis. *Arterioscler. Thromb. Vasc. Biol.*, 15:551, 1995.

[105] E. Adiguzel, P. Ahmad, C. Franco, and M. P. Bendeck. Collagens in the progression and complications of atherosclerosis. *Vasc. Med.*, 14:73, 2009.

[106] R. A. van Dijk, et al. The natural history of aortic atherosclerosis: A systematic histopathological evaluation of the peri-renal region. *Atheroscler.*, 210:100, 2010.

[107] D. Eyre, M. A. Paz, and P. Gallop. Cross-Linking in Collagen and Elastin. *Annu. rev. biochem.*, 53:717, 1984.

[108] H. A. Lucero and H. M. Kagan. Lysyl oxidase: an oxidative enzyme and effector of cell function. *Cell. Mol. Life Sci.*, 63:2304, 2006.

[109] A. Patenaude, J. Parker, and A. Karsan. Involvement of endothelial progenitor cells in tumor vascularization. *Microvasc. Res.*, 79:217, 2010.

[110] J. A. Joyce and J. W. Pollard. Microenvironmental regulation of metastasis. *Nat. Rev. Cancer*, 9:239, 2009.

[111] G. J. Lieschke and N. S. Trede. Fish immunology. *Curr. Biol.*, 19:R678, 2009.

[112] W. Goessling, T. E. North, and L. I. Zon. New waves of discovery: modeling cancer in zebrafish. *J. Clin. Oncol.*, 25:2473, 2007.

[113] L. I. Zon and R. T. Peterson. In vivo drug discovery in the zebrafish. *Nat. Rev. Drug Discov.*, 4:35, 2005.

[114] K. Stoletov, et al. Visualizing extravasation dynamics of metastatic tumor cells. *J. Cell. Sci.*, 123:2332, 2010.

[115] A. M. Taylor and L. I. Zon. Zebrafish tumor assays: the state of transplantation. *Zebrafish*, 6:339, 2009.

[116] S. Nicoli, D. Ribatti, F. Cotelli, and M. Presta. Mammalian tumor xenografts induce neovas-

cularization in zebrafish embryos. *Cancer Res.*, 67:2927, 2007.

[117] M. Haldi, C. Ton, W. L. Seng, and P. McGrath. Human melanoma cells transplanted into zebrafish proliferate, migrate, produce melanin, form masses and stimulate angiogenesis in zebrafish. *Angiogenesis*, 9:139, 2006.

3 Methods

In this thesis several different biological imaging techniques are used to image various collagen containing samples and to measure their mechanical properties. Table 3.1 shows an overview of the techniques used in this study with their specific features and characteristics.

In this chapter we will discuss AFM and fluorescence microscopy in relation to our experiments on collagen.

3.1 Atomic Force Microscopy

The Atomic Force Microscope[1] (AFM), a member of the more general class of Scanning Probe Microscopes, has become a valuable tool for biologists, physicists and chemists to perform a various number of measurements on the nano-scale. Since their invention in 1982 by Binnig and Rohrer,[2] Scanning Probe Microscopes have changed the modern natural sciences by contributing to major progress in the understanding of the structure and properties of condensed matter. The many different measurement techniques of the AFM and its ability to operate under aqueous conditions have made the AFM a popular tool in most of the natural sciences. The AFM has been used for high resolution imaging of material surfaces including, metals[3] and polymers,[4] but also of biological systems like DNA,[5, 6] proteins[7–9] and whole cells.[10, 11] Other applications of the AFM include nano manipulation,[12] friction measurements,[13] protein mapping[14, 15] and MRI imaging.[16] In this study the AFM is mainly used as a tool to perform nano-indentations.

3.1.1 The Atomic Force Microscope

The unique resolution of the AFM is based on an ultra-sharp tip, with a typical radius of 20 nm, which is attached to a flexible cantilever (fig. 3.1a). The cantilever is accurately moved with respect to the sample in x, y and z by ceramic piezoelements, which allow the sample to be scanned with sub-nanometer resolution while maintaining a constant force between the sample and the AFM tip (fig. 3.1b). The force between sample and tip is commonly determined by deflecting a laser beam of the end of the cantilever and measuring its deflection with a four-quadrant photodiode. Tip-sample interactions include electrostatic repulsion, van der Waals attraction, capillary and frictional forces.

The AFM used in this study, a Molecular Imaging Picoscan AFM, is mounted on a Zeiss Axiovert inverted microscope to allow for a precise selection of the scanned area, as is depicted in fig. 3.1c. The whole setup is put in an acoustic box to reduce acoustic and electronic noise on the one hand and to minimize the thermal drift on the other. A custom built heating and cooling system allows

Microscopy	Resolution limit	Specific features and characteristics
Light microscopy	~ 0.2 µm	Samples can be imaged in liquid or air. The resolution is limited by the wavelength of visible light.
Fluorescence microscopy	~ 0.2 µm	Samples can be imaged in liquid or air. Fluorescent labels are used to localize molecular components within the sample. Confocal microscopy further enables three-dimensional studies of the sample.
Scanning electron microscopy (SEM)	~ 5 nm	The sample placed is in a vacuum and is often coated, as the technique generally requires an electron conductive surface. An electron beam is used to probe the surface of the sample. Specific surface molecules can be labeled with heavy metals.
Atomic force microscopy (AFM)	~ 5 nm ~ 100 pN	Samples can be imaged in liquid or air. Imaging is accomplished by monitoring the position of a sharp tip, attached to a micro-cantilever, while it is scanned over the sample surface. The AFM provides a three-dimensional visualization of the sample surface and can also be used to measure the mechanical properties of the sample.

Table 3.1: Overview of characteristics of the main microscopy tools used in this study.

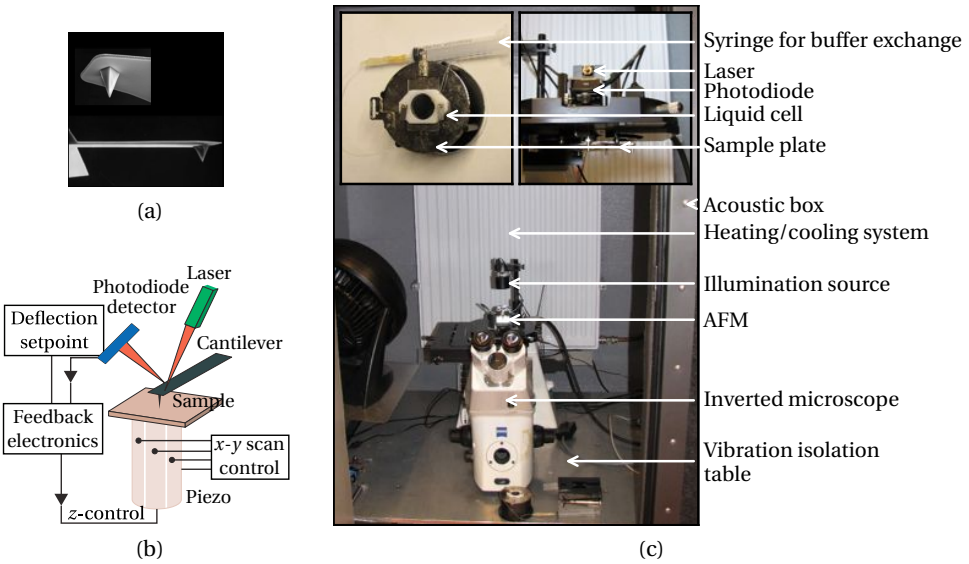

Figure 3.1:
(a) SEM image of an AFM cantilever (± 100 µm long) and an AFM tip (20 nm radius).
(b) Schematic representation of an AFM. A cantilever with a very sharp tip scans the sample, while the feedback electronics maintain a constant deflection of the cantilever.[17]
(c) The AFM, mounted on an inverted microscope, is put in an acoustic box to reduce the noise and thermal drift. A heating system is installed to control the temperature in the box.

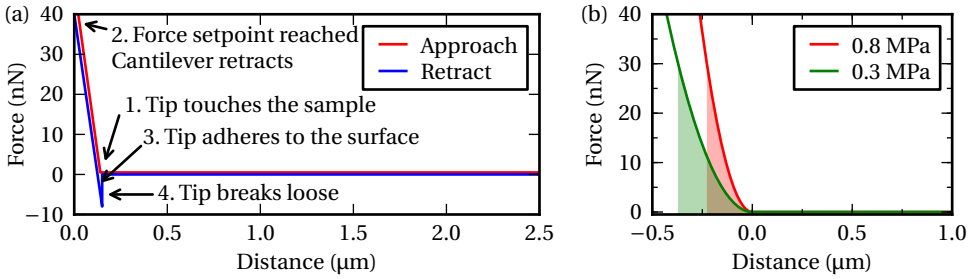

Figure 3.2:
(a) A typical force-distance curve made on glass. The cantilever approaches the surface until the force setpoint, 40 nN, is reached and retracts.
(b) Force-distance curves made on a stiff and a soft substrate by a conical indenter. The relative stiffness of the samples can be obtained by comparing the work needed to reach the same repulsive force (30 nN).

the temperature in the box to be set. A small fluid cell, clamped on the sample, facilitates measurements in aqueous conditions.

The AFM has been equipped with a break-out box, which gives access to the individual signals sent between the AFM scanner and its electronics. By sampling the deflection signal with a National Instruments acquisition card and controlling the AFM with a custom scripting program written in LabVIEW and Visual Basic 6, nano-indentation measurements are made with an enhanced resolution of approximately ten thousand points per indentation instead of a few hundred points.

3.1.2 Nano-indentation measurements

The AFM's ability to measure small forces, has made it a valuable instrument to measure the local mechanical properties of a wide range of samples.[18–21] By indenting the surface with the tip and measuring the force as a function of tip-sample distance, fig. 3.2, quantities such as sample stiffness, electrostatic interactions and adhesion forces can be measured.[17, 22–25]

In 1882, Heinrich Hertz modeled the indentation of a homogeneous sample with a spherical indenter.[26] This model, extended by Ian Sneddon for rotational symmetric indenters,[27] is commonly used to determine the Young's modulus, a measure of the sample stiffness, from a force-distance curve. The AFM tips used in this study can be approximated as a cone or a sphere, resulting in the

following relation between the force, F, and indentation, δ,

$$F_{cone} = \frac{\pi}{2}\frac{\tan(\alpha)E}{1-\nu}\delta^2 \tag{3.1}$$

$$F_{sphere} = \frac{4}{3}\frac{E\sqrt{R}}{1-\nu}\delta^{\frac{3}{2}}, \tag{3.2}$$

with E the Young's modulus and ν the Poisson ratio of the sample, α the opening angle of the cone and R the radius of the sphere.

A precise determination of the point of contact is necessary to apply the Hertz model to a force-distance curve. A small error in the determination of the point of contact due to the presence of a background signal and noise, often leads to a large error in the calculated stiffness. For rough and soft samples it can be difficult to control these errors, since forces at the moment of contact are often too small to give a measurable increase in the deflection signal. Optical distortions in tip-scanning AFM's tend to make these errors even larger (section 3.1.3). A-Hassan et al. developed a method, called FIEL (force integration to equal limits), to calculate the Young's modulus from a force-distance curve without the necessity to know the point of contact.[28]

By integrating the force, F, until a certain deformation, δ, the work needed for this deformation, W, is calculated: $W = \int_0^\delta F(z)dz$. This measure is directly related to the stiffness of the sample, as is illustrated in fig. 3.2b. Because the tip only starts to deflect when it indents the surface, there is no work performed until the point of contact. This allows the whole force-distance curve to be integrated, and removes the necessity to determine the point of contact. Rather, the problem is shifted to determining the zero of force. This error, however, is easier to control. By comparing the work needed with the work needed for the same deformation on a reference sample with a known stiffness, the stiffness of the sample can easily be calculated:

$$\frac{W_{sample}}{W_{calibration}} = \left(\frac{E_{calibration}}{E_{sample}}\right)^{\beta}, \tag{3.3}$$

with $\beta = \frac{1}{2}$ for a conical indenter and $\beta = \frac{3}{2}$ for a spherical indenter.

Ideally, this method of deriving the Young's modulus from a force-distance curve does not only remove the need to determine the point of contact, it also has several other advantages over fitting the Hertz model on the force-distance curve. Since the sensitivity of the system and the spring constant of the probe are the same in both measurements, they will divide out in equation 3.3, making it unnecessary to perform a calibration of the cantilever stiffness and to determine the optical lever sensitivity (which allows the bending of the cantilever to be

translated into the vertical deflection). This method is furthermore insensitive to small deviations in the tip geometry.

It proved, however, to be hard to produce a reference sample suitable to use as a comparison for measurements on the aortic wall. Various different types of reference samples with a stiffness similar to aortic tissue, 10^6 Pa,[29] have been tested, but they were either not stable over a longer period of time or were not suitable for AFM measurements, e.g. most synthetic polymers get sticky at low Young's moduli and thereby contaminate the cantilever. This calibration problem has been circumvented by modeling an indentation using equation 3.1 or 3.2. This method still allows for the whole force-distance curve to be integrated, but needs a precise calibration of the AFM setup and therefor lacks all the other advantages of the method proposed by A-Hassan et al. The spring constant, necessary to relate the cantilever deflection with the applied force, is calibrated with the Sader method[30] for rectangular cantilevers and with the thermal noise method[31–33] for triangular cantilevers.

The Hertz model describes the response of a homogenous and infinitely thick medium, whereas our samples have a finite thickness. By keeping the maximum indentation less than 10% of the sample thickness, the effect of supporting substrate turns out to be negligible.[34, 35] Hydrodynamic drag, caused by the surrounding buffer, could result in an extra loading force on the cantilever. The indentation rate is however chosen to be small enough, approximately 20 µm/s, to render the effects of hydrodynamic drag negligible.

The necessary condition of an isotropic, smooth substrate with a Young's modulus independent of the applied force, is however not met. Biological tissues tend to stiffen when they are deformed,[36, 37] and the many different types of fibers make the sample far from isotropic. However, by keeping the loading rate approximately constant amongst different experiments and using the same force-setpoint, the calculated values for the stiffness can still be used as a measure of the response of the tissue upon indentation. This "effective Young's modulus" will reflect the local mechanical properties of the tissue under the set experimental conditions and can be used to compare indentations on different types of tissue.

In this study we will indent the tissue on different equally spaced locations, e.g. a grid of 100 µm×100 µm containing 34 × 34 points. Such a measurement is often referred to as a force-volume measurement. By calculating the effective Young's modulus for every indentation a stiffness map of tissue is made, which can show local stiffness variations on the sub-micrometer level.

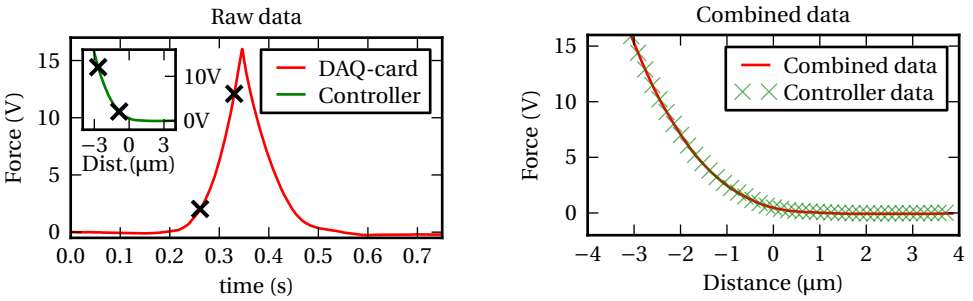

Figure 3.3:
Raw deflection data collected by the AFM controller and the DAQ-card. Two points, marked with an X, are used to correlate the DAQ-data to the data of the AFM controller and combine them into a force-distance curve with a higher resolution.

3.1.3 Data processing

Increase the time-resolution of indentation data

We use a National Instruments card controlled with a custom LabVIEW and Visual Basic script developed in the lab, to acquire force-distance curves with an enhanced time resolution. This resolution is needed because the increase of force can be very rapid and the AFM software only stores a limited number of data points per indentation. This enhancement is especially relevant for rough samples such as the human aorta, where the full piezo range in the z-direction is needed to indent the surface at different lateral positions.

The deflection versus time signal from the DAQ-card is transformed into a deflection versus piezo position dataset with a MATLAB script. This script determines the piezo position at two different indentation depths using the indentation data from the AFM-controller. By correlating these two indentation depths with the data from the DAQ-card, as is depicted in fig. 3.3, the piezo positions of the approach part of the force versus time data can be calculated by linear interpolation. Afterwards the χ^2 of the difference between the data from the AFM-controller and the high resolution force-distance curve is calculated to verify the accuracy of the new curve.

Correction for the beam-walk effect

In a tip scanning AFM, the laser, used to detect the deflection of the cantilever, is attached on top of a hollow piezo tube, which has a small lens at the bottom to focus the laser on the cantilever. A schematic drawing of the PicoSPM LE, a tip scanning AFM, is shown in fig. 3.4a. During a force-distance curve the distance

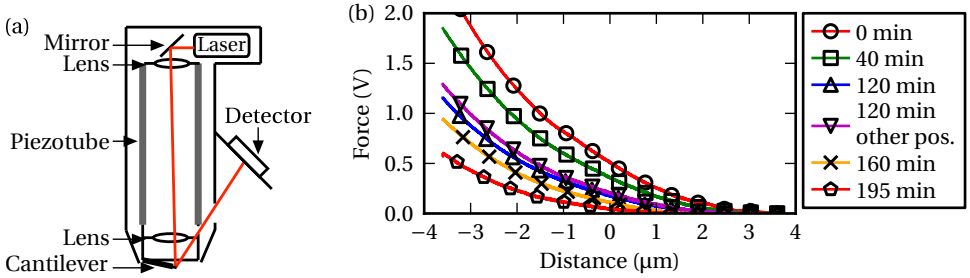

Figure 3.4:
(a) Schematic drawing of the PicoSPM LE, a tip scanning AFM. During a force-distance curve, the lens changes position, changing the deflection signal.
(b) Contact free force-distance curves made in liquid. Curves were measured at a variety of x, y positions and over an extended length of time.

between the laser and the lens changes slightly, which changes the laser spot and makes the beam move over the cantilever. This “beam-walk” effects produces a slight artifact in the apparent cantilever deflection.

Additionally, since all the tissues are measured under aqueous conditions, differences in condensation on the lens and other optics of the AFM make the beam-walk effect change over time. These optical effects change the deflection signal, making it seem as if the cantilever is experiencing a force, while in fact it is still far above the surface. This effect is illustrated in fig. 3.4b.

Initially, the functional form of the "beam-walk" effect was measured by making force-distance curves in liquid about one hundred microns above the surface. We find that the change of the deflection signal as a function of the piezo height can well be approximated by a second order polynomial.

As the optical effect changes with time and tip position, the parameters for the background correction need to be measured for each curve separately. A quadratic fit is made over the first 33% of the force-distance curve. This criterium proved to provide sufficiently many datapoints to give a good estimate of the background, without having the risk of using data where the tip is already in contact with the surface. The estimate of the "beam-walk" effect is improved by performing a median average of each fit with the fits from the adjacent force-distance curves.

This method of correcting force-distance curves is demonstrated by making a force-volume measurement on a piece of cartilage from a pig knee joint. Two typical force-distance curves before and after the correction are shown in fig. 3.5. The fitting correction reduces the artifact of apparent deflection to less than 1nm. The measured stiffness before and after correction differs up to 30%.

This correction also removes the systematic error that makes raised areas of

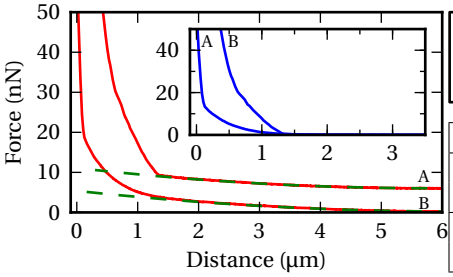

		Corrected	Uncorrected
A	Work	3.8 μm nN	6.2 μm nN
	Young's mod.	0.27 MPa	0.21 MPa
B	Work	2.1 μm nN	5.7 μm nN
	Young's mod.	0.36 MPa	0.22 MPa

Figure 3.5:
Corrected and uncorrected force-distance curves on pig cartilage. The "beam-walk" effect is measured by making a quadratic fit to the first 33% of the curve. Afterwards the fit is averaged with its adjacent fits and subtracted from the original force-distance curve. This reduces the artifact of apparent deflection to less than 1 nm and gives a correction to the measured stiffness in the order of 30%.

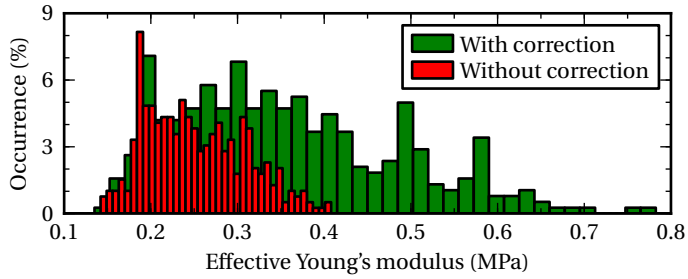

Figure 3.6:
Histogram of the measured stiffnesses on a piece of pig cartilage, before and after the background correction. The force-distance curves were made on a grid of 75 μm × 75 μm.

the sample appear stiffer than the lower areas. The lower areas of the tissue have a longer distance before the tip touches the sample. Since for the uncorrected curves the cantilever seems to be deflected before the point of contact, the total work done until the set force is reached seems to be higher. For rough samples, with height variations of several micrometers, this effect can dominate over the stiffness variations of the sample.

When all the force-distance curves made in one measurement are put together in one histogram, fig. 3.6, the significance of the correction is very clear. The optical artifact of the apparent deflection gives rise to an underestimation of the stiffness in the order of 30%. The fact that the magnitude of the error changes over time, makes the correction even more essential.

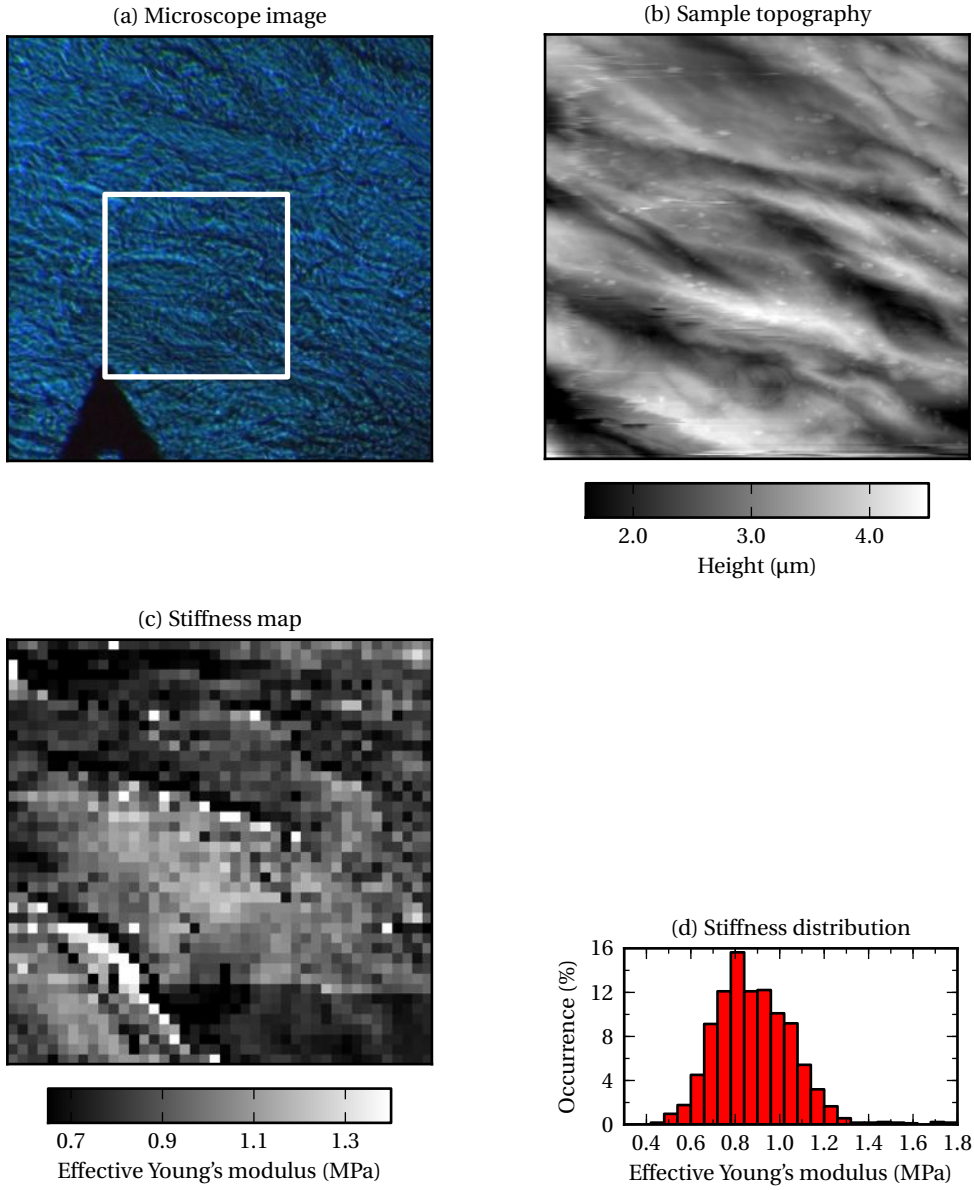

Figure 3.7:
Example measurement on a piece of porcine aortic wall. The inverted microscope is used to select the region (a) on which first the samples topography (b) is measured. The white square shows the area, 113 µm × 113 µm, which is being imaged with the AFM. Afterwards a force-volume measurement is made and the effective Young's modulus is calculated for every indentation (c). Stiffer, elongated, regions in the stiffness map tend to correlate with higher regions in the height image, which both have the same orientation as the fibers seen through the microscope. (d) Shows the distribution of the stiffnesses from the stiffness map (c).

3.1.4 Example dataset

The optical microscope is used to select the region to be measured, while two micrometer screws allow for a precise positioning of the sample in x and y. The microscope image clearly shows a network composed of different fibers. When the AFM is used to make a height image of the same region, as is shown in fig. 3.7b, the same fiber-like structure is measured. Afterwards, the tissue is indented on a regular grid of points and the effective Young's modulus is calculated for every indention, as is shown in fig. 3.7c. Stiffer regions in the stiffness map are elongated in the same direction as the fibers in the optical images and tend to correlate with higher regions in the height image, suggesting they might be collagen fibers. When all individual stiffness measurements are combined into a histogram, fig. 3.7d, the distribution of stiffnesses of the sample can be studied.

3.2 Fluorescence microscopy

In this study different forms of fluorescence microscopy are used to study the arrangement of fibers which make up the aortic wall and determine the mechanical properties of the tissue. In this type of microscopy the sample is illuminated with light of a specific wavelength which is being absorbed by the tissue and re-emitted at a longer wavelength. Most often this process takes place in fluorophores which are either attached to specific proteins, e.g. a Alexa488 anti-body, or are naturally present in the sample, e.g. elastin fibers have a high autofluorescence.

A special form of fluorescence microscopy is multi-photon microscopy in which multiple photons are absorbed after which one photon is emitted with the combined energy of the absorbed photons, as is illustrated in fig. 3.8b.

3.2.1 Confocal microscopy

In a conventional (wide-field) fluorescence microscope, the entire sample is evenly illuminated by a light source. All parts of the sample are excited at the same time and the resulting fluorescence, detected by the microscope's photodetector, includes a large unfocused background. In contrast, a confocal microscope uses point illumination together with a pinhole to eliminate out-of-focus signal, as is schematically illustrated in fig. 3.9a, and it thereby greatly increases the image's optical resolution, particularly in the z direction.

Tissues are made up of a complex three-dimensional network of fibers. By collecting a series of images with the focal plane at different heights, a three-dimensional view of this network can be constructed. 3D imaging of the tissue

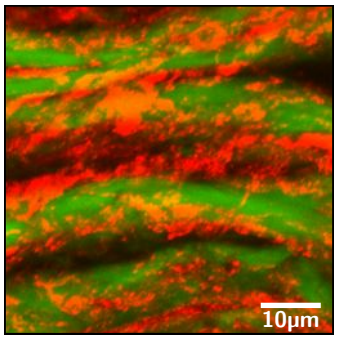

(a)

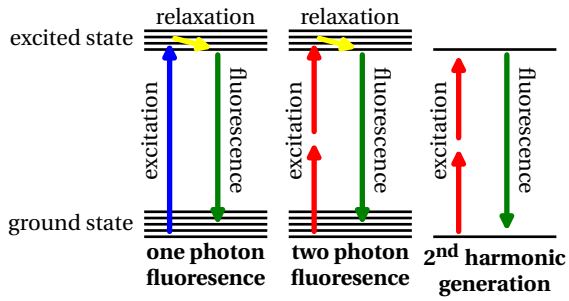

(b)

Figure 3.8:
(a) Fluorescence image of the aortic wall after it has been treated with enzymes which remove the proteoglycans, chapter 5. The collagen fibers (red) have been imaged using second-harmonic generation, while elastin (green) has been imaged using its two-photon autofluorescence.
(b) The basic principle of fluorescence microscopy. One or multiple photons are observed which bring an fluorphore into an excited state. When the fluorphore falls back to its ground state, it emits a photon.

not only gives a clear image of the organization of the different fibers, it also proved to be able to reveal structural changes in tissues which were hidden by conventional wide-field microscopy, fig. 3.9b,c.

In this study various different wide-field and confocal microscopes have been used. Tissues have been stained either chemically, e.g. with Pico Sirius Red, or with anti-bodies, to label different components of the vessel wall, e.g. collagen and hyaluron. Elastin has been imaged using its strong autofluorescence.

3.2.2 Multi-photon microscopy

Multi-photon microscopy is an imaging technique that relies on nonlinear light-matter interaction to provide high contrast and optical sectioning capabilities. The nonlinear signals which are responsible for forming the images are of two primary types: second-harmonic generation (SHG) and two-photon excited fluorescence (TPF).[38] Both types of nonlinear interactions occur naturally in biological tissues, enabling the imaging of tissues without the addition of exogenous contrast agents. Multi-photon microscopy has been widely used to image cells,[39, 40] tissues[41–44] and even unstained living specimens.[44–46]

In two-photon excited fluorescence (TPF), two photons of wavelength λ are absorbed to excite an electron to an excited state, fig. 3.8b.[47] Relaxation back to the ground state occurs through the emission of a photon having slightly less than the input energy (due to losses in the the transitions between the excited

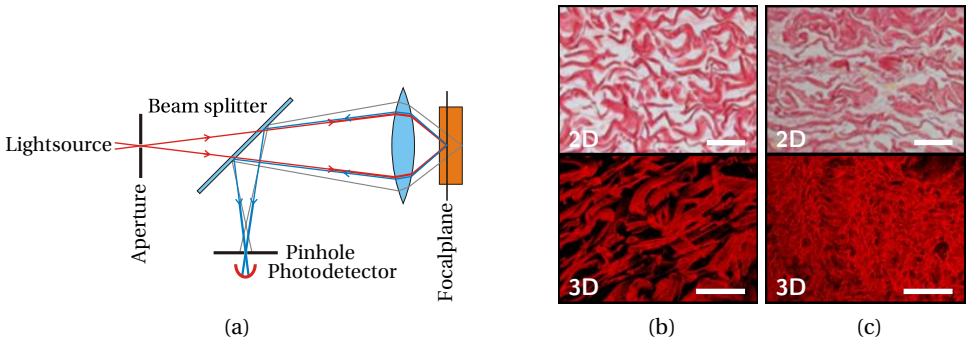

(a) (b) (c)

Figure 3.9:
(a) A confocal microscope uses a point illumination source together with a pinhole to eliminate the out-of-focus signal. This greatly increases the image's optical resolution, particularly in the z-direction.
(b), (c) Show a 2D and 3D image of the collagen structure of the adventitia of the abdominal aorta of a healthy individual (b) and a patient with Marfan syndrome (c). The 2D image is made with a bright field microscope, while the 3D image is a reconstruction made by projecting multiple optical sections taken by a confocal microscope. In the 3D image a clear difference in the network structure can be seen, while this remains largely hidden in the 2D image.
Scale bars: 30µm

states). This photon has a wavelength slightly greater than $\lambda/2$.

Second-harmonic generation, on the other hand, is primarily electronic in origin.[48] Two photons of the same wavelength "coalesce" to a virtual state within the specimen to form a single photon with an energy of exactly twice that of the incident photons, the emitted wavelength is $\lambda/2$. A detailed study on the electronic origin of this process shows that the intensity of the resulting signal strongly depends on the orientation, polarization and local symmetry properties of the molecule.[48]

Multi-photon microscopy has several advantages over one-photon confocal microscopy. The probability of two-photon absorption depends on the square of the intensity of the excitation light, and thereby only takes place in a very narrow volume at the focal point of the microscope. The maximum resolution is approximately 0.3µm in xy- and 0.9µm in z-direction, without the need of a pinhole.[49] Most tissues are transparent for near-infrared light, used in this type of microscopy, enhancing the depth penetration, eg. up to 250µm in rat aortas.[50] In addition, photobleaching and photodamage are drastically reduced.[49]

The chirality of the collagen molecule makes it a well known source of SHG, while the autofluorescence of elastin exhibits TPF.[41, 51] A study by Zoumi et al.[43] showed that both the collagen and the elastin can be excited at a wave-

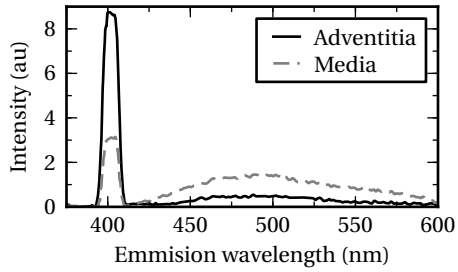

Figure 3.10:
Multi-photon emission spectra from a rabbit aortic wall excited at 800 nm showing the SHG peak of the collagen around 400 nm, and the broad TPF peak of elastin around 500 nm.[43]

length of 800 nm, fig. 3.10. By detecting the emitted light with a wavelength of 371 nm–425 nm for collagen and 471 nm–532 nm for elastin, both structures can be imaged simultaneously, fig. 3.8a. The multi-photon images were taken on a Zeiss 710 NLO upright confocal microscope equipped with a Spectra-Physics Deep See MP laser.

3.3 Sample preparation

All human arterial wall samples were provided by the Vascular Tissue Bank, Department of Vascular Surgery, Leiden, The Netherlands. Sample collection and handling was performed in accordance with the guidelines of Medical Ethical Committee of the Leiden University Medical Center and the code of conduct of the Dutch federation of Biomedical Scientific Societies.[52]

All aortic samples are cut to sections of approximately 1 cm thick, and are snap frozen within 24 hours after biopsy. Snap freezing is a method in which a small sample, a few mm^3, is quickly frozen by plunging it into liquid ethane (−183 °C). This freezing method prevents the formation of ice crystals which could damage the sample.

Afterwards the samples are cryosliced with a microtome (Leica CM3050S), and attached to Klinipath KP Plus microscope slides. Samples for AFM measurements and 2-photon imaging were cut to a thickness of 50 µm. This proved to be thick enough for the sample to remain intact in buffer for at least 24 hours. Samples used for (imuno)histochemistry were cut to a thickness of 5 µm, because thinner sections give less out of focus signal and chemical fixation would ensure that the sample remains intact. The samples are stored at −80 °C until use.

3.4 References

[1] G. Binnig and C. F. Quate. Atomic Force Microscope. *Phys. Rev. Lett.*, 56:930, 1986.

[2] G. Binnig and H. Rohrer. Scanning tunneling microscopy. *Surf. Sci.*, 126:236, 1983.

[3] F. Houze, R. Meyer, O. Schneegans, and L. Boyer. Imaging the local electrical properties of metal surfaces by atomic force microscopy with conducting probes. *Appl. Phys. Lett.*, 69:1975, 1996.

[4] S. N. Magonov, et al. Atomic force microscopy on polymers and polymer related compounds. *Polymer Bulletin*, 26:223, 1991.

[5] T. Thundat, D. P. Allison, R. J. Warmack, and T. L. Ferrell. Imaging Isolated Strands of Dna-Molecules by Atomic Force Microscopy. *Ultramicroscopy*, 42:1101, 1992.

[6] H. G. Hansma, et al. Reproducible imaging and dissection of plasmid DNA under liquid with the atomic force microscope. *Science*, 256:1180, 1992.

[7] P. Hallett, G. Offer, and M. J. Miles. Atomic force microscopy of the myosin molecule. *Biophys. J.*, 68:1604, 1995.

[8] Y. Lin, J. Wang, L.-J. Wan, and X.-H. Fang. Study of fibrinogen adsorption on self-assembled monolayers on Au(111) by atomic force microscopy. *Ultramicroscopy*, 105:129, 2005.

[9] M. Radmacher, et al. Imaging Adhesion Forces and Elasticity of Lysozyme Adsorbed on Mica with the Atomic-Force Microscope. *Langmuir*, 10:3809, 1994.

[10] M. Radmacher, R. W. Tillamnn, M. Fritz, and H. E. Gaub. From molecules to cells: imaging soft samples with the atomic force microscope. *Science*, 257:1900, 1992.

[11] H. Miyazaki and K. Hayashi. Atomic force microscopic measurement of the mechanical properties of intact endothelial cells in fresh arteries. *Med. Biol. Eng. Comp.*, 37:530, 1999.

[12] R. Resch, et al. Manipulation of gold nanoparticles in liquid environments using scanning force microscopy. *Ultramicroscopy*, 82:135, 2000.

[13] S. Park, K. D. Costa, and G. A. Ateshian. Microscale frictional response of bovine articular cartilage from atomic force microscopy. *J. Biomech.*, 37:1679, 2004.

[14] C. Stroh, et al. Single-molecule recognition imaging microscopy. *PNAS*, 101:12503, 2004.

[15] L. A. Chtcheglova, et al. Nano-Scale Dynamic Recognition Imaging on Vascular Endothelial Cells. *Biophys. J.*, 93:L11, 2007.

[16] C. L. Degen, et al. Nanoscale magnetic resonance imaging. *PNAS*, 106:1313, 2009.

[17] D. P. Allison, N. P. Mortensen, C. J. Sullivan, and M. J. Doktycz. Atomic force microscopy of biological samples. *Wiley Interdiscip Rev Nanomed Nanobiotechnol*, 2:618, 2010.

[18] C. Das, K. H. Sheik, P. D. Olmsted, and S. D. Connell. Nano-scale mechanical probing of supported lipid bilayers with atomic force microscopy. *arXiv*, physics.bio-ph, 2010.

[19] M. Salerno, S. Dante, N. Patra, and A. Diaspro. AFM Measurement of the Stiffness of Layers of Agarose Gel Patterned With Polylysine. *Microsc. Res. Techniq.*, 73:982, 2010.

[20] S. Kasas and G. Dietler. Probing nanomechanical properties from biomolecules to living cells. *Pflugers Arch.*, 456:13, 2008.

[21] M. M. J. F. Koenders, et al. Microscale mechanical properties of single elastic fibers: The role of fibrillin-microfibrils. *Biomaterials*, 30:2425, 2009.

[22] P. Grutter, D. Rugar, and H. J. Mamin. Magnetic force microscopy of magnetic materials. *Ultramicroscopy*, 47:393, 1992.

[23] A. Razatos, Y. L. Ong, M. M. Sharma, and G. Georgiou. Molecular determinants of bacterial adhesion monitored by atomic force microscopy. *PNAS*, 95:11059, 1998.

[24] C. Rotsch and M. Radmacher. Mapping local electrostatic forces with the atomic force microscope. *Langmuir*, 13:2825, 1997.

[25] G. Huber, S. N. Gorb, R. Spolenak, and E. Arzt. Resolving the nanoscale adhesion of individual gecko spatulae by atomic force microscopy. *Biol. Lett.*, 1:2, 2005.

[26] H. Hertz. Ueber die Berührung fester elastischer Körper. *Journal für die reine und angewandte Mathematik (Crelles Journal)*, 1882:156, 1882.

[27] I. N. Sneddon. The relation between load and penetration in the axisymmetric Boussinesq problem for a punch of arbitrary profile. *Int. J. Eng. Sci.*, 1965.

[28] E. A-Hassan, et al. Relative microelastic mapping of living cells by atomic force microscopy. *Biophys. J.*, 74:1564, 1998.

[29] J. H. N. Lindeman, et al. Distinct defects in collagen microarchitecture underlie vessel-wall failure in advanced abdominal aneurysms and aneurysms in Marfan syndrome. *PNAS*, 107:862, 2010.

[30] J. Sader, J. Pacifico, C. Green, and P. Mulvaney. General scaling law for stiffness measurement of small bodies with applications to the atomic force microscope. *J. Appl. Phys.*, 97:124903, 2005.

[31] H. J. Butt and M. Jaschke. Calculation of Thermal Noise in Atomic-Force Microscopy. *Nanotech.*, 6:1, 1995.

[32] R. Stark, T. Drobek, and W. Heckl. Thermomechanical noise of a free v-shaped cantilever for atomic-force microscopy. In *Ultramicroscopy*, 207–215 (Univ Munich, Inst Kristallog & Angew Mineral, D-80333 Munich, Germany, 2001).

[33] J. L. Hutter and J. Bechhoefer. Calibration of atomic-force microscope tips. *Rev. Sci. Instrum.*, 64:1868, 1993.

[34] H. Bueckle. Micro-Hardness Test and its Application. Berliner Union Verlag, Stuttgart, 1965.

[35] H. Bueckle. The science of hardness testing and its research applications. American Society for Metals, Ohio, 1973.

[36] I. K. Piechocka, A. S. G. van Oosten, R. G. M. Breuls, and G. H. Koenderink. Rheology of heterotypic collagen networks. *Biomacromolecules*, 12:2797, 2011.

[37] C. Storm, et al. Nonlinear elasticity in biological gels. *Nature*, 435:191, 2005.

[38] A. Zoumi, A. Yeh, and B. J. Tromberg. Imaging cells and extracellular matrix in vivo by using second-harmonic generation and two-photon excited fluorescence. *PNAS*, 99:11014, 2002.

[39] J. M. Squirrell, D. L. Wokosin, J. G. White, and B. D. Bavister. Long-term two-photon fluorescence imaging of mammalian embryos without compromising viability. *Nat. Biotechnol.*, 17:763, 1999.

[40] P. J. Campagnola, M. D. Wei, A. Lewis, and L. M. Loew. High-resolution nonlinear optical imaging of live cells by second harmonic generation. *Biophys. J.*, 77:3341, 1999.

[41] S. Roth and I. Freund. Optical second-harmonic scattering in rat-tail tendon. *Biopolymers*, 20:1271, 1981.

[42] T. Parasassi, et al. Two-photon microscopy of aorta fibers shows proteolysis induced by LDL hydroperoxides. *Free Radic. Biol. Med.*, 28:1589, 2000.

[43] A. Zoumi, X. Lu, G. Kassab, and B. Tromberg. Imaging coronary artery microstructure using second-harmonic and two-photon fluorescence microscopy. *Biophys. J.*, 87:2778, 2004.

[44] Y. Guo, et al. Second-harmonic tomography of tissues. *Opt. Lett.*, 22:1323, 1997.

[45] M. J. Levene, et al. In vivo multiphoton microscopy of deep brain tissue. *J. Neurophysiol.*, 91:1908, 2004.

[46] B. Masters, P. So, and E. Gratton. Multiphoton excitation fluorescence microscopy and spectroscopy of in vivo human skin. *Biophys. J.*, 72:2405, 1997.

[47] I. Freund, M. Deutsch, and A. Sprecher. Connective tissue polarity. Optical second-harmonic microscopy, crossed-beam summation, and small-angle scattering in rat-tail tendon. *Bio-*

phys. J., 50:693, 1986.

[48] R. Gauderon, P. B. Lukins, and C. J. Sheppard. Optimization of second-harmonic generation microscopy. *Micron*, 32:691, 2001.

[49] K. König. Multiphoton microscopy in life sciences. *J. Microsc*, 200:83, 2000.

[50] C. J. de Grauw, et al. Two-photon lifetime imaging of blood and blood vessels. *Proc. SPIE*, 4262:171, 2001.

[51] E. Georgiou, T. Theodossiou, and V. Hovhannisyan. Second and third optical harmonic generation in type I collagen, by nanosecond laser irradiation, over a broad spectral region. *Opt. Comm.*, 176:253, 2000.

[52] Code of conduct of the Dutch federation of Biomedical Scientific Societies, http://www.federa.org/?s=1&m=78&p=&v=4.

4 Defects in collagen organisation in abdominal aneurysms

This chapter has been published as:
Distinct defects in collagen microarchitecture underlie vessel-wall failure in advanced abdominal aneurysms and aneurysms in Marfan syndrome
J. H. N. Lindeman, B. A. Ashcroft, J. W. M. Beenakker, M. van Es, N. B. R. Koekkoek, F. A. Prins, J. F. Tielemans, H. Abdul-Hussien, R. A. Bank and T. H. Oosterkamp
Proceedings of the National Academy of Sciences 107:862, 2010

4.1 Abstract

An aneurysm of the aorta is a common pathology characterized by segmental weakening of the artery. Although it is generally accepted that the vessel-wall weakening is caused by an impaired collagen metabolism, a clear association has been demonstrated only for rare syndromes such as the vascular type Ehlers-Danlos syndrome. Here we show that vessel-wall failure in growing aneurysms of patients who have aortic abdominal aneurysm (AAA) or Marfan syndrome is not related to a collagen defect at the molecular level. On the contrary our findings indicate similar (Marfan) or even higher collagen concentrations (AAA) and increased collagen cross-linking in the aneurysms. Using 3D confocal imaging we show that the two conditions are associated with profound defects in collagen microarchitecture. Reconstructions of normal vessel wall show that adventitial collagen fibers are organized in a loose braiding of collagen ribbons. These ribbons encage the vessel, allowing the vessel to dilate easily but preventing overstretching. AAA and aneurysms in Marfan syndrome show dramatically altered collagen architectures with loss of the collagen knitting. Evaluations of the functional characteristics by atomic force microscopy showed that the wall has lost its ability to stretch easily and revealed a second defect: although vascular collagen in normal aortic wall behaves as a coherent network, in AAA and Marfan tissues it does not. As a result, mechanical forces loaded on individual fibers are not distributed over the tissue. These studies demonstrate that the mechanical properties of tissue are strongly influenced by collagen microarchitecture and that perturbations in the collagen networks may lead to mechanical failure.

4.2 Introduction

Aortic aneurysms are localized dilatations of the aortic wall that are caused by segmental weakening of the vessel wall. Although aneurysms generally are without clinical symptoms, larger aneurysms may rupture, and bleeding from a ruptured aneurysm is responsible for more than 15,000 annual deaths in the United States alone.[1]

Aneurysm formation relates to a primary or secondary (acquired) defect in the matrix structures supporting the vessel wall resulting in attenuation and ultimate failure of the vessel wall.[2] Although extensive loss of medial elastin traditionally is considered the hallmark of aneurysm formation, it now is acknowledged that aneurysmal growth and ultimate rupture relate to impaired collagen homeostasis.[2] Remarkably, although numerous studies have looked for putative quantitative changes in aortic collagen, results reported to date are

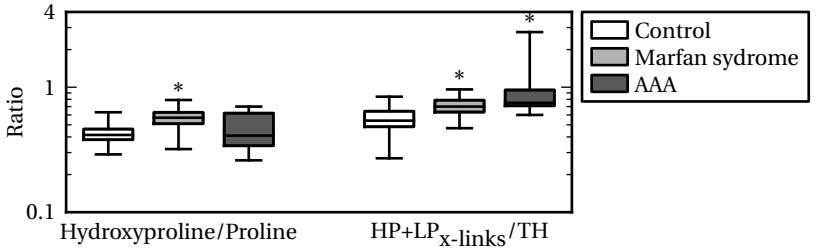

Figure 4.1:
Aortic wall collagen levels were assessed by the hydroxyproline/proline ratio, and the extent of intermolecular collagen cross-links was assessed by the number of hydroxylysyl pyridinoline and lysyl pyridinoline cross-links per triple helix. $*$ $p < 0.00001$.

controversial.[3–5] With the exception of rare mutations in the collagen III gene such as the vascular type of Ehlers-Danlos syndrome, no clear association between impaired collagen homeostasis and aneurysm growth and/or rupture has been identified.

In search of the collagen defect(s) underlying aneurysm formation, we applied an integrated approach of biochemical analyses, multiple imaging modalities, and functional analysis by atomic force microscopy (AFM) to identify the putative collagen defect in aortic abdominal aneurysm (AAA) and in Marfan syndrome, by far the two most common forms of aortic aneurysms. Results of this evaluation show that advanced stages of aneurysmal disease are characterized by distinct defects in the adventitial collagen skeleton armoring the vessel wall rather than by purely biochemical defects.

4.3 Results

Vascular load-bearing collagen is composed of highly stable type I and III fibrillar collagens that are stabilized further by intra-molecular cross-linking.[6] Biochemical as well as morphometric evaluation showed similar collagen concentrations in aneurysm wall from patients with Marfan syndrome and normal, non-aneurysmal control aorta, whereas elevated collagen concentrations were found in AAA (fig. 4.1). The ratio of type I/III collagen MRNA expression was similar in control aorta, Marfan syndrome, and AAA (fig. 4.7). Expression of lysyl oxidase was higher in the aneurysm wall from patients with Marfan syndrome ($p < 0.05$; fig. 4.7). Evaluation of intermolecular collagen cross-linking through quantification of nonreducible lysyl oxidase-initiated collagen cross-links (hydroxylysyl pyridinoline/lysyl pyridinoline cross-links)[7] showed increased intermolecular collagen cross-linking in the aneurysmal wall in both AAA and Marfan tissue (fig. 4.1). These biochemical findings for AAA are in line with reports in the avail-

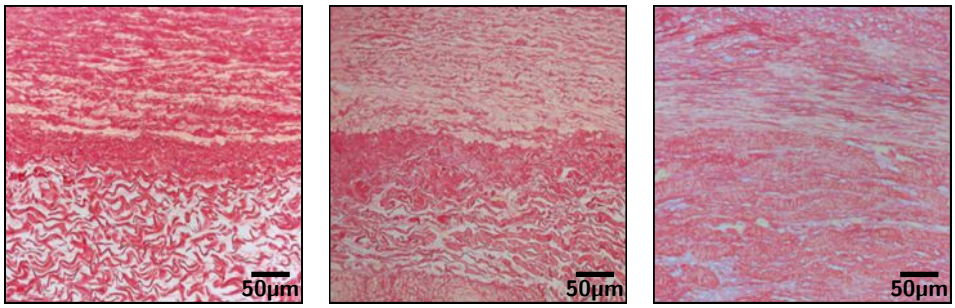

Control Marfan AAA

Figure 4.2:
Collagen deposition (Sirius Red staining) in normal aortic wall and aneurysmal wall in Marfan syndrome and AAA. The images are oriented with the media layer in the upper half and the adventitial layer in the lower half of the image.

able literature, and none of the findings indicates a quantitative or qualitative defect in vascular collagen at the molecular level in AAA or in aneurysms of patients with Marfan syndrome.

In the absence of a clear defect at the biochemical level, we sought for possible structural defects in collagen organization. Histological evaluation (Picro sirius Red collagen staining) (fig. 4.2) and immunohistological staining for collagen type I and III (fig. 4.8) show distinct differences in collagen organization in the medial and adventitial layers of the (grossly) normal aortic wall. A similar pattern but with minor fibrotic changes is seen in the aneurysm wall of patients with Marfan syndrome (fig. 4.2 and fig. 4.8). Collagen deposition in AAA, on the other hand, is hallmarked by complete loss of vessel-wall architecture and deposition of disorganized and condensed collagen (fig. 4.2 and fig. 4.8), a finding that is consistent with fibrosis.

Because the regular 2D images may mask structural defects in the third dimension,[8] we also created 3D reconstructions of the medial and adventitial collagen microarchitecture using the z-stack function on the confocal microscope. These reconstructions show a clearly distinct collagen organization in the medial and adventitial layers of the normal aortic wall (fig. 4.3). Collagen deposition in the medial layer is best characterized by small, interdispersed collagen fibrils that run mainly perpendicular to the circumferential elastic sheets (fig. 4.3A). Adventitial collagen, on the other hand, is arranged in a loose knitting of highly organized ribbon-like collagen bands that brace the medial and intimal layers of the vessel wall (fig. 4.3B). These different architectures appear optimal for achieving the different functionalities for the aortic medial and adventitial layers (elastic recoil and resilience, respectively).[9, 10]

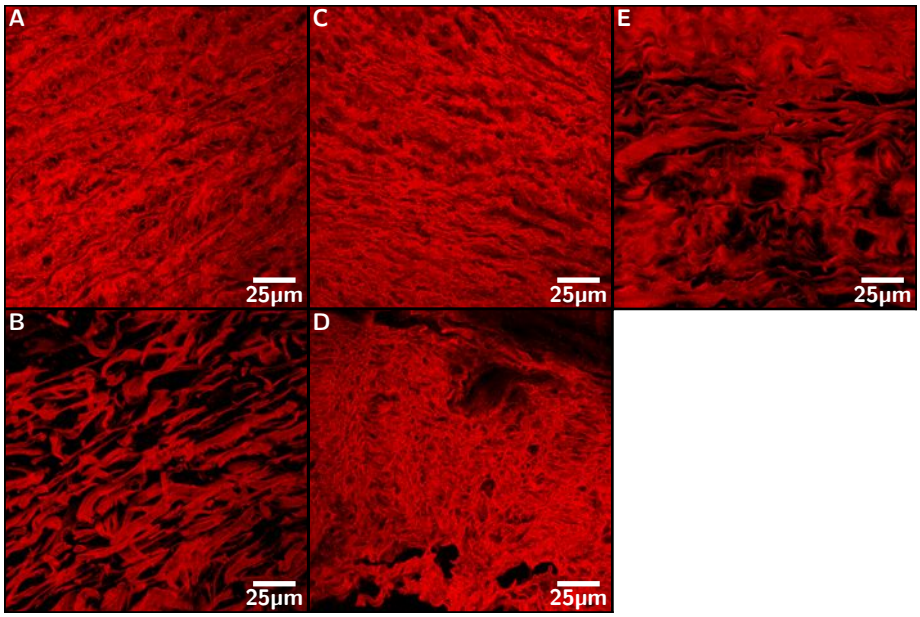

Figure 4.3:
(A,B) Three-dimensional reconstructions (maximum intensity projections of multiple optical sections) of collagen networks in the normal media (A) and adventitial (B) layer.
(C,D) Aneurysms in patients with Marfan syndrome, media (C) and adventitial (D) layer.
(E) Aortic abdominal aneurysm.

Evaluation of collagen architecture in aneurysms of patients with Marfan syndrome showed minor changes in the medial layers of the aortic wall (fig. 4.3C) but a dramatically disturbed collagen architecture in the adventitial layer, with complete absence of the normal collagen fibril organization and deposition of thin parallel collagen fibrils (fig. 4.3D).

Reconstructions for the AAA (fig. 4.3E) show complete loss of the normal architecture, loss of the distinction between medial and adventitial collagen organization, and deposition of aggregated, parallel collagen sheets that appear rigid.

The disordered properties of the collagen microarchitecture in AAA and in the adventitial layer of aneurysms from patients with Marfan syndrome suggest that defects in adventitial collagen organization underlie the weakening of the aortic wall. To test this hypothesis, we performed functional analysis by AFM on normal and aneurysmal adventitial aortic sections. AFM is an established means to test the mechanical properties of individual proteins, cells, and tissue.[11, 12] AFM experiments are performed by indenting the tissue at multiple points with a needle and testing the mechanical response.[13] The tissue response to the

indentation then is used to calculate the elasticity (Young's modulus) for the given point. (The method is described in SI Materials and Methods, section 4.5.) Multiple individual elasticity measurements then are integrated to create a visual representation (stiffness map) of the probed area. The high force resolution of the AFM (in pico-newtons) and its high lateral resolution (i.e., several elasticity measurements per square micrometer) make the AFM ideal for precisely mapping the mechanical properties of tissue at the microscale level, thereby allowing comparison of the elasticity map with the confocal images (fig. 4.3). Moreover, the individual elasticity measurements can be compiled into a histogram that can be used to express the distribution of the elasticity of the arterial wall at a larger scale.

Tissue was probed at two different levels by using different AFM cantilevers: a sharp tip (20 nm end radius) and a blunter ball tip (10 µm radius). These two tips allow a comparison of the different scales in the tissue. The size of the sharp tip is chosen to interact only with individual molecules in the tissue (individual fiber level), whereas the larger ball tip is designed to probe at the tissue level (fibril behavior). The elasticity modulus (Young's modulus) was calculated for each indentation, because then the size and shape of the indenter can be removed, allowing direct comparison of the two measurements. The combined measurements provide a complete picture of the mechanical properties of the tissue and allow the AFM measurements to be compared with previous conventional studies of the mechanical properties of AAA and normal aorta segments.[14, 15] Note, however, that all measurements are performed on a microscale level, not fully loading the fibers.

Stiffness histograms combining the individual data points (fig. 4.4) show that the tissue response of the control adventitia is independent of the size of the tip that is used. This finding indicates that the normal adventitial tissue behaves as a highly coherent network. The stresses encountered by the tissue are dispersed equally over the whole network, and the scale of the challenger does not matter. The fact that the sharp indenter is not able to penetrate the network to a greater extent than the ball tip shows that the individual collagen fibers are densely interconnected, because the fibers do not slide out of the way and are all pulled when a single fiber is moved.

The major difference between the aneurysmal tissues and normal tissue is immediately apparent from the histogram in fig. 4.4 and the AFM force-volume topography (fig. 4.5). Unlike normal tissue, the stiffness of AAA tissue is clearly dependent on the size of the AFM tip: The ball tip, which interacts with the larger structures, senses a very stiff tissue. This observation is in line with our confocal images and conventional biomechanical studies that show that AAA tissue has become stiffer.[16] The sharp tip, on the other hand, meets hardly any resistance,

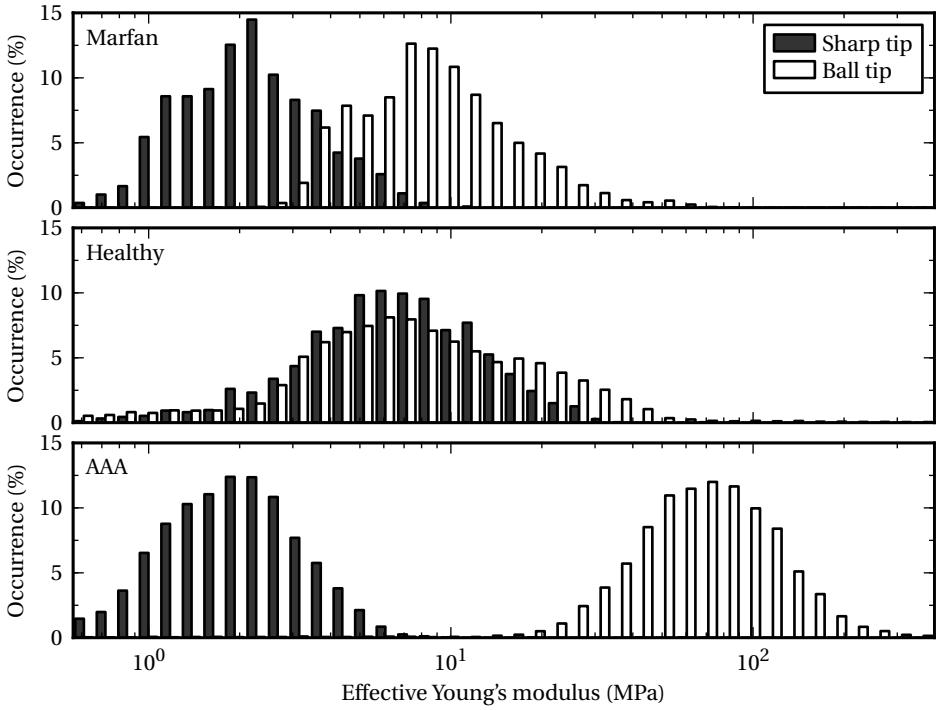

Figure 4.4:
Histograms showing the distribution of the effective Young's modulus for the different conditions. White bars show curves taken with the sharp tip; black bars show curves taken with the ball tip. Values are plotted on a log scale to improve the comparison of the modulus.

suggesting that the sharp tip pushes the fibers of the extracellular matrix aside. This observation indicates that the interconnections that normally allow the tissue to behave as a coherent network are missing in AAA.

Probing of Marfan aneurysmal tissue shows a tissue behavior that is clearly distinct from both control aorta and AAA tissue. The larger ball tip senses stiffness similar to that of normal tissue, suggesting that under the conditions of the AFM experiment (a resting, nonstretched state) the tissue elasticity at a larger scale equals that of normal aortic wall. The sharp tip, on the other hand, finds little resistance and plunges through the tissue just as it did with AAA tissue. This observation indicates that the individual fibers are pushed aside when probed with the 25 nm tip and thus that the loaded fibrils are unable to transfer the stress and strain to the neighboring fibrils (i.e., absence of network behavior).

Another remarkable finding distinct to the Marfan tissue is that sections of the tissue collapse as the force is applied (fig. 4.10). These sections appear to be small voids in the collagen network that also are observed in the confocal images (fig. 4.3D). Such voids could provide sites susceptible to dissection or rupture.[17]

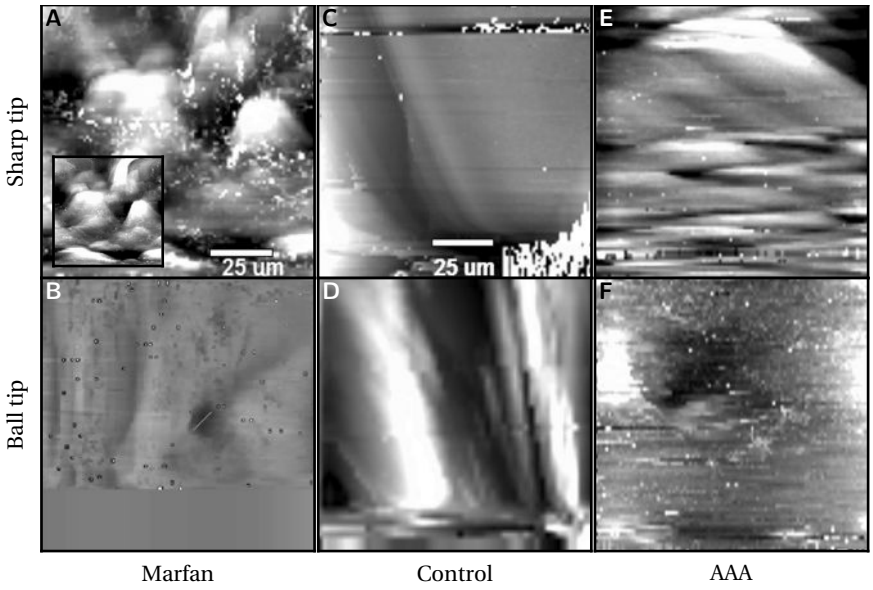

Figure 4.5:
Topography maps for the various tissues as determined from AFM force-volume spectroscopy at 11 nN of constant force. The inset in (A) shows the Marfan tissue at 40 nN; it is apparent that the force collapses something in the tissue at various points resulting in a much smoother-looking surface.

4.4 Discussion

This study shows that advanced aneurysms in AAA and Marfan syndrome are associated more with distinct defects in the collagen microarchitecture than with a collagen defect at the biochemical level. These architectural defects result in loss of the normal stress-strain curve and in impaired collagen network behavior, both of which can contribute to the aortic wall failure.

Visualization of adventitial collagen structures in the control aorta shows a collagen architecture that is best described as a loosely knitted network of interwoven collagen ribbons encasing the medial layer. A similar architecture has been described previously for the adventitial layer of the urine bladder, and it was shown that the collagen ribbons align during bladder filling, thereby allowing the bladder to distend easily but preventing overstretching.[18] The aortic adventitial layer may serve a similar purpose: its flexibility allows the arterial wall to dilate easily but resists overstretching once fully loaded. Such a construction is similar to the textile and metal plies in a steel-belted radial tire that allow flexibility but prevent failure in extreme conditions.

The different architectures of the medial and adventitial layers may well explain

the J-shaped stress-strain curve (i.e., the nonlinearity of the curve) of the normal vessel wall and suggest that the two layers have different functionalities, the elastic medial layer being responsible for the flat, horizontal part of the curve and the adventitial knitting resulting in the steep arm of stress-strain curve.[19]

Visualization of the collagen braiding in Marfan aneurysms and AAA in vessel-wall samples that were obtained at the time of operation (i.e., from advanced stages of the disease) shows that the collagen fibrils run almost in parallel, thereby limiting their ability to stretch, and therefore stiffen the vessel. This observation is well in line with biomechanical studies that show that both AAA and Marfan aneurysms are stiffer than the normal vessel wall.[16, 20]

The increased stiffness of AAA tissue also is immediately apparent from the AFM experiments performed with a ball tip that show a sharp increase in the effective Young's modulus for AAA tissue, indicating that the tissue resisted even the minimal indentations (2–3 µm) by the AFM tip. The similar Young's moduli for ball-tip experiments in normal aorta and aortas from patients with Marfan syndrome seemingly conflict with biomechanical studies that indicate that Marfan tissue is stiffer than normal tissue.[20] This apparent contradiction presumably reflects a limitation when AFM measurements are performed under resting, nonstretched conditions. The confocal images clearly show that under such conditions collagen fibrils in Marfan tissue adopt a wave-like pattern that allows them to stretch when probed with the AFM tip.

Findings from this study also point to defects in collagen network behavior in the aneurysmal tissues studied. Network behavior has long been recognized as a key to mechanical stability in the field of structural design, but, remarkably, in the biomedical context network behavior has only been reported for bone tissue.[12] Our results indicate that aneurysms in both AAA and Marfan tissue are associated with defects at all three scale lengths (i.e., at the intrafibril, intrafiber, and suprafiber levels). Impaired network behavior may interfere with the dissipation of the mechanical forces over the arterial wall, thereby contributing further to the mechanical failure of the aortic wall.

In conclusion, the findings in this study provide a structural explanation of how biological tissue (i.e., normal arterial wall) can acquire its typical nonlinear stress-strain curve and also can settle the longstanding controversy regarding the existence of a collagen deficiency in AAA. We show that defects in collagen architecture and network behavior, rather than a defect at the molecular level, explain the debilitation of the aortic wall in AAA and aneurysms in Marfan syndrome. The observed changes in AAA do not necessarily reflect the primary cause of AAA formation. More likely, the changes in AAA reflect inappropriate collagen deposition (fibrosis) in an environment that is characterized by sustained inflammation and activation of multiple proteolytic pathways. The findings in Marfan syndrome, on

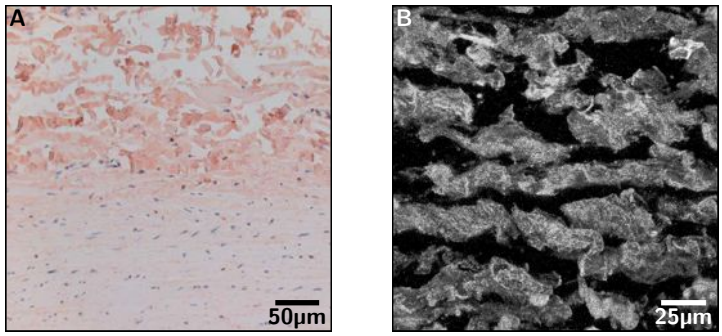

Figure 4.6:
Fibrillin localization in the normal aortic wall (immunohistochemistry).
(A) Fibrillin (reddish-brown) is present primarily in the adventitial layer of the aortic wall.
(B) Three-dimensional reconstruction by confocal microscopy showing that fibrillin colocalizes with adventitial collagen.

the other hand, may reflect a primary defect: Unlike AAA, aneurysms in patients with Marfan syndrome do show signs of increased inflammation and proteolytic activities.[21] As such, the observed defects in the collagen microarchitecture may reflect a primary defect that could relate to impaired TGF-β signaling. However, the strong link between a defect in the fibrillin gene and development of Marfan syndrome also may reflect a role of fibrillin in the organization of the collagen bands in the adventitial layer. This notion is supported by the fact that fibrillin is localized predominantly in the adventitia of the normal aortic wall (fig. 4.6A) and by the pattern of fibrillin deposition that is similar to that of the adventitial collagen network (fig. 4.6B). Our findings confirm the longstanding assumption that Marfan syndrome is a collagen disorder[22] and show that Marfan syndrome is associated with a defect in collagen network organization. Such a defect may well explain most of the other phenotypical features of Marfan syndrome which appear related to collagen dysfunction (e.g., skeletal deformities, hernias, dural ectasia, and ectopia lentis).

We speculate that defects similar to those in AAA explain the longstanding apparent contradiction between increased collagen content but reduced mechanical strength during wound healing and scar formation.[23] Microarchitectural defects in collagen network formation may well contribute to scar formation in postfetal wound healing that currently is attributed to a reduced elastin transcription after birth.[24]

4.5 Materials and Methods

All human arterial wall samples were provided by the Vascular Tissue Bank, Department of Vascular Surgery, Leiden, The Netherlands. Sample collection and handling was performed in accordance with the guidelines of Medical Ethical Committee of the Leiden University Medical Center, Leiden, The Netherlands, and the code of conduct of the Dutch federation of Biomedical Scientific Societies.[25]

Anterior lateral aneurysm wall samples were obtained from patients with an AAA > 55 mm undergoing elective open repair (AAA group: $n = 17$, mean age 72.4 ± 6.2 years). Thoracic aortic aneurysms (ascending aorta, diameter > 50 mm) of Marfan patients were obtained during elective repair (Bentall procedures) (Marfan group: $n = 11$, age 26.9 ± 8.2 years). All Marfan patients met the international criteria for Marfan syndrome.[26]

Control (normal) abdominal aortic wall was obtained during kidney explantation for organ donation. All these control samples were obtained from the level of the renal artery, i.e., from a location comparable to that of the samples from AAA patients ($n = 11$, age 55.6 ± 10.2 years). The primary cause of the fatal brain injury in this control group was a major head trauma or subarachnoidal bleeding.

Control thoracic aorta (post mortems) from patients dying from noncardiac causes was used as a histological reference for the Marfan tissue.

Following excision, half of the sample was fixed in formalin for 24 h, decalcified in Kristensen's solution, and subsequently embedded in paraffin for immunohistochemical analysis. The remaining half was immediately flash-frozen in liquid nitrogen for mRNA analysis and for the preparation of cryosections.

Details on the biochemical, histological, and AFM methodology and reproducibility (fig. 4.9), and statistical analysis are provided in SI Materials and Methods.

4.6 Supporting Information

SI Materials and Methods

Collagen and Cross-Link Analysis. Ten 10 μm slices of paraffin-embedded tissue were deparafinized in xylene, and the samples were hydrolyzed (110 °C, 20–24 h) in 1 mL 6 M HCl in 5 mL Teflon-sealed glass tubes. The samples were dried and redissolved in 1 mL of water containing 10 μM of pyridoxine [internal standard for the cross-links hydroxylysylpyridinoline (HP) and lysyl-pyridinoline] and 2.4 mmol/L of homoarginine (internal standard for amino acids) (Sigma). Samples were diluted 5-fold with 0.5% (vol/vol) heptafluorobutyric acid (Fluka) in

10% (vol/vol) acetonitrile for cross-link analysis; aliquots of the 5-fold diluted sample were diluted 50-fold with 0.1 M sodium borate buffer (pH 8.0) for amino acid analysis. Derivatization of the amino acids with 9-fluorenylmethyl chloroformate and reversed-phase HPLC of amino acids and cross-links was performed on a Micropak ODS-80TM column (150 mm × 4.6 mm) (Varian) as described previously.[27, 28] The quantities of the cross-link HP were expressed as the number of residues per collagen molecule, assuming 300 hydroxyproline (Hyp) residues per triple helix. This procedure is well established, because Hyp is a collagen-specific amino acid and because the prolyl hydroxylation level in collagen is stable.

RNA Extraction and mRNA Analysis. Total RNA extraction was performed using RNAzol (Campro Scientifics) and glass beads according to the manufacturer's instructions. Copy-DNA was prepared using kit #A3500 (Promega), and quantitative realtime PCR analysis was performed for collagen type I and III and lysyl oxidase on the ABI-7700 system (Applied Biosystems) using established primer/probe sets (Assays on Demand; Applied Biosystems) and MasterMix (Eurogentec). Analyses were performed according to the manufacturers' instructions and as previously reported.[29] GAPDH expression was used as a reference and for normalization.

Histology. Histochemistry and immunohistochemistry was performed on 4 µm deparaffinized, ethanol-dehydrated tissue sections. Collagen staining was performed by the Sirius Red-picrine method.[30] Immunohistochemical staining for collagen type I and III and fibrillin was performed using specific antibodies for collagen type I (C7510-17K; US Biological), collagen type III (C7510-39G; US Biological), or fibrillin (MAB1919, Chemicon). Pepsin-trypsin retrieval was required for optimal collagen I and III staining, and a 10 mM (pH 6.0) citrate retrieval was required for the fibrillin staining.

AB-conjugated biotinylated anti-goat or rabbit anti-IgG was used as secondary antibody. Sections were stained with Nova Red (Vector Laboratories) and counterstained with Mayer's hematoxylin. Controls were performed by omitting the primary antibody.

We used confocal microscopy (LSM615; Zeiss) for the visualization of the collagen network structures. Tissue slices (20 µm) were stained with Sirius Red, and Sirius Red fluorescence was used for the reconstruction. Fibrillin deposition was evaluated by immunohistochemical staining (see above) using the Alexa 647 mouse anti-goat antibody for visualization. Serial confocal sections of x-y images (stack size 206 µm × 206 µm) of representative sections of the medial and adventitial layer were made along the z axis with a distance of 0.5 µm. The excitation

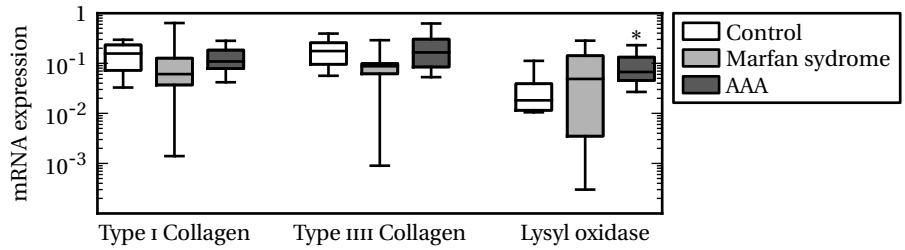

Figure 4.7:
mRNA expression relative to GAPDH (GAPDH = 1) of type I and III collagen, and lysyl oxidase (a key enzyme required for collagen cross-linking). $*$ $p < 0.00001$.

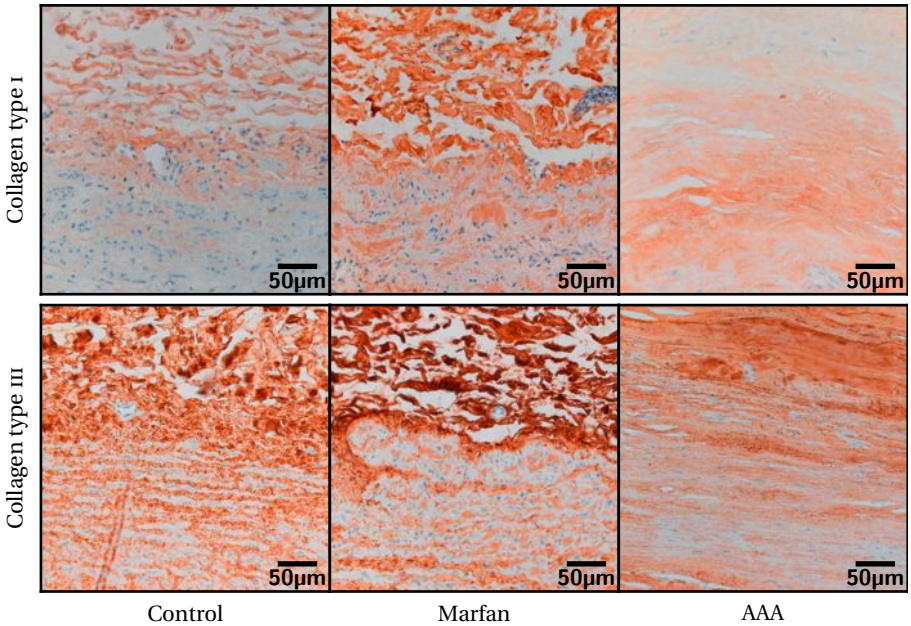

Figure 4.8:
Collagen type I and III distribution in medial-adventitial border zone of control (abdominal) aorta, ascending aortic aneurysm in Marfan syndrome, and AAA.

and emission wavelengths were 543 and 633 nm, respectively, for the Sirius Red staining and were 633 and 647 nm, respectively, for immunohistochemical (Alexa 647) staining. The pinhole was set at 108 µm. Three-dimensional reconstructions of confocal stacks (20 serial images at 0.5 µm intervals) were performed using the stacks-z-function on the Zeiss LSM Image Examiner version 3.2.0.115.

Atomic Force Microscopy. Atomic force microscopy (AFM) measurements were performed on 8 µm-thick tissue slices. To that end, tissue was cryosliced to 8 µm thickness, perpendicular to the flow of the blood, and stored at −80 °C. Measurements were done using a Molecular Imaging PicoScan atomic force microscope controlled with a custom scripting program written in LabVIEW (National Instruments) and Visual Basic 6 (Microsoft). Data were recorded with a National Instruments card at 100 kS/s and then processed into higher-resolution force-volume images than can be taken with the control software of the AFM. All force-distance curves were performed at a rate of 1 Hz.

Tissue was probed at two different resolutions: A sharp tip (20 nm tip radius) was used to probe the tissue on the fibril level, and a 10 µm ball tip was used to probe at the tissue level.[31, 32] The sharp tips were Nanoprobe tips model NP (Veeco). Cantilevers were calibrated using the thermal method.[33]

Balls tips were specially modified tips from Novascan. These tips are Park cantilevers (Veeco) to which a 10 µm glass ball is attached. Because the effective stiffness of the tissue is greater when probed at a larger scale, we choose cantilevers with a force constant of 0.32 N/m. Tips were coated by a layer of polyethylene glycol (molecular weight 3,400 kDa) to prevent fouling.

All AFM measurements were performed in a liquid cell (Molecular Imaging) in PBS. Preliminary evaluation showed that the AFM measurements on the aorta sections were independent of the spring constant of the cantilevers. Consistency of the data was checked by measuring the variations in stiffness in a number of healthy individuals. As shown in fig. 4.9, the variation among the individuals tested is consistent with the conclusion that the differences found among different tissues are disease specific rather than representing variation among individuals.

AFM Function and Nanoindentation. Force-extension curves were performed by laying a section of tissue on a glass slide and immersing it in the PBS buffer in the liquid cell. Tissue then was loaded in the AFM microscope, and a force-volume dataset was produced by pushing the cantilever into the tissue at each point on a grid. This technique allowed the collection of a 2D grid of indentation data that then was transformed as explained below into effective Young's modulus as well

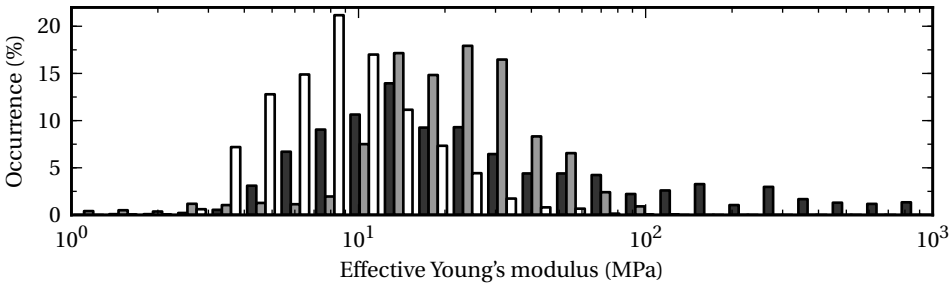

Figure 4.9:
Force distribution of three distinct healthy aortas (black, gray and white bars) measured by the sharp tip.

as a constant-force topograph.

The Young's modulus was determined using the methods of A-Hassan et al.[34] This technique is more robust to the errors that are inherently present in fitting the Hertz model[35] of an indenter to data collected from AFM force-distance curves. A detailed discussion of the methods that can be used to find the Young's modulus from AFM force-extension curves can be found in Stolz et al.[36] or in A-Hassan et al.[34] This technique involves determining the work performed by the cantilever on the tissue sample and then comparing this work with a known standard. By integrating the total area under the force-distance curve, local variations are minimized, and the curve fitting becomes less difficult. Most importantly, the exact point of contact between surface and AFM cantilever is no longer needed, because the area under the curve at the estimated contact point is small compared with the total area under the curve. Its ease of application and, more importantly, its reproducibility, make this technique the more desirable method of determining the effective Young's modulus of the tissue.

In this case, Sneddon's equations[37] were used to estimate the curve that would be expected with a conical (sharp tip) or spherical (ball tip) Hertz model indenter. Although this estimation negates some of the advantages of this method, namely the ability to divide the shape, force constant, and sensitivity of the tip from the equation, it still produces a standard curve to which all of the curves analyzed by this method have been compared. Thus, although the absolute value for the Young's modulus has a large error, the error is systematic, and comparisons between the various datasets are still completely valid.

Validity and Reproducibility of the AFM Measurements. Two different force constants were used between the ball tips and the sharp tips. To determine what effects the differing force constants would have, we performed an experiment

with the sharp tip on aortic abdominal aneurysm (AAA) tissue. Various cantilevers were available on the nanoprobe chip; we used cantilevers with the 0.06 N/m and the 0.32 N/m tips, force constants that were chosen specifically to match the stiffness of the tissue and therefore to maximize the force resolution.

The effect from the force constant of the cantilever over this range is negligible. The observed differences pale in comparison with the differences between the Marfan and AAA tissue. Therefore we can safely assume that the differences seen in the aneurysmal tissue between the ball tip and the sharp tip result solely from the differences in tip shape.

Action of Ball Tip vs. Sharp Tip. The different-sized tips allow very different information about the collagen networks to be collected, and the data provide a sense of the coherence of the matrix network. The two tips allow an understanding of the collagen networks as well as interacting directly with individual proteins. The sharper tip is smaller than the radius of a collagen fibril. It is able to interact directly with these structures in the extracellular matrix as well as slip between the fibers. The ball tip was chosen to interact with the tissue on a micrometer scale. This tip is able to push tens of fibers and directly measures the network indentation properties of the tissue. The size is a compromise between seeing the large network behavior and yet remaining small enough to handle with an AFM tip.

Nanoindentation Stiffness Maps. The force-vs.-distance curves were processed into a combination topography and stiffness image by combining all the force-extension curves from the AFM measurements into a grid and then taking the extension at which the force reached a certain level as the intensity at that point. This method is sensitive to both the initial height of the tissue and to the stiffness of the tissue under the cantilever. Regions where the tissue is stiffer will indent less before the required force is reached and will therefore appear higher than regions that were equally high before indentation but that are softer. We find that these images provide information complementary to the collagen confocal images.

Statistics. Differences between the groups were evaluated by an unpaired t test (for the normally distributed data) or by the Wilcoxon-Mann-Whitney test (for non-normally distributed continuous data). The level of significance was set at $p < 0.05$. All analyses were performed using SPSS16.0 (SPSS Inc.)

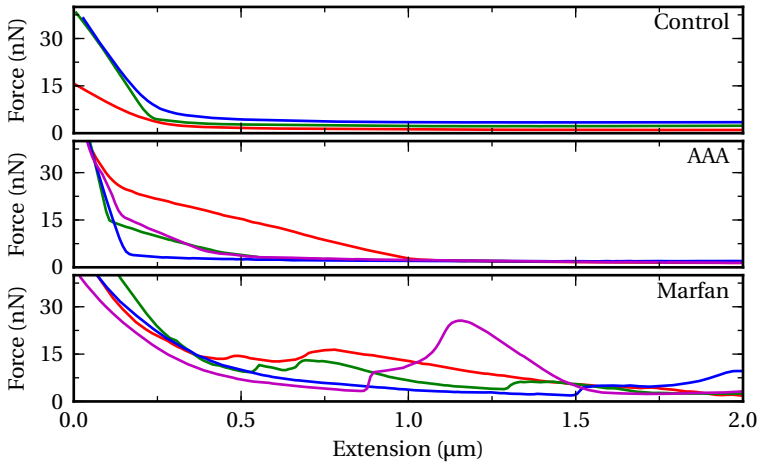

Figure 4.10:
Individual force extension curves. "Extension" refers to the length of the piezoelectric tube. Motion toward zero results in indentation of the tissue by the cantilever tip. (Top) Curves sampled from control tissue. (Middle) Curves sampled from AAA tissue showing the nonlinear interactions common on the AAA tissue with the ball tip. It is proposed that the nonlinearity is a result of one collagen fiber being pushed into a second fiber, resulting in markedly stronger forces with nonlinear transitions at the connection. This behavior is consistent with the notion that there are fewer interconnections between the various collagen fibers resulting in no warning for the second fiber and its sudden recruitment. (Bottom) Curves sampled from Marfan tissue showing the collapses that are common with the Marfan tissue. These collapses could be the result of the weakened collagen fibers slipping to the side of the tip or could indicate structural weaknesses in the tissue. The confocal images in fig. 4.3A and B show the presence of small voids.

4.7 References

[1] N. Sakalihasan, R. Limet, and O. Defawe. Abdominal aortic aneurysm. *Lancet*, 365:1577, 2005.

[2] R. W. Thompson, P. J. Geraghty, and J. Lee. Abdominal aortic aneurysms: Basic mechanisms and clinical implications. *Curr. Prob. Surg.*, 39:98, 2002.

[3] G. McGee, et al. Aneurysm or occlusive disease - factors determining the clinical course of atherosclerosis of the infrarenal aorta. *Surgery*, 110:370, 1991.

[4] R. J. Rizzo, et al. Collagen types and matrix protein content in human abdominal aortic aneurysms. *J. Vasc. Surg.*, 10:365, 1989.

[5] S. Menashi, J. S. Campa, R. M. Greenhalgh, and J. T. Powell. Collagen in abdominal aortic aneurysm: typing, content, and degradation. *J. Vasc. Surg.*, 6:578, 1987.

[6] S. M. Sweeney, et al. Candidate cell and matrix interaction domains on the collagen fibril, the predominant protein of vertebrates. *J. Biol. Chem.*, 283:21187, 2008.

[7] H. M. Kagan and W. Li. Lysyl oxidase: properties, specificity, and biological roles inside and outside of the cell. *J. Cell. Biochem.*, 88:660, 2003.

[8] J. Alkemper and P. W. Voorhees. Quantitative serial sectioning analysis. *J. Microsc*, 201:388, 2001.

[9] P. B. Dobrin, W. H. Baker, and W. C. Gley. Elastolytic and collagenolytic studies of arteries. Implications for the mechanical properties of aneurysms. *Arch. surg.*, 119:405, 1984.

[10] T. Inahara. Eversion endarterectomy for aortoiliofemoral occlusive disease. A 16 year experience. *Am. J. Surg.*, 138:196, 1979.

[11] T. Ludwig, R. Kirmse, K. Poole, and U. S. Schwarz. Probing cellular microenvironments and tissue remodeling by atomic force microscopy. *Pflugers Arch.*, 456:29, 2008.

[12] G. E. Fantner, et al. Sacrificial bonds and hidden length dissipate energy as mineralized fibrils separate during bone fracture. *Nat. Mater.*, 4:612, 2005.

[13] N. Gadegaard. Atomic force microscopy in biology: technology and techniques. *Biotech. Histochem.*, 81:87, 2006.

[14] J. F. Rodríguez, C. Ruiz, M. Doblaré, and G. A. Holzapfel. Mechanical stresses in abdominal aortic aneurysms: influence of diameter, asymmetry, and material anisotropy. *J. Biomech. Eng.*, 130:021023, 2008.

[15] D. A. Vorp and J. P. Vande Geest. Biomechanical determinants of abdominal aortic aneurysm rupture. *Arterioscler. Thromb. Vasc. Biol.*, 25:1558, 2005.

[16] C. M. He and M. R. Roach. The composition and mechanical properties of abdominal aortic aneurysms. *J. Vasc. Surg.*, 20:6, 1994.

[17] N. M. Ammash, T. M. Sundt, and H. M. Connolly. Marfan syndrome-diagnosis and management. *Curr. Probl. Cardiol.*, 33:7, 2008.

[18] S. L. Chang, P. S. Howard, H. P. Koo, and E. J. Macarak. Role of type III collagen in bladder filling. *Neurourol. Urodyn.*, 17:135, 1998.

[19] R. E. Shadwick. Mechanical design in arteries. *J. Exp. Biol.*, 202:3305, 1999.

[20] B. Sonesson, F. Hansen, and T. Länne. Abnormal mechanical properties of the aorta in Marfan's syndrome. *Eur. J. Vasc. Surg.*, 8:595, 1994.

[21] M. J. Collins, et al. Variation in the histopathological features of patients with ascending aortic aneurysms: a study of 111 surgically excised cases. *J. Clin. Pathol.*, 61:519, 2008.

[22] M. Macek, J. Hurych, M. Chvapil, and V. Kadlecová. Study of fibroblasts in Marfan's syndrome. *Humangenetik*, 3:87, 1966.

[23] J. Madden. *Textbook Of Surgery; The Biological Basis Of Modern Surgical Practice.* Wound healing (W. B. Saunders, Philadelphia, 1986).

[24] M. T. Longaker and N. S. Adzick. The biology of fetal wound healing: a review. *Plast. Reconstr. Surg.*, 87:788, 1991.

[25] Code of conduct of the Dutch federation of Biomedical Scientific Societies, http://www.federa.org/?s=1&m=78&p=&v=4.

[26] A. De Paepe, et al. Revised diagnostic criteria for the Marfan syndrome. *Am. J. Med. Genet.*, 62:417, 1996.

[27] R. A. Bank, E. J. Jansen, B. Beekman, and J. M. te Koppele. Amino acid analysis by reverse-phase high-performance liquid chromatography: improved derivatization and detection conditions with 9-fluorenylmethyl chloroformate. *Anal. Biochem.*, 240:167, 1996.

[28] R. A. Bank, et al. Sensitive fluorimetric quantitation of pyridinium and pentosidine crosslinks in biological samples in a single high-performance liquid chromatographic run. *J. Chromatogr. B Biomed. Sci. Appl.*, 703:37, 1997.

[29] H. Abdul-Hussien, et al. Collagen degradation in the abdominal aneurysm: a conspiracy of matrix metalloproteinase and cysteine collagenases. *Am. J. Pathol.*, 170:809, 2007.

[30] L. C. Junqueira, G. Bignolas, and R. R. Brentani. Picrosirius staining plus polarization microscopy, a specific method for collagen detection in tissue sections. *Histochem. J.*, 11:447, 1979.

[31] P. D. Kemp and J. E. Scott. Ehrlich chromogens, probable cross-links in elastin and collagen. *Biochem. J.*, 252:387, 1988.

[32] S. R. Pinnell and G. R. Martin. The cross-linking of collagen and elastin: enzymatic conversion of lysine in peptide linkage to alpha-aminoadipic-delta-semialdehyde (allysine) by an extract from bone. *PNAS*, 61:708, 1968.

[33] J. L. Hutter and J. Bechhoefer. Calibration of atomic-force microscope tips. *Rev. Sci. Instrum.*, 64:1868, 1993.

[34] E. A-Hassan, et al. Relative microelastic mapping of living cells by atomic force microscopy. *Biophys. J.*, 74:1564, 1998.

[35] H. Hertz. Ueber die Berührung fester elastischer Körper. *Journal für die reine und angewandte Mathematik (Crelles Journal)*, 1882:156, 1882.

[36] M. Stolz, et al. Dynamic elastic modulus of porcine articular cartilage determined at two different levels of tissue organization by indentation-type atomic force microscopy. *Biophys. J.*, 86:3269, 2004.

[37] I. N. Sneddon. The relation between load and penetration in the axisymmetric Boussinesq problem for a punch of arbitrary profile. *Int. J. Eng. Sci.*, 1965.

5 Mechanical properties of the aorta studied by enzymatic treatments

This chapter is currently in press as:
Mechanical properties of the extra cellular matrix of the aorta studied by enzymatic treatments
J. W. M. Beenakker, B. A. Ashcroft, J. H. N. Lindeman and T. H. Oosterkamp
Biophysics Journal, 2012

5.1 Abstract

The micro-architecture of different components of the extra cellular matrix is crucial to the understanding of the properties of a tissue. In the study presented here, we use a top-down approach to understand how the interplay between different fibers determines the mechanical properties of real tissues. By selectively removing different elements of the arterial wall, we are able to measure the contribution of the different constituents of the extra cellular matrix (ECM) to mechanical properties of the whole tissue. The change in the network structure is being imaged using two-photon microscopy. The Atomic Force Microscope is used to measure the change in mechanical properties by performing nano-indentation experiments.

We show that although the removal of a key element of the ECM reduced the local stiffness by up to 50 times, the remaining tissue still formed a coherent network. We also show how this method can be extended to study the effects of cells on real tissues. This new way of studying the ECM will not only help physicists gain a better understanding of biopolymers, it will be a valuable tool for biomedical researchers studying processes such as wound healing and cervix ripening.

5.2 Introduction

In addition to the different fibers and other components making up a tissue, the micro-architecture of the different components is crucial to the mechanical properties of a tissue. In recent years, different in vitro studies on reconstituted components of the extra cellular matrix (ECM) have shed a light on the physical principles that determine the mechanical properties of tissues. In such a bottom-up approach, one or two different ECM-components are combined to make a gel and reveal a rich interplay between fibers, linkers and cells.[1–4]

In the study presented here, we use a top-down approach to understand how the interplay between different components determines the mechanical properties of real tissues. By selectively removing different elements of the arterial wall, e.g. removing the collagen by collagenase, we were able to measure the contribution of the different constituents of the ECM to the mechanical properties of the tissue as a whole. Similar proteolytic treatments on the arterial wall have previously been used to study the spatial organisation of the fibers within the tissue using immunofluorescence[5] and scanning electron microscopy.[6] Despite the difficulties posed by the complexity of real tissues, this method allows the microarchitecture present in real tissues to be studied. Ultimately, this method

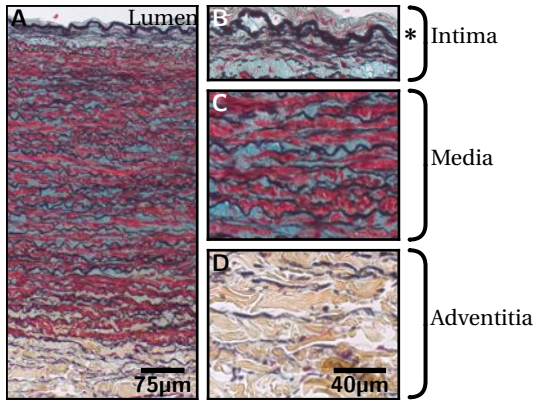

Figure 5.1:
Microscopic overview of the anatomy of the abdominal aortic wall using Movat pentachrome staining.
The aortic wall (A) is composed of multiple layers consisting of different builds. The intima (B) is the thin inner layer of the vessel wall, containing endothelial cells which are in contact with the lumen and is separated from the media (C) by the internal elastic lamina (∗). The tunica adventitia (D) contains mainly collagen (brown), while the tunica media also consists of elastin (dark blue/black) and smooth muscle cells (red). Proteoglycans (light blue) are present in both layers, but predominantly in the media.
(A) was taken at 100 × magnification, (B–D) were taken at 400 × magnification.

could be extended to study the effects of cells on the extra cellular matrix, e.g. by studying the effects of the contents of neutrophils on the extra cellular matrix. The change in the network structure is being imaged using two photon microscopy. Previous studies have used enzymatic digestions to differentiate the contributions of the different constituents of the ECM to the mechanical response of the whole tissue.[7–11] In this study, the Atomic Force Microscope (AFM) is used to measure the change in mechanical properties on the sub-micrometer scale by performing nano-indentation experiments.

5.3 Materials and Methods

All experiments have been performed on porcine aorta to minimize the biological variation between samples. Whole porcine aortas were collected within 18 hours after slaughter sliced in 15mm pieces and snap frozen in liquid pentane. The tissue was cryosliced to 50µm and stored at -80°C until used.

The aortic wall is composed of multiple layers consisting of different builds, as is shown in fig. 5.1. By studying the tunica adventitia, the collagen rich outer layer of the aorta, and the neighboring tunica media, which is rich in elastin and

Sample	Concentration	Temperature
Control/PBS	-	25 °C / 37 °C
Elastase (Worthington)	5.5 u/ml	25 °C
Collagenase (Worthington, type CLSPA)	200 u/ml	37 °C
Chodroitionas ABC (Sigma) + Hyalunoidase (Sigma)	1000 u/ml 0.04 u/ml	37 °C
Neutrophils	10 times diluted	37 °C

Table 5.1:
Concentrations of enzymes used for the various proteolytic treatments.
PBS was used as a buffer for al experiments except for the Chondroitinase ABC + Hyaluronidase, in which a 50 mM Tris (Sigma), 10 mM sodium (Sigma) acetate buffer was used for the incubation and all the sample preparation steps. Incubation took place in the presence of penicillin (50 units/ml, Sigma) + streptomycin (50 µg/ml, Sigma) to prevent the growth of bacteria. Elastase and collagenase are from Worthington Biochemical Corporation, Lakewood, NJ.

also contains some collagen fibers, we can examine the proteolytic effects on two different networks within one sample.

After thawing, the samples were put in PBS (137 mM NaCl, 2.7 mM KCl, 8 mM Na2PO4, 1.8 mM KH2PO4, pH 7.4, all from Sigma-Aldrich, Zwijndrecht, The Netherlands) for approximately 5 minutes to reconstitute. After removal of the PBS, the samples where covered with PBS with penicillin-streptomycin (50 units/ml) and the enzymes in a stove overnight at 37 °C, except for the elastin digestion which was performed overnight at 25 °C. The concentrations of the enzymes, listed in table 5.1, are chosen such that the specific components are removed, but the rest of the tissue remains intact.[9] The contents of neutrophils, activated by 100 nM formyl-Met-Leu-Phe (Sigma), were prepared as described in ref. [12]. After the proteolytic treatment, the buffer with enzymes is changed to PBS and the sample is used either for two-photon imaging or AFM nano-indentation.

Second-harmonic generation (SHG) was used to image the organization of the collagen and the elastin fibers.[13] To detect collagen we used filter settings to be sensitive for frequency doubling, while to detect elastin we relied on its autofluorescence. The two-photon microscopy was performed on a Zeiss 710 NLO (Jena, Germany) upright confocal microscope equipped with a Spectra-Physics Deep See MP laser (Spectra-Physics, Inc., Mountain View, CA). The images were obtained with an excitation wavelength of 800 nm and emitted light with a wavelength between 371 nm–425 nm was detected for the collagen signal and between 471 nm–532 nm for elastin. Confocal stacks were processed for maximum intensity projections with the Zeiss ZEN2009 software.

The AFM nano-indentation experiments are performed as described in chapter 3. In short, measurements were done using a Molecular Imaging Picoscan AFM (Agilent Technologies, Palo Alto, CA) controlled with a custom scripting program

written in LabVIEW (National Instruments, Austin, TX) and Visual Basic 6 (Microsoft, Redmond, WA). The nano-indentation was performed with a 0.58 N/m cantilever (NP type (Veeco Metrology, Santa Barbara, CA)) with a sharp tip and was recorded with a National Instruments card at 100 kS/s. MATLAB (The MathWorks, Natick, MA) was used to calculate the Young's modulus for each indentation using the FIEL method of Hassan et al.[14] This method calculates the work needed for a certain deformation by integrating the force-distance curve. This measure for the stiffness is compared to a modeled curve, calculated using the Hertz model,[15] that would be expected for a conical indenter. The spring constant, necessary to relate the cantilever deflection with the applied force, is calibrated with the thermal noise method.[16]

The assumption of the Hertz model of an isotropic, smooth substrate with a Young's modulus independent of the applied force, is not met. Biological tissues tend to stiffen when they are deformed,[3, 4] and the many different types of fibers make the sample far from isotropic. However, by keeping the loading rate approximately constant amongst different experiments and using the same force-setpoint, 20 nN, the calculated values for the stiffness can still be used as a measure of the response of the tissue upon indentation. This "effective Young's modulus" will reflect the local mechanical properties of the tissue under the set experimental conditions and can be used to compare indentations on different types of tissue.

By performing the indentations on a regular grid, a stiffness map of the tissue, with a corresponding stiffness distribution, is made. All AFM measurements are performed in buffer at 37 °C (control, collagenase, chondroitinase + hyaluronidase, neutrophils) or 25 °C (control, elastase). For every case at least 2000 indentations on different locations have been performed.

Samples for Scanning Electron Microscopy (SEM) imaging have been prepared and incubated with enzymes with the same method as for the AFM measurements. After overnight incubation with the enzymes, the samples were put overnight in PBS with 2% glutaraldehyde (Sigma) at 4 °C. Afterwards, the samples where critical point dried and coated with a thin layer of gold-palladium (maximal 5 nm thick) and stored at room temperature until use. A field emission SEM (JEOL JSM-6700F) was used at 5.0 kV.

5.4 Results and Discussion

Figure 5.2 shows a stiffness map measured on the tunica media of a sample without any enzymes added. Each pixel of the stiffness map represents the stiffness calculated from a single indentation curve, with light colors indicating

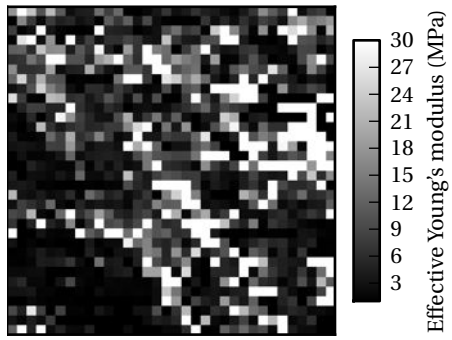

Figure 5.2:
Stiffness map measured on the tunica media of a sample without any enzymes added (113µm × 113µm, 34 × 34points). Stiffer pixels tend to be grouped in elongated patches which have an orientation that coincides with the fibers that are visible in the optical microscope integrated with the AFM.

large stiffness. The stiffness map shows that stiffer pixels tend to be grouped in elongated patches, which have an orientation that coincides with the fibers that are visible in the optical microscope integrated with the AFM. We combine multiple stiffness maps for every sample treatment into a single histogram, which reflects the distribution of stiffnesses within a sample. These histograms of the media and the adventitia are plotted in fig. 5.3, and show a clear change in effective Young's modulus for certain proteolytic treatments.

Figure 5.4 shows the two-photon images of the adventitia and media for the different proteolytic treatments we have performed. The two-photon images of the control show the difference in network structure between the media and adventitia. The adventitia consists of a densely woven network of collagen fibers, while the media consists mainly of parallel elastin fibers. The swelling stress of the proteoglycans, present in both layers of the arterial wall, puts the network, composed by the collagen and the elastin fibers, under tension.[17, 18] The small deformations made by the AFM tip mainly probe the tension on this combined network instead of the mechanical properties of the isolated fibers. The inhomogeneous distribution of proteoglycans across the vessel wall, showing a higher concentration in the media than in the adventitia,[19, 20] could give rise to the measured stiffer response in the media compared to the adventitia.[21, 22]

Digestion by elastase reveals the underlying collagen structure in the media and reduces the stiffness of the remaining tissue of the media, as was expected since elastin is one of its main components. The network structure and mechanics of the adventitia however remain unaltered by the elastin removal. Since the removal of elastin needed an incubation temperature of 25 °C, a control

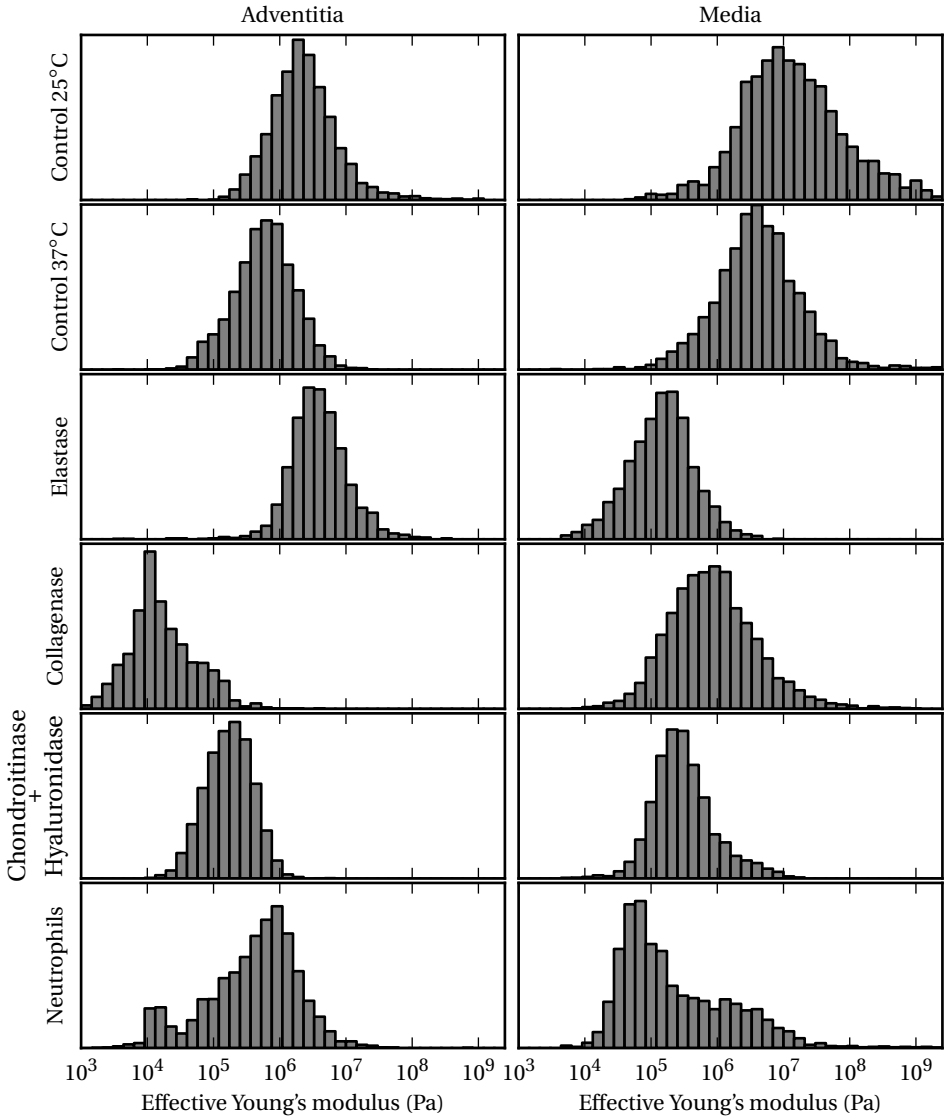

Figure 5.3:
Histograms showing the stiffness distribution of the porcine aortic wall after various proteolytic treatments. The plot shows a clear decrease in effective Young's modulus in certain conditions. For every condition at least 2000 indentations on different locations have been performed. All measurements have been performed at 37 °C, except for one control and the elastase treatment which have been performed at 25 °C. A maximum indentation force of 20 nN was used.

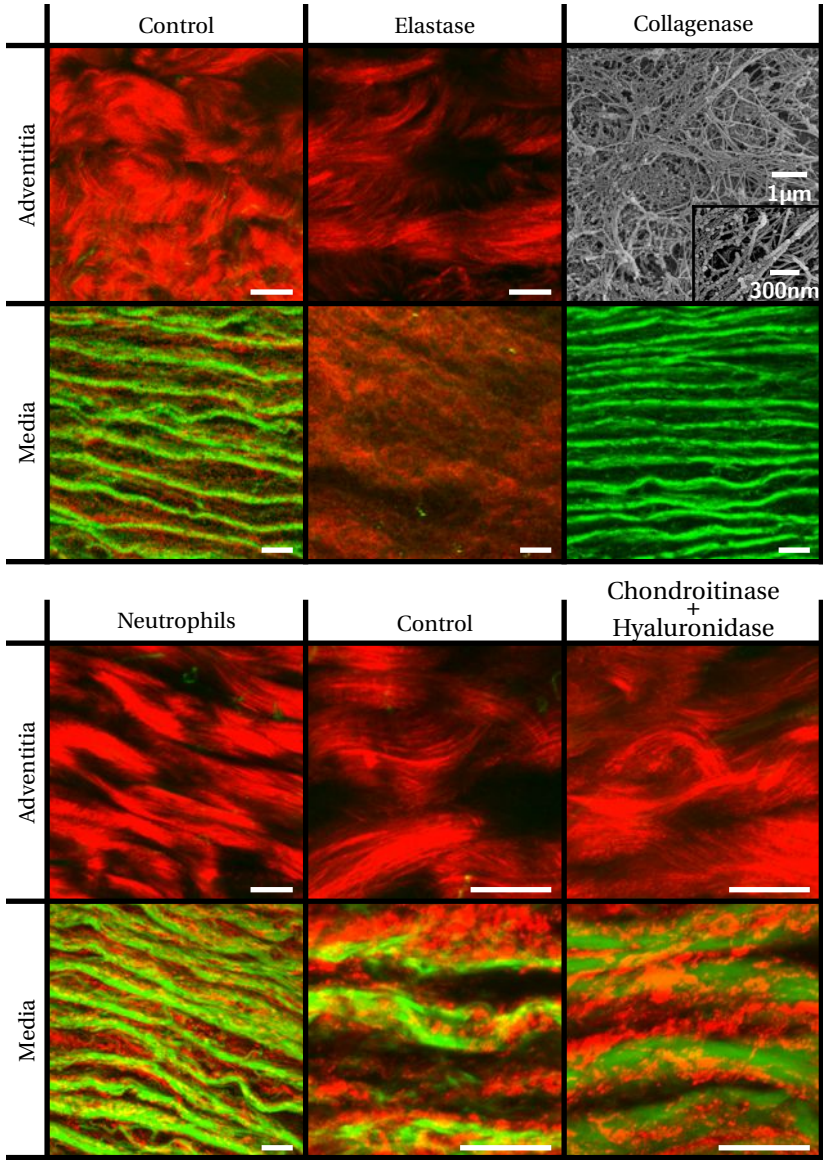

Figure 5.4:
Two photon microscopy images of the porcine aortic wall after various proteolytic treatments. Scale bars are 20µm. The images show a clear removal of the autofluorescence signal corresponding to elastin (green) or the SHG signal corresponding to collagen (red) fibers in certain conditions.
The adventitia did not give any signal after the collagenase treatment. Instead SEM images, at a higher magnification, of the remaining tissue are shown. Please note that, because the effects of chondroitinase and hyaluronidase treatments are expected to take place on a smaller length scale compared to the other treatments, the images of this treatment are made at a higher magnification. The sample used for the two photon experiments with the neutrophils had a four times as high penicillin-streptomycin concentration as is listed in table 5.1.

with this temperature has also been made. The observed small decrease in stiffness between the control sample left overnight at an incubation temperature of 37 °C, compared to an incubation temperature of 25 °C, is much smaller than the changes made by the proteolytic treatments.

Colagenase treatment weakens both layers. The weakening of the adventitia, an approximate 45-fold decrease in stiffness, is stronger than in the media, where the stiffness decreases by approximately a factor 3. Although two-photon imaging shows no collagen and elastin present in the digested adventitia, the AFM still feels a coherent network. SEM imaging confirms the existence of a remaining coherent network. The remaining structures have a large similarity with the structure of proteoglycans, which have been reported to be present in both layers of the aortic wall.[19, 20]

Removal of the proteoglycans by a mixture of Chondroitinase ABC and Hyaluronidase showed reduced stiffness of both media and adventitia. This decrease is modest compared to the collagenase treatment of the adventitia or the elastase treatment of the media, but it is still quite significant, considering that the two-photon images do not reveal any significant change in the network structure.

Different studies suggest that neutrophils are associated with degradation of the extracellular matrix. The large number of different enzymes, contained in neutrophils,[23] have been shown to be capable of removing proteoglycans,[24–26] collagen[27] and elastin[28] from the ECM. The visually unaltered collagen and elastin structure in the multi-photon images suggest that the concentration of collagen and elastin degrading enzymes is too low to significantly alter those networks. The AFM nano-indentation measurements, however, do show a weakening similar to the weakening of the tissue when the combination of Chondroitinase ABC and Hyaluronidase is applied. This could imply that there is a sufficient concentration of proteoglycan degrading enzymes in the neutrophil extract to alter these components of the ECM. The larger spread in measured stiffnesses could be the result of ECM degrading enzymes that do locally damage the collagen and elastin network.

A close look at the individual nano-indentation curves, depicted in fig. 5.5, shows additional information concerning the mechanical interaction on the fiber level. While untreated or unaltered tissue shows a steep increase of the force upon indentation, we find that when a main component of the extra cellular matrix is removed, eg. collagen from the adventitia, the elasticity of the tissue not only decreases, but also many drops in force are observed, which we interpret as breaking events (denoted by asterixes in fig. 5.5b–d).

A large number of indentation curves of the neutrophil treated adventitia show a piecewise linear increasing force upon indentation, indicating that the AFM tip pushes on an individual fiber instead of on a well connected network. The

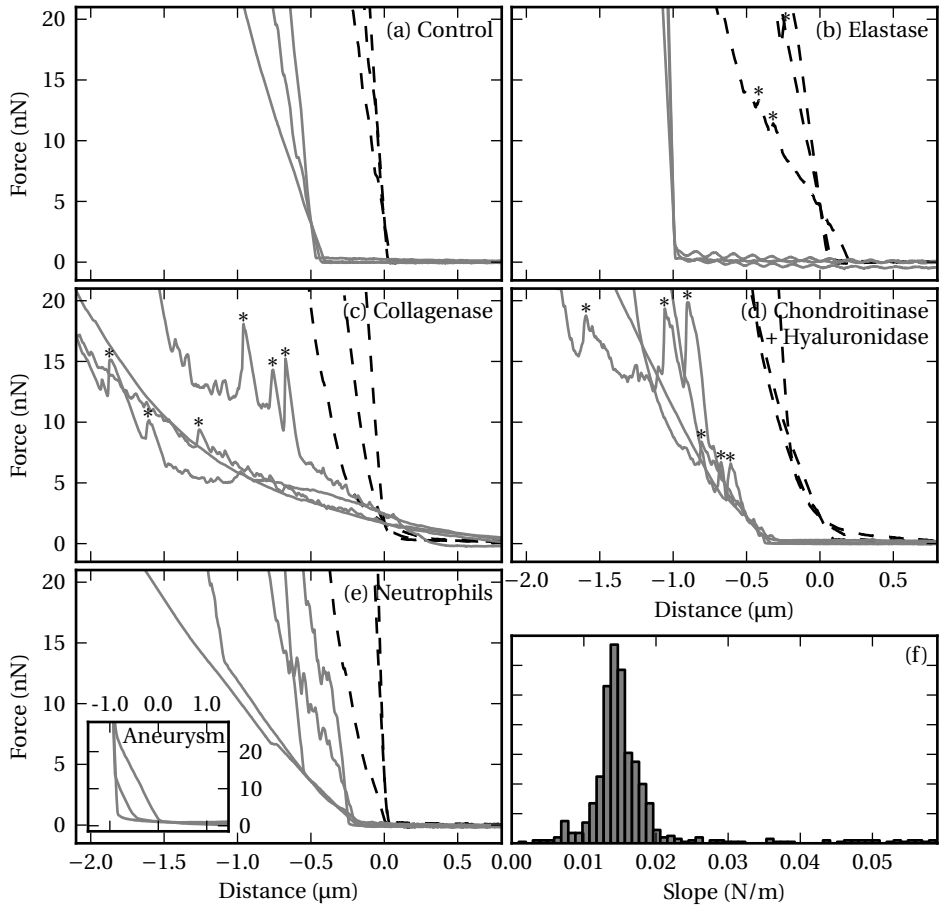

Figure 5.5:
(a-e) Representative nano-indentation curves after various proteolytic treatments of the adventitia (continous lines) and the media (striped lines) of the porcine aorta. Some of the breakage events are marked with a *. These curves gives a clear signal of the mechanical interaction on the fiber level. Untreated or unaltered tissue shows a steep increase of the force upon indentation. When a main component of the extra cellular matrix is removed, the elasticity of the tissue not only decreases, but also many drops in force are observed.
The inset of e) shows three representative nano-indentation curves measured on an aneurismatic aorta of a human donor (data taken from chapter 4[29]). In (e) a similar piecewise linear increase is measured on an adventitia treated with the contents of activated neutrophils.
(f) Histogram of slopes of the first increasing part of the nano-indentation curves of a neutrophil treated adventitia. The distribution shows a clear peak around 0.014N/m. The data of this graph is taken from one of the two locations on which the piece-wise linear increasing force was measured.

piece-wise linear curves of the neutrophil treated adventitia show a peak in the stiffness distribution, at 10^4 and at 10^5 Pa, depending on the stiffness of the AFM cantilever. This shows that the Hertz model does not apply for these curves because the slope of the force-distance curve is a measure for the ratio of the stiffness of the cantilever and the fiber on which it pushes and not for the Young's modulus of the sample.

A complicating factor of the neutrophil data arises from the fact that its action is consistently non-uniform. Only two out of five different 113µm × 113µm grids (from two independent experiments) on which the nano-indentation measurements were performed, showed the piecewise linear increasing force, while the other three grids did not, revealing an inhomogeneity of the tissue on larger length scales. However, some of the indentations on these three grids, did show a piece-wise linear decreasing force on the retracting part only of the indentation. The control measurements, taken on four different locations from two independent measurements, did not show any non-uniformity between the measurement locations. Alcian blue staining for proteoglycans, fig. 5.6, confirmed the emergence of inhomogeneity on a length scale larger than the scan-size of the AFM . At present we cannot attribute the non-uniformity to a specific blocking agent simply because we do not know which of the many components of the neutrophil extract is responsible for the observed change.

The sharp distribution of slopes of the first linear part after indentation, figure 5.5f, shows that the different fibers have the same stiffness. Previous studies on aneurysmatic tissue, chapter 4, showed a similar piecewise linear force increase upon indentation,[29] which is shown in the inset of fig. 5.5e. Aneurysms, a local dilatation of the arterial wall, are characterized by an inflammatory vessel wall, containing a highly elevated number of neutrophils.[30–32] The fact that an overnight incubation with the contents of activated neutrophils is enough to mimic the change in response from a healthy to an aneurysmatic tissue both in the stiffness and in the shape of the indentation curve, suggests that neutrophils may be responsible for the change in the mechanical properties of aneurysmatic aortic tissue of humans on the nanometer scale.

These measurements show how enzymes, secreted by cells, alter the mechanical properties of their surroundings. Other studies have shown that mechanical strain affects the ECM and enzyme production of cells. Vascular smooth muscle cells, for example, not only produce more fibronectin, collagen[33] and proteoglycans[34] when strained, the expression of the collagen degrading matrix metalloproteinase 2 is also increased.[33, 35] These effects, which strongly depend on the specific interactions between the cells and the ECM,[36] have also been shown in skin tissue,[37] synovial joints[38] and bone.[39, 40]

5.5 Conclusion

This study shows how the contribution of the individual components of the ECM to its mechanical properties is different for the adventitial and medial layers of the aorta. Although the removal of collagen, a key element of the ECM, is capable of reducing the local stiffness up to 50 times, the remaining tissue still forms a coherent network. The revealed micro-architecture and stiffness of the individual network components can be used as a basis for further theoretical studies, to better understand the interplay between fiber mechanics and the network organization.

Furthermore, we believe the significance of this study is demonstrated by the effect of the contents of activated neutrophils on the aortic wall. An overnight incubation with the contents of activated neutrophils is able to reproduce the change of local mechanical properties observed in aneurysms. Although this does not explain the previously observed remodeling of the collagen fibers on a larger length scale,[29] it is very well possible that the local change in mechanical properties, caused by the neutrophils, might trigger other cells to weave the new collagen fibers to repair the tissue in a different, less ordered, way. Further studies are needed to elucidate which components of the extra cellular matrix are altered by enzymes of the neutrophils and how this gives rise to a distinct response upon indentation.

We believe that this new way of studying the mechanical properties of the extra cellular matrix is not only valuable for physicists to get a better understanding of the mechanical properties of biopolymers, it will also help biomedical researchers to study processes like wound healing, atherosclerotic plaque development and cervix ripening. These are all processes in which the interaction between cells and their environment results in a remodeling of the extra cellular matrix.

5.6 Supporting material

In order to see whether proteoglycans could be at the origin for the observed non-uniformity in the adventitia after the treatment with the neutrophil extract, we stained samples, after incubation with either PBS or the neutrophil extract, for proteoglycans using alcian blue, fig. 5.6.

The alcian blue stained sample of the neutrophil treated tissue reveals bands of more intense staining in the adventitia that do not appear in the controls. The width of those bands, which exceed 100µm, are comparable to the area which is examined within one AFM measurement, which could explain why we do not see the piece-wise linear force curves in all measurements. We do not

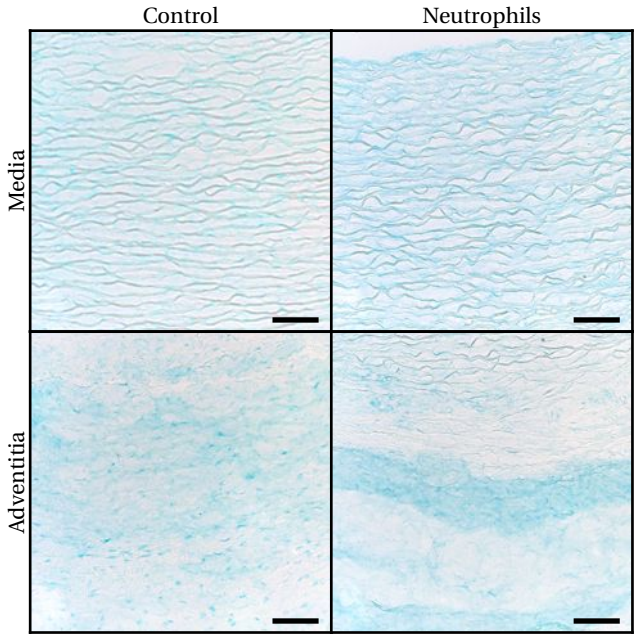

Figure 5.6:
Alcian blue staining of the media and adventitia of a control and neutrophil treated sample shows the presence of proteoglycans in both layers. The adventitia of the neutrophil extract treated sample shows bands with an increased staining.
Scale bars are 100µm.

know the mechanism that produces this non-homogeniety, but neutrophils are known to affect proteoglycans.[24–26] The increased staining could be caused by the cutting of large proteoglycans into smaller units, but could also be the result of unmasking: the enzymes removed some components from the ECM allowing more proteoglycans to be stained.

Methods

The samples have been prepared and treated with the enzymes as described section 5.3. After the overnight incubation with the enzymes, the buffer with the enzymes has been removed from the sample and the samples have been dried in air for 2 hours. Afterwards the samples are fixated by putting them 10 minutes in acetone and are stained in Alcian blue solution (Merck, Darmstadt, Germany) for 8 minutes. Subsequently they are rinsed three times by dipping them for 2 minutes in water. Afterwards they are dried in air and covered.

5.7 Acknowledgements

We thank T. Cerami for stimulating discussions, A. van der Laan and H. Tanke for their help and use of the two photon microscope, R. van Dijk for the movat stained arterial wall, J. Onderwater and A. Koster for their help and use of the SEM and P. Nibbering for the preparation of the contents of the activated neutrophils. This project is financially supported by a Netherlands SmartMix grant and the NIMIC partner organizations (www.nimic-project.com) through NIMIC, a public-private program.

5.8 References

[1] D. A. Vader, A. Kabla, D. A. Weitz, and L. Mahadevan. Strain-induced alignment in collagen gels. *arXiv*, cond-mat.soft:e5902, 2009.

[2] F. Backouche, L. Haviv, D. Groswasser, and A. Bernheim-Groswasser. Active gels: dynamics of patterning and self-organization. *Phys. Biol*, 3:264, 2006.

[3] I. K. Piechocka, A. S. G. van Oosten, R. G. M. Breuls, and G. H. Koenderink. Rheology of heterotypic collagen networks. *Biomacromolecules*, 12:2797, 2011.

[4] C. Storm, et al. Nonlinear elasticity in biological gels. *Nature*, 435:191, 2005.

[5] J. S. Bartholomew and J. C. Anderson. Investigation of relationships between collagens, elastin and proteoglycans in bovine thoracic aorta by immunofluorescence techniques. *Histochem. J.*, 15:1177, 1983.

[6] H. M. Walker-Caprioglio, et al. Organization of rat mesenteric artery after removal of cells of extracellular matrix components. *Cell Tissue Res.*, 264:63, 1991.

[7] M. R. Roach and A. C. Burton. The reason for the shape of the distensibility curves of arteries. *Can. J. Biochem. Physiol.*, 35:681, 1957.

[8] P. B. Dobrin and T. R. Canfield. Elastase, Collagenase, and the Biaxial Elastic Properties of Dog Carotid-Artery. *Am. J. Physiol.*, 247:H124, 1984.

[9] P. B. Dobrin, W. H. Baker, and W. C. Gley. Elastolytic and collagenolytic studies of arteries. Implications for the mechanical properties of aneurysms. *Arch. surg.*, 119:405, 1984.

[10] A. S. Hoffman and J. Park. Sequential Enzymolysis of Human Aorta and Resultant Stress-Strain Behavior. *Biomater. Artif. Cell*, 5:121, 1977.

[11] J. A. Kratzberg, P. J. Walker, E. Rikkers, and M. L. Raghavan. The effect of proteolytic treatment on plastic deformation of porcine aortic tissue. *J. Med. Behav. Biomed. Mater.*, 2:65, 2009.

[12] M. J. A. van der Plas, et al. Maggot excretions/secretions inhibit multiple neutrophil pro-inflammatory responses. *Microbes Infect.*, 9:507, 2007.

[13] A. Zoumi, X. Lu, G. Kassab, and B. Tromberg. Imaging coronary artery microstructure using second-harmonic and two-photon fluorescence microscopy. *Biophys. J.*, 87:2778, 2004.

[14] E. A-Hassan, et al. Relative microelastic mapping of living cells by atomic force microscopy. *Biophys. J.*, 74:1564, 1998.

[15] I. N. Sneddon. The relation between load and penetration in the axisymmetric Boussinesq problem for a punch of arbitrary profile. *Int. J. Eng. Sci.*, 1965.

[16] H. J. Butt and M. Jaschke. Calculation of Thermal Noise in Atomic-Force Microscopy. *Nanotech.*, 6:1, 1995.

[17] W. M. Lai, J. S. Hou, and V. C. Mow. A Triphasic Theory for the Swelling and Deformation Behaviors of Articular Cartilage. *J. Biomech. Eng.*, 113:245, 1991.

[18] A. I. Maroudas. Balance between swelling pressure and collagen tension in normal and degenerate cartilage. *Nature*, 260:808, 1976.

[19] T. N. Wight. Vessel proteoglycans and thrombogenesis. *PNAS*, 5:1, 1980.

[20] L. Y. Yao, et al. Identification of the proteoglycan versican in aorta and smooth muscle cells by DNA sequence analysis, in situ hybridization and immunohistochemistry. *Matrix Biol.*, 14:213, 1994.

[21] X. Guo, Y. Lanir, and G. S. Kassab. Effect of osmolarity on the zero-stress state and mechanical properties of aorta. *Am. J. Physiol. Heart Circ. Physiol.*, 293:H2328, 2007.

[22] E. U. Azeloglu, et al. Heterogeneous transmural proteoglycan distribution provides a mechanism for regulating residual stresses in the aorta. *Am. J. Physiol. Heart Circ. Physiol.*, 294:H1197, 2008.

[23] M. Faurschou and N. Borregaard. Neutrophil granules and secretory vesicles in inflammation. *Microbes Infect.*, 5:1317, 2003.

[24] Y. Matzner, et al. Degradation of heparan sulfate in the subendothelial extracellular matrix by a readily released heparanase from human neutrophils. Possible role in invasion through basement membranes. *J. Clin. Invest.*, 76:1306, 1985.

[25] D. Shum and S. Chan. Neutrophil-Mediated Degradation of Lung Proteoglycans. Stimulation by Tumor Necrosis Factor-alpha in Sputum of Patients with Bronchiectasis. *Am. J. Med. Sci.*, 2000.

[26] S. E. McGowan. Mechanisms of extracellular matrix proteoglycan degradation by human neutrophils. *Am. J. Respir. Cell Mol. Biol.*, 2:271, 1990.

[27] K. A. Hasty, et al. Human Neutrophil Collagenase - a Distinct Gene-Product with Homology to Other Matrix Metalloproteinases. *J. Biol. Chem.*, 265:11421, 1990.

[28] J. C. Powers, et al. Specificity of Porcine Pancreatic Elastase, Human Leukocyte Elastase and Cathepsin-G-Inhibition with Peptide Chloromethyl Ketones. *Biochim. Biophys. Acta*, 485:156, 1977.

[29] J. H. N. Lindeman, et al. Distinct defects in collagen microarchitecture underlie vessel-wall failure in advanced abdominal aneurysms and aneurysms in Marfan syndrome. *PNAS*, 107:862, 2010.

[30] J. R. Cohen, et al. Role of the neutrophil in abdominal aortic aneurysm development. *Cardiovasc. Surg.*, 1:373, 1993.

[31] M. B. Pagano, et al. Complement-dependent neutrophil recruitment is critical for the development of elastase-induced abdominal aortic aneurysm. *Circulation*, 119:1805, 2009.

[32] J. Eliason, et al. Neutrophil depletion inhibits experimental abdominal aortic aneurysm formation. *Circulation*, 112:232, 2005.

[33] C. O'Callaghan and B. Williams. Mechanical strain-induced extracellular matrix production by human vascular smooth muscle cells - Role of TGF-beta(1). *Hypertension*, 36:319, 2000.

[34] R. Lee, et al. Mechanical strain induces specific changes in the synthesis and organization of proteoglycans by vascular smooth muscle cells. *J. Biol. Chem.*, 276:13847, 2001.

[35] D. Seliktar, R. M. Nerem, and Z. S. Galis. Mechanical Strain-Stimulated Remodeling of Tissue-Engineered Blood Vessel Constructs. *Tissue Eng.*, 9:657, 2003.

[36] E. Wilson, K. Sudhir, and H. Ives. Mechanical Strain of Rat Vascular Smooth-Muscle Cells Is Sensed by Specific Extracellular Matrix/Integrin Interactions. *J. Clin. Invest.*, 96:2364, 1995.

[37] N. Bhadal, et al. The effect of mechanical strain on protease production by keratinocytes. *Brit. J. Dermatol.*, 158:396, 2007.

[38] G. Dowthwaite, et al. The effect of mechanical strain on hyaluronan metabolism in embryonic fibrocartilage cells. *Matrix Biol.*, 18:523, 1999.

[39] A. Kadow-Romacker, et al. Effect of Mechanical Stimulation on Osteoblast- and Osteoclast-Like Cells in vitro. *Cells Tissues Organs*, 190:61, 2009.

[40] M. Buckley, A. Banes, and R. Jordan. The effects of mechanical strain on osteoblasts in vitro. *J. Oral Maxil. Surg.*, 48:276, 1990.

6 Collagen cross-linking in atherosclerotic lesions

Part of this chapter will be submitted as:

The collagen cross-linking enzyme lysyl oxidase is associated with a stable phenotype of human atherosclerotic lesions

O. A. Ovchinnikova, L. Folkersen, J. W. M. Beenakker, J. Persson, J. H. N. Lindeman, T. Ueland, P. Aukrust, R. Hanemaaijer, N. A. Gavrisheva, E. V. Shlyakhto, G. Berne, P. S. Olofsson, U. Hedin, and G. K. Hansson

6.1 Abstract

Background Acute clinical complications of atherosclerosis such as myocardial infarction and ischemic stroke are usually caused by thrombus formation on the ruptured plaque surface. Collagen, the main structural protein of the fibrous cap, provides mechanical strength to the atherosclerotic plaque. The integrity of the fibrous cap therefore is likely to depend on collagen fiber cross-linking, a process controlled by the enzyme lysyl oxidase (LOX). We therefore investigate the LOX expression in human atherosclerosis and its effect on the stiffness of the fibrous cap.

Methods and results We studied atherosclerotic plaques from patients undergoing carotid endarterectomy. Lox protein was detected in areas of the plaque rich in smooth muscle cells (SMC) and collagen; higher LOX MRNA and protein levels were associated with a more stable phenotype of the plaque. Lox MRNA levels in carotid plaques predicted future myocardial infarctions among operated patients. A positive correlation was observed between MRNA levels of LOX and osteoprotegerin (OPG), and negative correlations between LOX MRNA and markers of inflammation. The amount of the mature, LOX-mediated collagen cross-links in plaques correlated positively with serum level of OPG and with the stiffness of the fibrous cap.

Conclusions Lox may contribute to the stabilization of atherosclerotic lesions and to the prevention of its lethal complications. Expression of LOX is negatively correlated with pro-inflammatory stimuli and positively correlated with OPG, suggesting that such mediators may control plaque LOX expression and hence plaque stability.

6.2 Introduction

Acute clinical complications of atherosclerosis such as myocardial infarction and ischemic stroke are caused by the thrombus formation on the plaque surface.[1, 2] The most frequent patho-anatomical substrate for sudden arterial thrombosis is a rupture of the fibrous cap that overlies the lipid core of the plaque.[1] Fibrillar collagens types I and III, synthesized by vascular smooth muscle cells (SMC), are abundantly present in the fibrous cap and are an important factor for the biomechanical stability of the plaque.[3] The strength of the fibrous cap depends not only on the amount of collagen, but also on cross-linking generated in the maturation of collagen fibers.[4]

Lysyl oxidase (LOX) is an extracellular copper-dependent enzyme that catalyzes the formation of aldehydes from lysyl and hydroxylysyl residues within the C- and N-terminal telopeptides of collagen fibrils. This reaction leads to the formation of covalent intermolecular mature cross-links, hydroxylysylpyridinoline (HP) and lysylpyridinoline (LP), which results in the insolubilization and stabilization of extracellular collagen.[5, 6] *Lox* gene deletion causes fetal death due to defects in the cardiovascular system including aortic aneurysms,[7] illustrating its importance for vascular pathophysiology.

Sites of atherosclerotic plaque rupture are characterized by the presence of activated macrophages, T cells, and mast cells that can influence collagen strength within the fibrous cap by producing pro-inflammatory cytokines, proteases, coagulation factors, radicals, and vasoactive molecules.[1] Interferon IFN-γ produced by Th1 cells strongly inhibits the proliferation of vascular SMCs and the production of interstitial collagens and LOX by these cells.[8–10] Other proinflammatory cytokines such as tumor necrosis factor TNF-α induce expression of collagenolytic proteases by activated macrophages and mast cells in plaques.[1, 11]

Atherosclerotic lesions of mice with increased T-cell activation have smaller fibrous caps and display reduced amounts of mature, cross-linked collagen due to inhibition of LOX by cytokines of activated T cells.[12] Interestingly, two risk factors for atherosclerotic heart disease, hypercholesterolemia and hyperhomocysteinemia, can decrease LOX levels in cells.[10, 13] Anti-inflammatory mediators are thought to protect atherosclerotic plaques from rupture by expanding the population of vascular SMCs in the fibrous cap and by augmenting collagen production and LOX-dependent cross-linking of fibers. Transforming growth factor TGF-β, platelet-derived growth factor (PDGF) and statins all increase LOX expression and activity in vascular SMCs.[10] Treatment of *Apoe-/-* mice with osteoprotegerin (OPG), a decoy receptor for the receptor activator of nuclear factor κB ligand (RANKL), promotes vascular SMC accumulation, LOX-dependent collagen fiber formation and development of fibrous caps.[14]

We hypothesized that LOX-dependent collagen cross-linking plays an important role by stabilizing the atherosclerotic plaque and preventing fibrous cap rupture. Therefore, we investigated LOX expression and its cytokine regulation in human atherosclerosis and its effect on the stiffness of the fibrous cap.

6.3 Methods

Human Specimen Collection The studies were approved by the respective ethics committees for human studies. Human atherosclerotic plaque tissue was obtained from the Biobank of Karolinska Endarterectomies (BIKE)[15] and from the

Biobank of St. Petersburg Investigation of Carotid Endarterectomies (SPICE) (table 6.4). Atherosclerotic plaques from carotid arteries were retrieved from patients during carotid endarterectomy, a surgical procedure in which material is removed from the inside of an artery, after providing informed consent. Pieces of carotid arteries were immediately frozen for RNA and protein extraction or embedded in TissueTek optical coherence tomography (OCT) compound (Sakura Finetek Europe BV, Zoeterwoude, the Netherlands) and frozen for immunohistochemistry. 157 cases in BIKE were used for RNA analysis and 24 cases from SPICE for protein analysis.

RNA analysis Total gene expression profiling was performed on 107 RNA samples from BIKE using Affymetrix Gene Array U133 Plus 2.0. All LOX analysis was based on the 215446_s_at probeset, which generated the highest signal values. Results from another probeset (204298_s_at) were similar, with a high correlation of 0.88. RNA from 157 human carotid endarterectomies from the same cohort was analyzed by real-time reverse-transcription polymerase chain reaction (rt-RT-PCR) as described previously.[16] There was an overlap of 77 samples between the microarray and rt-RT-PCR cohort. Primers and probes for human lysyl oxidase and cyclophilin A, a house-keeping gene, were purchased as assays-on-demand (Applied Biosystems). Expression of LOX mRNA as assessed by rt-RT-PCR had a high correlation with the expression of the 215446_s_at probeset (Pearson correlation coefficient, $r = 0.62$).

The population of SMCs in the atherosclerotic lesion exhibits extensive phenotypic diversity and plasticity.[17] SMCs in differentiated and dedifferentiated states differ morphologically and functionally, however it is difficult to clearly distinguish two populations based on existing SMC-markers. Therefore, to estimate the content of SMCs in atherosclerotic lesions we calculated the SMC-index that reflects the median of mRNA levels for all SMC-related genes as determined by gene expression array of total plaque mRNA (table 6.5).

Immunohistochemistry and immunofluorescence To localize LOX in human atherosclerotic plaques, series of single immunohistochemical and double immunefluorescent stainings were performed. The primary antibodies that were used included mouse polyclonal antibody generated against a synthetic peptide of human LOX (anti-LOX antibody)[18] (a generous gift from Professor Amato Giaccia, Department of Radiation Oncology, Stanford University, Stanford, CA); rabbit polyclonal antibodies to human von Willebrand factor (Dako), α-smooth muscle cell-actin (αSM-actin) (Abcam, Cambridge, UK) and collagen IV (Abcam); mouse monoclonal antibodies to human CD68 (Dako) and human CD163 (Dako); and a

mouse isotype control (Dako, Glostrup, Denmark). Immunohistochemical and fluorescent images were captured with a Leica DC480 color camera and with a Leica SP5X confocal microscope, respectively.

Western blot analysis Active LOX enzyme in 4 M urea extracts (5 µg of protein per lane) from carotid plaques was visualized by Western blots using anti-LOX antibody[18] diluted in 5% defatted dry milk/Tris-buffered saline/0.1% Tween 20. Optical density of the bands was measured using densitometry software, Fujifilm Image Gauge version 3.46.

Collagen analysis Picrosirius red staining was used for the assessment of collagen fibers in lesions.[19, 20] Briefly, 10 µm formaldehyde-fixed sections of carotid plaques were stained for 1 hour in saturated picric acid containing 0.1% picrosirius red (Direct Red 80, Fluka, Buchs, Switzerland). The color of collagen fibers when identified using Picrosirius Red staining depends upon fiber thickness and packing of collagen fibers; as fiber thickness or alignment increases, the color under polarized light changes from green to yellow and red.[21] All sections were analyzed under linear polarized light at magnification 200× in a Leica DRMB microscope and images were captured with a Leica DC480 color camera.

Collagen cross-link analysis Analysis of mature collagen enzymatic cross-links, hydroxylysylpyridinoline (HP) and lysylpyridinoline (LP)[5] and non-enzymatic cross-links, pentosidine, was performed on ten slices (10 µm) of frozen sections from individual carotid plaques by reverse-phase HPLC of amino acids and cross-links on a Micropak ODS-80TM column (150 mm×4.6 mm) (Varian, Palo Alto, CA) as described previously.[22, 23] The quantities of the enzymatic mature cross-links (HP+LP) were expressed as the number of residues per collagen molecule, assuming 300 hydroxyprolyl (Hyp) residues per triple helix given that the prolyl hydroxylation level in collagen is stable.

Enzyme-linked Immunosorbent Assay OPG, interleukin (IL)-6 and C-reactive protein (CRP) levels in serum and OPG in plaque tissue were measured with ELISA kits from R&D Systems (Minneapolis, MN). Neopterin was analyzed with an ELISA kit from BRAHMS (Hennigsdorf, Germany) and soluble RANKL with an Elisa from Peprotech (EC Ltd, London, UK) according to the manufacturer's instructions.

AFM nano-indentations The atomic force microscopy (AFM) nano-indentation experiments are performed as in ref. [23]. In short, measurements were done using a Molecular Imaging Picoscan AFM (Agilent Technologies, Palo Alto,

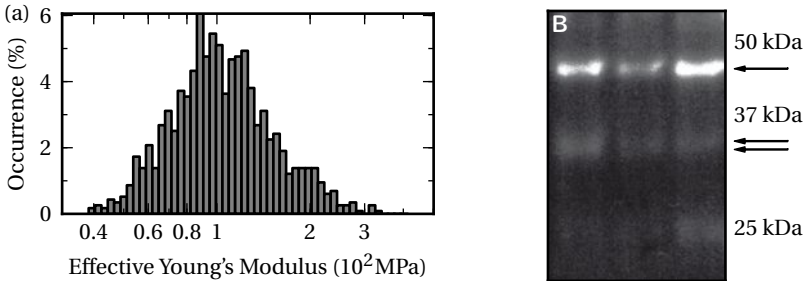

Figure 6.1:
(a) Histogram showing the distribution of measured Young's moduli on the fibrous cap of an atherosclerotic plaque. For every location more than 1000 indentations have been performed on a grid of 34×34 points, reflection the spread in stiffness of the 113 µm×113 µm probed area. The median of this distribution, 0.98×10^2 MPa for this measurement, is used as a representative measure for the stiffness of this location.
(B) Lox protein was detected in 4 M urea extracts from human carotid plaques by Western blot using mouse anti-human lysyl oxidase antibodies. Representative photograph of a Western blot membrane shows two Lox-specific bands: inactive proenzyme (around 48–50 kDa, single arrow) and active Lox enzyme (32 kDa, double arrow).

CA) controlled with a custom scripting program written in Labview (National Instruments, Austin, TX) and Visual Basic 6 (Microsoft, Redmond, WA). The nano-indentation was performed with a 2.0 N/m cantilever (Olympus OMCL type (Olympus, Hamburg, Gemany)) and was recorded with a National Instruments card at 100 kS/s. Matlab (The MathWorks, Natick, MA) was used to calculate the Young's modulus for each indentation using the FIEL method of Hassan et al.[24] This method calculates the work needed for a certain deformation by integrating the force-distance curve. This measure for the stiffness is compared to a modeled curve, calculated using the Hertz model,[25] that would be expected for a conical indenter. The spring constant of the cantilever, necessary to relate the cantilever deflection with the applied force, is calibrated with the Sader method.[26]

The assumption of the Hertz model of an isotropic, smooth substrate with a Young's modulus independent of the applied force, is not met. Biological tissues tend to stiffen when they are deformed,[27, 28] and the many different types of fibers make the sample far from isotropic. However, by keeping the loading rate approximately constant amongst different experiments and using the same force-setpoint, 100 ± 16 nN, the calculated values for the stiffness can still be used as a measure of the response of the tissue upon indentation. This "effective Young's modulus" will reflect the local mechanical properties of the tissue under the set experimental conditions and can be used to compare indentations on different types of tissue.

By performing the indentations on a regular grid, a stiffness map of the tissue,

with a corresponding stiffness distribution, is made. At every location at least 1000 indentations on a grid of 34×34 points have been performed. For every indentation the effective Young's modulus was calculated. The median of all the stiffness measurements was used as a representative measure for the local stiffness, fig. 6.1a.

Prediction of secondary events For each of the BIKE patients the following two adverse event categories were defined: 1) death, and 2) myocardial infarction. All event types were taken from the Swedish Hospital Discharge Register and the Swedish Cause of Death Register. The retrieval of myocardial infarction incidence data from the Swedish Hospital Discharge Register and the Swedish Cause of Death Register is a reliable, validated alternative to the use of revised hospital discharge and death certificates.[29] The follow-up time for patients free of myocardial infarction was 35 ±14 months for the rt-RT-PCR cohort and 22 ±13 months for the microarray cohort.

Statistical Analysis Spearman Rank Order Correlation was used to calculate the correlation coefficient and all correlations were adjusted for multiple comparisons by Bonferroni correction. The Mann-Whitney U test was used for comparisons between 2 groups in in vitro experiments. Values were expressed as mean ± std. Values of $p < 0.05$ were considered significant. Analysis of follow up data was done using cox-regression as implemented in the survival package[30] from the R programming language.[31]

6.4 Results

Expression of LOX in human atherosclerotic lesions

We investigated LOX mRNA and protein in perioperatively obtained samples of human carotid plaques. LOX mRNA was highly expressed in human carotid plaques; with microarray data, LOX mRNA was detected among the top 10% of all genes. Using rt-RT-PCR, LOX mRNA was detected at a Ct value of 26–30. Using specific anti-LOX antibodies[18] we were able to detect two forms of LOX: the proenzyme (approximately 48–50 kDa) and the 32 kDa mature enzyme in 4 M urea extracts from plaque tissues (fig. 6.1B).

Immunostaining of human atherosclerotic lesions demonstrated prominent LOX expression in the fibrous cap and in the areas surrounding the necrotic core (fig. 6.2A). Expression of LOX was observed either intracellularly within αSM-actin-positive SMCs (fig. 6.2B) or extracellularly, where it was localized in areas that

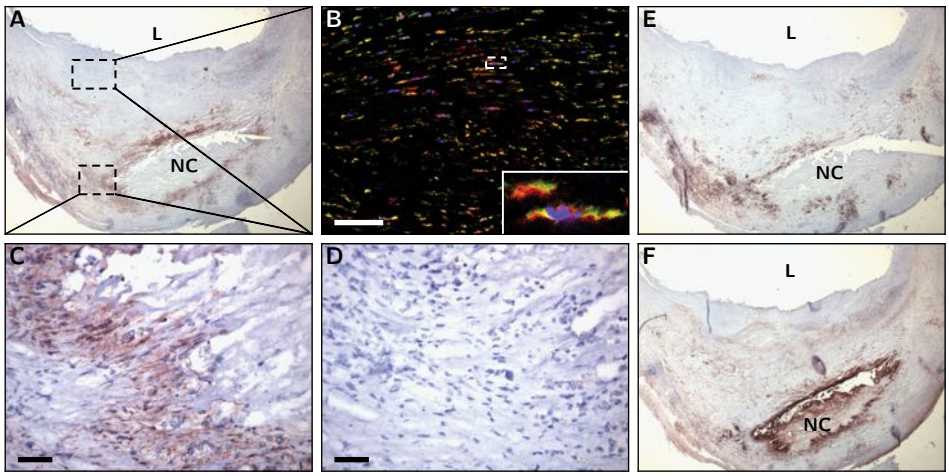

Figure 6.2:
Lox protein was localized in frozen sections of human carotid atherosclerotic plaques. Serial sections were stained with antibodies against Lox (A–C), αSM-actin (B), isotype control (D), CD163 (E) and CD68 (F). Immunoperoxidase micrographs (A, C–F) show specific staining in red and hematoxylin stained nuclei in blue, original magnification 25× (A,E,F) and 200× (C,D). In the immunofluorescent micrograph (B) αSM-actin is stained green, Lox is red, and colocalization of red and green results in yellow. Nuclei are stained blue with DAPI. Original magnification 400×. Scale bars are 50µm (B–D). L, lumen, NC, necrotic core.

contained thick mature collagen fibers, predominantly fibrillar collagens type I and III, and collagen type IV (fig. 6.3A–C,E). SMCs in the media of plaque-free vessel walls were generally Lox positive whereas the medial layer under the plaque contained predominantly Lox-negative SMCs (fig. 6.7). Lox protein was also detected in the immediate subendothelial space where it co-localized with collagen IV but not with von Willebrand factor-positive endothelial cells (fig. 6.3D–E). Lox protein co-localized with areas enriched with CD163+ macrophages (fig. 6.2A,E) and partially overlapped with CD68- positive areas (fig. 6.2A,F). However, expression of Lox varied within the lesions and between patients.

LOX is associated with a more stable phenotype of human plaques

Stable atherosclerotic plaque is characterized by an abundance of SMCs and mature fibrillar collagen type I and III in the fibrous cap.[3] Previous studies in the lab of prof. Hansson in atherosclerosis-prone mice revealed that higher Lox mRNA and protein levels associate with better collagen fiber quality, i.e. with a high proportion of thick, cross-linked collagen fibers in lesions.[12] To investigate whether Lox expression was associated with a more stable phenotype of human

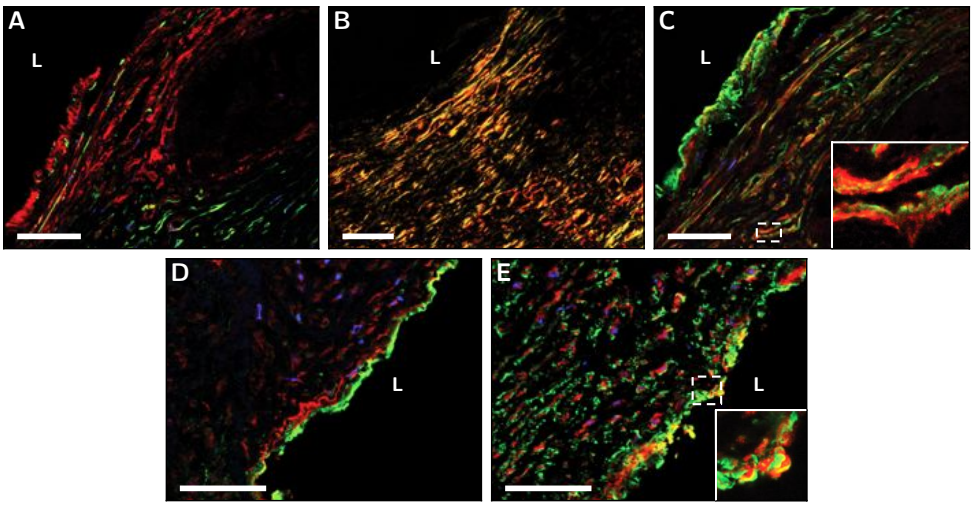

Figure 6.3:
Double immunofluorescent staining of frozen sections of human carotid plaques with antibodies against LOX (A,C–E) αSM-actin (A), collagen type IV (C,E), and von Willebrand factor (D). Lox is stained red; cell type markers and collagen IV are green; co-localization of red and green results in yellow color. Nuclei are stained blue with DAPI. Original magnification 400× (A–C) and 630× (D,E). (B). Micrograph shows section of human plaque stained with Picrosirius red dye for collagen fibers and visualized under polarized light. Original magnification 200×.
Scale bars are 50µm. L, lumen.

Transcript	Correlation, rho	p-value
SMC index	0.2	0.02
Procollagen α1(I)	0.51	< 0.001
Procollagen α1(III)	0.53	< 0.001
Procollagen α1(IV)	0.52	< 0.001
Prolyl 4-hydroxylase, α-subunit (P4HA)	0.51	< 0.001
Prolyl 4-hydroxylase, β-subunit (P4HB)	0.61	< 0.001
Lysyl-hydroxylase-2 (PLOD2)	0.6	< 0.001

Table 6.1:
Spearman rank correlation, rho, between MRNA levels of LOX and factors involved in collagen biosynthesis as analyzed by gene expression arrays of human carotid atherosclerotic lesions.

atherosclerotic lesions, we examined the correlation between the MRNA levels of LOX and MRNA for several markers of collagen biosynthesis in the human plaques. As shown in table 6.1, LOX MRNA correlated significantly with MRNA for three main procollagen types present in vascular tissue: procollagen type I, III and IV; it also correlated with MRNA for prolyl-4-hydroxylase and lysyl hydroxylase, enzymes that are important for cross-linking of collagen fibrils.[4]

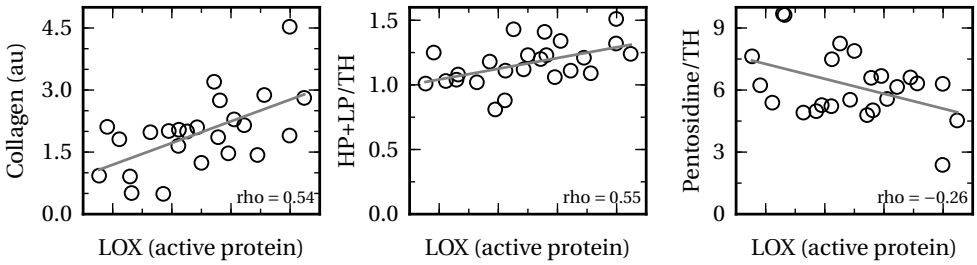

Figure 6.4:
Correlation between lysyl oxidase and collagen. Semiquantitative analysis of active LOX enzyme in human carotid plaques was performed by measuring optical density of the 32 kDa-band. Amounts of collagen and enzymatically induced cross-links (hydroxylysylpyridinoline (HP) and lysylpyridinoline (LP)) of mature collagen, and nonenzymatic pentosidine cross-links were determined in human carotid plaques by reverse-phase HPLC. Active LOX enzyme positively correlated with the percentage of collagen per mg of plaque tissue (left) and with the amount of mature enzymatic collagen cross-links per triple helix (TH) (pmol/pmol) (middle). It is negatively correlated with non-enzymatic cross-links, pentosidine (pmol/pmol) (right). Rho-Spearman rank correlation coefficient.

Transcript	Correlation, rho	p-value
OPG	0.6	< 0.001
CD74	−0.48	< 0.01
HLA-DR	−0.44	< 0.01
Lipocalin-2	−0.318	< 0.01
CD4	−0.3	< 0.01
RANKL	−0.26	NS
INF-γ	−0.1	NS

Table 6.2:
Spearman rank correlation, rho, between MRNA levels of LOX and markers of inflammation analyzed by gene expression arrays of human carotid plaques. NS indicates non significant results.

	OPG in serum (ng/ml)	OPG in tissue (ng/mg)	SRANKL in serum (pg/ml)	IL6 in serum (pg/ml)
Collagen	0.26	0.43*	0.001	−0.1
(HP+LP)/TH	0.48*	0.27	0.05	−0.3
Pentosidine/TH	0.2	0.05	0.11	0.2

Table 6.3:
Spearman rank correlation, rho, between systemic markers of inflammation, percentage of collagen (% per mg tissue), and mature collagen cross-links (pmol/pmol) in human carotid plaques.
$*p < 0.05$, TH-triple helix; mature insoluble collagen cross-links are hydroxylysylpyridinoline (HP) and lysylpyridinoline (LP).

Fibrogenic cells are the main source of LOX in tissues.[32] Therefore, we assessed whether LOX mRNA levels were dependent on the content of collagen-producing SMCs in plaques. To overcome great phenotypic diversity and plasticity of SMCs in lesions[17] we calculated a SMC index that reflected the median of mRNA levels for all SMC-related genes in vascular tissues (table 6.5). Although LOX mRNA correlated to the SMC index, the relationship was weak, suggesting that any changes of LOX expression in atherosclerotic plaque occur independently of SMC content (table 6.1 and fig. 6.8). We further evaluated whether LOX mRNA levels were associated with the amount of collagen in human atherosclerotic plaques. The amount of active LOX in plaques correlated positively with the amount of collagen and with the amount of mature collagen cross-links but negatively with non-enzymatic advanced glycation endproducts (AGE)-induced cross-links (pentosidine) (fig. 6.4).

LOX levels correlate negatively to factors associated with a proinflammatory phenotype of human plaques

To investigate if LOX was associated with vascular inflammation, we examined the correlation between the mRNA levels of LOX and several markers of inflammation in samples of carotid endarterectomies. As shown in table 6.2, LOX mRNA displayed significant positive correlation with OPG transcript levels and correlated negatively with mRNA levels for the MHC class II molecule HLA-DR and its invariant chain CD74, lipocalin-2 and the T-cell receptor associated protein CD4.

We further studied whether the quality of the collagen cap in human carotid plaques was associated with markers of systemic inflammation. The amount of mature collagen cross-links correlated positively with the systemic OPG level, but not with RANKL, IL-6, CRP or neopterin (table 6.3 and data not shown). Tissue OPG levels were associated with higher collagen content in carotid plaques (table 6.3).

Local LOX levels correlate to local stiffness of the extra cellular matrix

In a recent study by Hayenga et al., the atomic force microscope (AFM), has been used to show a stiffness difference between calcified and non-calcified regions of plaques in *ApoE-/-* mice.[33] In this study, we used the AFM to locally measure the stiffness on different locations on the fibrous cap of human patients and to correlate this to the amount of LOX and collagen.

The AFM measurements, summarized in fig. 6.5, show a positive correlation between the LOX concentration and the stiffness of the tissue. On the whole plaque level, we measure a positive correlation between the LOX and collagen concentration, fig. 6.4. The absence of a correlation within the fibrous cap between the sample stiffness and collagen concentration, shows that a local increase in LOX,

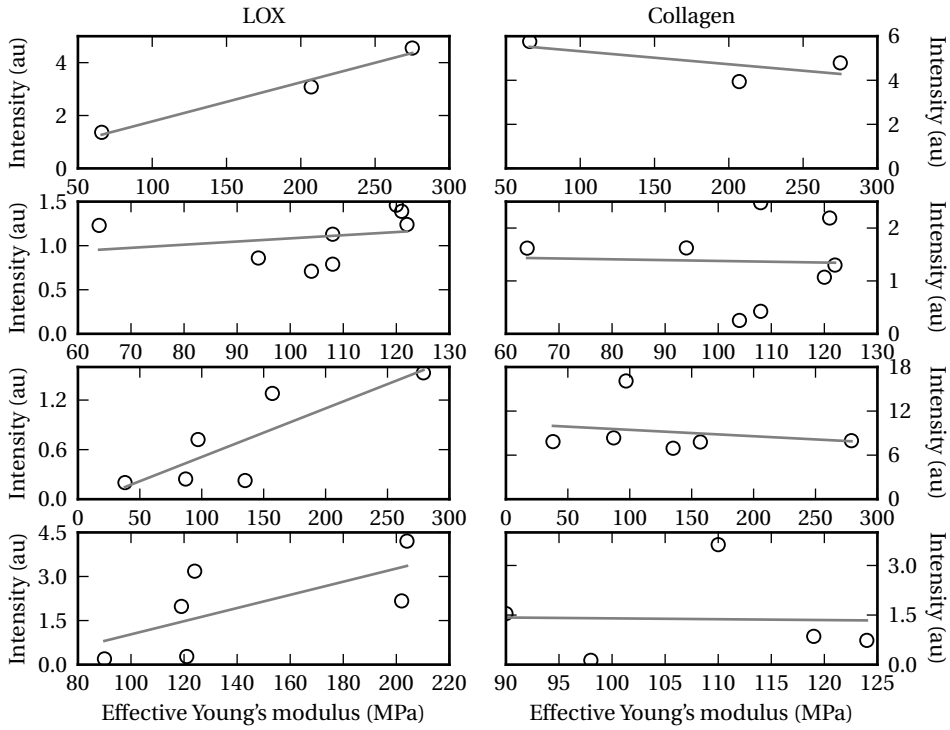

Figure 6.5:
Correlation between the tissue stiffness and lysyl oxidase (left) and collagen concentration (right) in four human carotid plaques. The stiffness was measured on various locations of the fibrous cap of four different plaques. On the same location, a semiquantitative analysis of active LOX enzyme and collagen concentration was performed by measuring the intensity of the LOX or collagen staining, made on subsequent coupes. These measurements show for every plaque a positive correlation between the Young's modulus and the LOX concentration. The absence of a correlation with the amount of collagen shows the minor influence of the local collagen concentration on the tissue stiffness, compared to the amount of LOX protein.

which cross-links the collagen, is sufficient to locally increase the stiffness of the tissue.

Local LOX levels were not correlated to historically reported symptoms

The LOX expression level was not associated with any of the reported clinical symptoms, including amaurosis fugax, transient ischemic attack or stroke, registered before the operation. The level of LOX MRNA and active LOX protein were not affected by gender, age, body mass index, plasma cholesterol level, or pharmacological treatment with statins or angiotensin-converting enzyme inhibitors in two studied populations (data not shown).

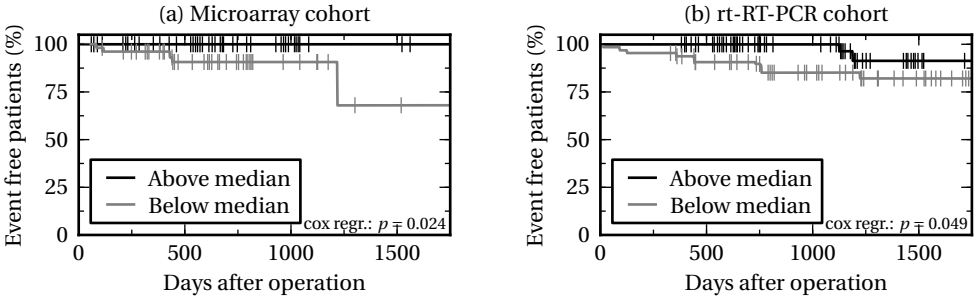

Figure 6.6:
Kaplan-Meyer plots for event-free survival from myocardial infarction in patients that had undergone carotid endarterectomy. The incidence of secondary myocardial infarctions in patients was determined using the Swedish Hospital Discharge Register and analyzed separately in patients with LOX mRNA expression above or below median in two BIKE cohorts: the microarray cohort (a) and the rt-RT-PCR cohort (b). Vertical lines indicate censored patients, i.e. the end of the follow-up period was reached without any event. The number of follow-up days after carotid endarterectomy is displayed on the x-axis.

LOX mRNA associated with better future outcome in patients with atherosclerosis

To investigate whether LOX mRNA levels were associated with the future outcome in carotid endarterectomy patients, we analyzed follow-up data for patients in the BIKE study. Data was analyzed from two subsamples of the BIKE cohort and stratified in tertiles by LOX expression. In the microarray subsample (69 patients), we found that higher LOX expression was associated with a significantly lowered incidence of myocardial infarction (cox regression coefficient of -1.20 ± 0.30, $p = 0.024$; patients with a LOX mRNA expression above median have a 1.20 times lower change to suffer from a myocardial infraction compared to the below median group) (fig. 6.6a). The ability to predict myocardial infarction was validated in a larger cohort of 157 samples using rt-RC-PCR measurements. In this cohort, the cox-regression coefficient was -1.46 ± 0.745, $p = 0.049$ (fig. 6.6b). Adjusting for age and gender effects gave similar results. No individual in the patient group with LOX expression above median was diagnosed with myocardial infarction within the follow-up period, while 12 individuals with LOX mRNA level below median suffered from myocardial infarction.

In total 12 deaths were registered in the BIKE cohort during follow-up period: three cases were related to cardiovascular pathology, one patient died of cancer, and the rest were unspecified. Lox transcript levels did not predict future death events.

6.5 Discussion

The present study provides evidence for an important role of LOX in the stabilization of the human atherosclerotic plaque. Higher LOX MRNA and protein levels were associated positively with markers of atherosclerotic plaque stability, i.e. collagen synthesis and a high proportion of thick, cross-linked collagen fibers, and negatively with pro-inflammatory markers that characterize a vulnerable plaque. We detected LOX protein in regions of the fibrous cap that were rich in collagen and SMCS and in areas surrounding the necrotic core. Moreover, LOX levels were associated with increased synthesis and sufficient maturation of fibrillar collagens type I and III in human carotid lesions. Furthermore, locally the stiffness of the fibrous cap correlated positively with the amount of LOX protein.

The expression of LOX in plaques was associated with clinical events. Although LOX levels were not associated with symptoms of acute brain ischemia reported before the endarterectomy, LOX does seem to be protective in the long-term follow-up. Patients with the highest LOX MRNA had fewer secondary myocardial infarctions. By catalyzing collagen cross-linking and the formation of thick collagen fibers with high tensile strength, LOX may contribute importantly to the mechanical strength of the plaque and counteract the risk for plaque rupture. The lack of association between LOX levels and past symptoms may reflect the natural course of plaque progression. The time between the onset of a symptom and the operation varied from one day to three months, implying that plaques were captured at different phases of the healing process. Recent studies suggest that LOX is expressed by endothelial cells and that LOX expression can be inhibited by several known atherosclerotic risk factors such as TNF, low density lipoproteins and homocystein.[10] We could not detect LOX positive endothelial cells overlying human atherosclerotic plaques; however, LOX expression co-localized with basement membrane collagen IV and with SMCS in the immediate subendothelial space. Given that collagen IV is one of the substrates for LOX,[5] we assume that such subendothelial distribution of the enzyme helps to stabilize the endothelial layer by maintaining the integrity of the basement membranes. The amount of immunoreactive LOX protein in the subendothelial space varied substantially between different samples, possibly reflecting the degree of endothelial dysfunction.

In the last few years, novel biological functions of LOX have been reported, including the control of cell migration, adhesion and gene regulation.[6] It was shown that that LOX can modulate the chemotactic sensitivity of vascular SMCS and monocytes.[34, 35] We identified LOX-positive areas in the regions surrounding the necrotic core and in areas rich with αSM-actin-positive SMCS and CD163+ macrophages. The haptoglobin receptor CD163 is a marker of “alternatively” acti-

vated (M2) macrophages with profibrotic and anti-inflammatory potential.[36, 37] Therefore, our findings may reflect a role for LOX in the recruitment of SMCs and M2 macrophages to the perinecrotic areas of plaques.

Impaired LOX-dependent collagen maturation has been suggested to play an important role in the pathogenesis of abdominal aortic aneurysms.[7, 38] We observed that the medial layer under the atherosclerotic plaque predominantly contain LOX-negative SMCs. Considering the notion that atherosclerotic plaques grow outwards during progression,[39] we speculate that the loss of LOX from medial SMCs promotes such an abluminal growth of the plaque.

The present findings in human atherosclerosis confirm and extend previous studies in mouse models, which demonstrated that excessive inflammation in atherosclerotic lesions leads to impaired fibrous cap formation by inhibiting LOX expression.[12]

In the human atherosclerotic plaque, LOX MRNA expression correlated negatively to MRNA for several markers of immune activity including CD74, HLA-DR, lipocalin-2 and CD4. CD74 is the invariant chain associated intracellularly with HLA class II molecules and CD4 is the HLA class II co-receptor expressed on T cells. Both molecules are crucial for immune activation and increased in inflamed regions of atherosclerotic plaques.[1, 40, 41] Their association with LOX confirms that local immune activity hampers plaque stability. Lipocalin-2, or neutrophil gelatinase-associated lipocalin (NGAL), is a glycoprotein found in neutrophil granules. It promotes MMP-9 activation and localizes in regions of atherosclerotic plaques with high proteolytic activity.[42] Together, these data imply that inflammation and proteolysis, conditions known to destabilize plaques, are associated with reduced LOX expression. This, in turn, supports the hypothesis that plaque inflammation promotes rupture[2] and suggests that reduction of LOX activity may contribute to the process.

Regions with higher LOX expression are stiffer compared to regions with lower LOX expression, confirming its stabilizing and strengthening effect on the collagen network. Further AFM studies could elucidate the effect of the various inflammatory systems on the collagen network and measure whether the spatial organization of the collagen has an influence on the fibrous cap strength.[23]

OPG is a soluble member of the TNF receptor superfamily and acts as a decoy receptor by inhibiting RANKL ligation.[43] Our recent findings provided evidence for atheroprotective and plaque stabilizing effects of OPG.[14] They suggested that OPG may exert biological effects not only by inhibiting RANK ligation but also by directly affecting collagen synthesis and LOX-dependent collagen maturation within atherosclerotic lesions.[14] Clinical studies show that RANK and its ligand are overexpressed in monocytes and T cells of patients with acute coronary syndromes.[44] Our present data show a positive association between OPG levels

and markers of stability in human atherosclerotic plaques: OPG mRNA levels correlated positively to LOX mRNA expression and the SMC index. Furthermore, we observed significant positive correlations between serum levels of OPG and enzymatic cross-links of mature collagen in the plaques. In light of this, we speculate that OPG may promote plaque stabilization by increasing collagen synthesis and LOX-dependent collagen maturation.

The levels of LOX protein and mature collagen cross-links did not correlate with circulating levels of soluble RANKL or proinflammatory cytokines such as IL-6. In view of the negative correlations between mRNA for LOX and those for a range of proinflammatory mediators in the plaque, it will be important to investigate additional inflammatory molecules for correlation with plaque levels of LOX and collagen in order to identify biomarkers for plaque stability.

Taken together, our present findings support a role for LOX in the stabilization of atherosclerotic plaques. By promoting collagen cross-linking and the formation of thick collagen fibers with high tensile strength, LOX may reduce the risk for plaque rupture and the development of lethal complications of atherosclerosis. The negative correlation between LOX and markers of plaque inflammation and immunity suggest that inflammatory mediators may counteract stabilizing the effects of LOX, possibly by acting directly on LOX expression. Further studies are warranted to evaluate LOX and LOX associated molecules as biomarkers and therapy targets for plaque stability.

6.6 Supplementary methods

RNA analysis Total gene expression profiling was performed on 107 RNA samples from BIKE using Affymetrix Gene Array U133 Plus 2.0. Samples for microarray analysis were hybridized and scanned at the Karolinska Institute Affymetrix core facility; obtained cel-files were preprocessed and log2-transformed using RMA-normalization.

Tissue samples and cells were lysed with RTL buffer (Qiagen, Valencia, CA). Total RNA was isolated with the RNeasy extraction kit (Qiagen) and reverse transcribed to CDNA using random hexamers and Superscript II reverse transcriptase (Life Technologies, Rockville, MD). MRNA levels were assessed by rt-RT-PCR in a TaqMan universal polymerase chain reaction master mix (Applied Biosystems, Foster City, CA). Primers and probes for human lysyl oxidase and cyclophilin A were purchased as assays-on-demand (Applied Biosystems). Samples were analyzed in duplicates with an ABI Prism 7700 Sequence Detector (Applied Biosystems). Results were normalized to values for human cyclophilin A.

Immunofluorescence Acetone-fixed sections were incubated with 5% horse serum followed by a mouse monoclonal anti-human lysyl oxidase antibody[18] (generous gift from Professor Amato Giaccia, Department of Radiation Oncology, Stanford University, Stanford, CA) or an isotype control (Dako, Glostrup, Denmark) and a polyclonal rabbit anti-human von Willebrand factor (Dako), rabbit polyclonal anti-human α-smooth muscle cell-actin (αSM-actin) (Abcam, Cambridge, UK) or rabbit polyclonal anti-human collagen IV (Abcam). Binding was detected with biotinylated horse anti-mouse antibody (Vector Laboratories, Burlingame, CA) followed by a Texas Redstreptavidin conjugate (Invitrogen, Carlsbad, CA) or a Alexa Fluor 488-conjugated goat anti-rabbit antibody (Invitrogen). Lipid autofluorescence was blocked with 0.03% Sudan black B (Sigma Aldrich) in 70% alcohol. Nuclei were visualized with DAPI (Sigma Aldrich), and images were viewed in a Leica fluorescence microscope and captured with a confocal microscope Leica DMI.

Immunohistochemistry 10 µm acetone-fixed sections of carotid plaques were stained by mouse monoclonal anti-human lysyl oxidase antibody[18] or an isotype control (Dako); monoclonal mouse anti-human CD68 (Dako); monoclonal mouse anti-human CD163 (Dako). Antibody binding was detected using ImmPress reagent kit/Peroxidase and visualized with Vector NovoRed substrate kit (Vector laboratories).

4 M urea LOX extraction and western blot analysis The active LOX protein is insoluble in neutral saline which likely reflects its tight association with its substrates in the extracellular space, but the enzyme can be rapidly solubilized by buffers supplemented with 4 to 6 M urea.[32] Therefore, multiple steps extraction was carried out at 0–4 °C similar to the one described previously.[45] Frozen samples of carotid plaques were cut into small pieces and homogenized for 2 min in 0.15 M-NaCl/0.016 M-potassium phosphate, pH7.7, at a ratio of 4 ml of buffer/g of ground tissue. The homogenate was incubated in ice for 30 min and centrifuged at 15000 g for 10 min, and the pellet was extracted once more with the new buffer. The two buffered salt extracts were discarded. The resulting pellet obtained from the salt extractions was further extracted with 0.016 M-potassium phosphate, and then with 4 M-urea in this phosphate buffer. The urea-soluble material was decanted and kept and the pellet was extracted once more with 4 M-urea/0.016 M phosphate. The two urea extracts were pooled and protein concentration was determined by bicinchoninic acid (BCA) protein assays (Thermo Fisher Scientific, Rockford, USA) with bovine serum albumin as a standard.

4 M urea extracts from carotid plaques (5 µg of protein per lane) were sepa-

rated by 12% sodium dodecyl sulfate-polyacrylamide gel electrophoresis under reducing conditions and blotted to hybridization transfer membrane Hybond-P (Amersham, Little Chalfont, UK). Blots were blocked and incubated with primary antibodies (mouse monoclonal anti-human lysyl oxidase antibody[18] and appropriate horseradish peroxidase-conjugated secondary antibodies diluted in 5% defatted dry milk/Tris-buffered saline/0.1% Tween 20). Immunoreactive proteins were visualized by the ECL Western blotting analysis system (Amersham). Optical density of the bands was measured using densitometry software Fujifilm Image Gauge version 3.46.

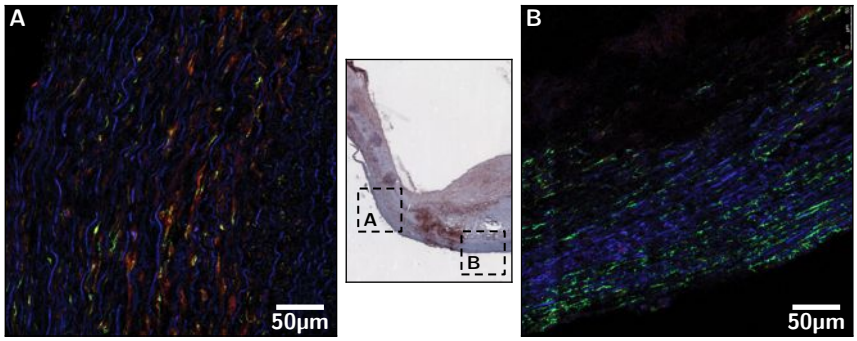

Figure 6.7:
Double immunofluorescent staining of frozen sections of human carotid plaques stained with antibodies against LOX (red) and αSM-actin (green); co-localization of red and green results in yellow; nuclei are stained blue with DAPI. LOX-positive SMCs dominate in plaque-free media (B), and LOX-negative SMCs are observed in the media under the plaque (B).
Original magnification 400×

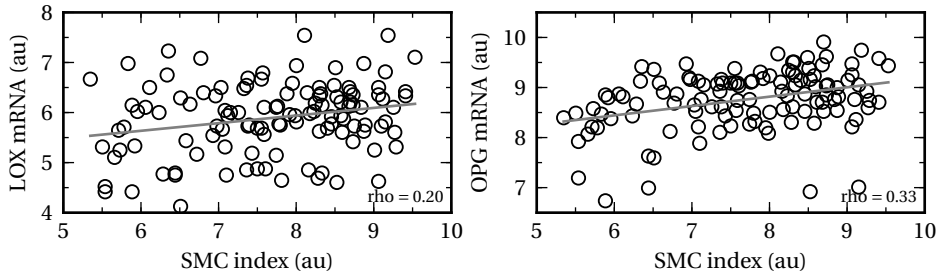

Figure 6.8:
Correlation between SMC index and mRNA levels of LOX or OPG analyzed by gene expression arrays of human carotid plaques. Rho-Spearman rank correlation coefficient.

Parameters	Values	
	BIKE	SPICE
Number of patines	107	106
Male/female	76.1% / 23.9%	79.2 % / 20.8%
Age, years (mean ± SD)	71.37 ± 8.61	62.6 ± 8.0
Pharmalocigal treatment:		
Antiplatelet agents	91.3%	79.5% ($n = 79$)
Statins	78.2%	32.9% ($n = 79$)
Angiotensin converting enzyme inhibitors	25.4%	59.5% ($n = 79$)
β-blockers	46.4%	49.4% ($n = 79$)

Table 6.4: General characterization of patients from the biobanks BIKE and SPICE.

Gene name	Transcript acc. nr.	Probe set ID
kruppel-like factor 5 (intestinal)	NM_001730	209211_at
kruppel-like factor 5 (intestinal)	NM_001730	209212_s_at
myocardin	NM_153604	237206_at
osteopontin	NM_000582	1568574_x_at
osteopontin	NM_000582	209875_s_at
platelet-derived growth factor receptor, α polypeptide	NM_006206	1554828_at
platelet-derived growth factor receptor, α polypeptide	NM_006206	203131_at
platelet-derived growth factor receptor, α polypeptide	NM_006206	211533_at
platelet-derived growth factor receptor, α polypeptide	NM_006206	215305_at
platelet-derived growth factor receptor, β polypeptide	NM_002609	202273_at
smoothelin	NM_006932	1556030_at
smoothelin	NM_006932	207390_s_at
smoothelin	NM_006932	209427_at
smoothelin-like 1	NM_001105565	230367_at
(SM 22) transgelin (TAGLN), transcript variant 1	NM_001001522	1555724_s_at
(SM 22) transgelin (TAGLN), transcript variant 1	NM_001001522	205547_s_at
(SM 22) transgelin (TAGLN), transcript variant 1	NM_001001522	226523_at
actin, alpha 1, skeletal muscle	NM_001100	203872_at
actin, alpha 2, smooth muscle, aorta	NM_001613	200974_at
actin, alpha 2, smooth muscle, aorta	NM_001613	215787_at
actin, alpha 2, smooth muscle, aorta	NM_001613	243140_at
homo sapiens transgelin 2 (TAGLN2)	NM_003564	200916_at
homo sapiens transgelin 2 (TAGLN2)	NM_003564	210978_s_at
myosin, heavy chain 11, smooth muscle	NM_002474	1568760_at
myosin, heavy chain 11, smooth muscle	NM_002474	201495_x_at
myosin, heavy chain 11, smooth muscle	NM_002474	201496_x_at
myosin, heavy chain 11, smooth muscle	NM_002474	201497_x_at
myosin, heavy chain 11, smooth muscle	NM_002474	207961_x_at
myosin, heavy chain 11, smooth muscle	NM_002474	228133_s_at
myosin, heavy chain 11, smooth muscle	NM_002474	228134_at

Table 6.5:
SMC-related genes that were analyzed by gene expression array of human carotid plaques and used to calculate SMC index. Transcript accession numbers are taken out of the NCBI database; Probe set ID corresponds to the Affymetrix Gene Array U133 Plus 2.0.

6.7 Additional measurements on plaques of the abdominal aorta

The disease of atherosclerosis affects all vascular beds including coronary, carotid, aorta and peripheral arteries.[47] Of these primary locations, surprisingly little is known about how atherosclerosis progresses in the aorta, the second largest manifestation of this disease.[48–52] This lack of information is remarkable, especially considering the fact that the aorta is generally used in rodent studies of atherosclerotic disease. A recent cardiovascular MRI study showed, that during the progression of atherosclerosis, the vessel wall area significantly increased for both the carotid artery and abdominal aorta (table 6.6).[46] The lumen area, however, did not change significantly for carotid arteries, but did significantly increase for the abdominal aorta. This difference in vascular remodeling could be the result of the difference in stiffness of the surrounding tissue, but could also have a more complicated origin. Furthermore, these measurements show a difference in plaque progression between different vascular beds.

In a large systematic histopathological study of 260 aortic samples, van Dijk et al. describe the development and progression of atherosclerosis in the abdominal aorta.[53] The results of this study, summarized in fig. 6.9, show how the initially thick fibrous cap thins and eventually ruptures. The mechanism of cap weakening and thinning is currently a controversial issue. Macrophages are thought to thin the cap by secreting enzymes that degrade the extracellular matrix.[3, 54–57] During the progression of the disease, the number of collagen producing smooth muscle cells declines, halting the production of collagen. Whether the primary cause of plaque thinning lies at the production or degradation side or both is a current issue of discussion.[54] Another line of theories on cap weakening is based on the mechanical aspects of plaques, e.g., the blood exerts a pulsed pressure on the cap which could weaken the cap.[58] A study by Bruke et al. provided evidence that silent plaque rupture could be a form of wound healing,[59] implying

	Baseline (mm^2)	Δ/year in %
Lumen	31.18 ± 8.98	-1.23 ± 12.34
Wall	25 ± 9.61	8.67 ± 35.54

Carotid artery

	Baseline (mm^2)	Δ/year in %
Lumen	259.63 ± 85.89	4.97 ± 15.86
Wall	103.48 ± 33.72	13.24 ± 17.36

Abdominal aorta

Table 6.6:
Annual progression rate of atherosclerosis and change in lumen size per year for the carotid artery ($n = 23$) and abdominal aorta ($n = 15$).[46] The wall area increased significantly for both the carotid artery and the abdominal aorta. The lumen area significantly increased for the abdominal aorta, but did not change significantly for the carotid arteries.

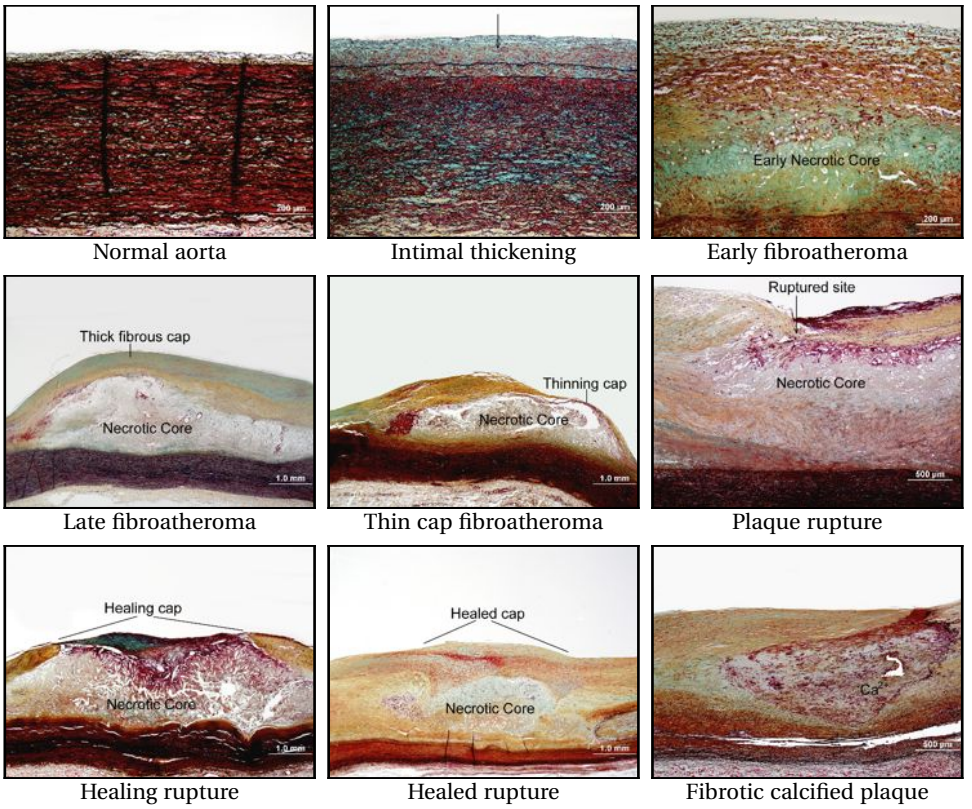

Figure 6.9: Development and progression of atherosclerosis in the abdominal aorta.[53]

that plaque thinning and rupture could sometimes also be beneficial.

In the remaining of this chapter, we show some preliminary data on atherosclerotic plaques of the abdominal aorta. Although the results of these measurements still needs to be verified on a larger number of samples, they do demonstrate how the AFM, in combination with multi-photon microscopy, can become a valuable tool to study the progression of atherosclerosis.

The ability of the AFM to measure spatial variations of the stiffness within an atherosclerotic plaque, could yield important information on the weakening of the collagen cap. Finite element simulations on the rupture of carotid plaques showed that calculated maximum plaque stresses were found to be significantly higher in patients with acute symptoms than those in recently symptomatic patients.[60, 61] These models can however be improved significantly if the local physical properties of these plaques are known.

Our preliminary AFM measurements show, fig. 6.10a, a ten-fold difference in

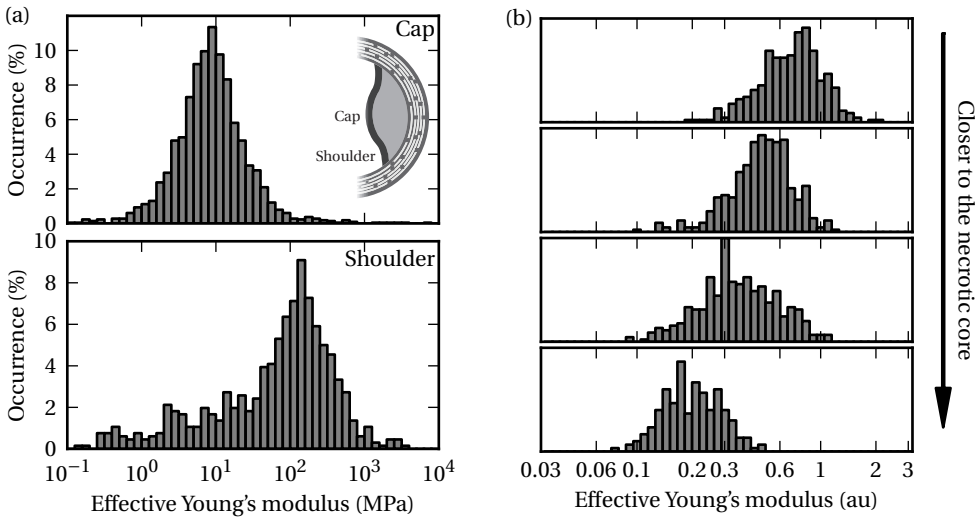

Figure 6.10:
AFM measurements on atherosclerotic plaques of the abdominal aorta.
(a) Stiffness measurements on the middle and the shoulder of the fibrous cap of the same plaque show a ten fold difference in stiffness, suggesting the middle of cap is weaker than the shoulder.
(b) Stiffness measurements made with a ball tip at various distances from the necrotic core show how the tissue gets weaker near the necrotic core.

the stiffness between the middle of the plaque and the plaque shoulder. These measurements seem to show that the mechanism for plaque rupture in the abdominal aorta is different than in the coronary arteries, where they tend to rupture in shoulder regions of the plaque.[62, 63] This difference could be the result of the difference in pressure and flow profiles between these arteries.

Multi-photon microscopy images of the collagen structure of a starting plaque, fig. 6.11a, show a thick barrier of multiple parallel collagen sheets, which preventing the contents of the necrotic core from entering the blood. Similar images of an older and thinner cap, fig. 6.11b, show how the collagen structure is disrupted. This damage is probably caused by the many collagen degrading enzymes of the necrotic core.[3, 54] This hypothesis is strengthened by our AFM measurements which, by probing the stiffness as a function of the distance to the necrotic core, fig. 6.10b, showed a significant weakening of the tissue near the necrotic core.

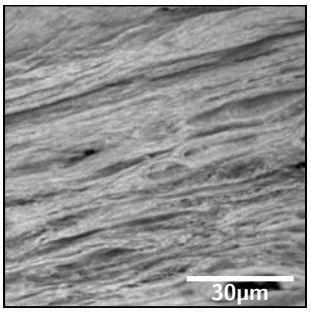

(a) Starting plaque (b) Old plaque

Figure 6.11:
Multi-photon microscopy images of the collagen cap of a starting (a) and old cap (b). The starting plaque shows a thick barrier of multiple parallel collagen sheets, which blocks the contents of the necrotic core from entering the blood. The collagen structure of the old cap, however, shows a disrupted collagen structure.

6.8 Acknowledgments

We thank Drs Vladimir V. Shlomin, Michail L. Gordeev, Vera A. Ovchinnikova and Olga M. Moiseeva for the help during collection of carotid plaque; Ingrid Törnberg and Anneli Olsson for technical assistance. Janneke Ravensbergen, Annemieke v/d Zalm and Rogier van Dijk for their help with the plaques of the abdominal aorta.

6.9 References

[1] G. K. Hansson. Inflammation, atherosclerosis, and coronary artery disease. *N. Engl. J. Med.*, 352:1685, 2005.

[2] P. Libby, P. M. Ridker, and G. K. Hansson. Progress and challenges in translating the biology of atherosclerosis. *Nature*, 473:317, 2011.

[3] E. Adiguzel, P. Ahmad, C. Franco, and M. P. Bendeck. Collagens in the progression and complications of atherosclerosis. *Vasc. Med.*, 14:73, 2009.

[4] K. Gelse, E. Pöschl, and T. Aigner. Collagens–structure, function, and biosynthesis. *Adv. Drug Deliv. Rev.*, 55:1531, 2003.

[5] D. R. Eyre, M. A. Paz, and P. M. Gallop. Cross-linking in collagen and elastin. *Annu. rev. biochem.*, 53:717, 1984.

[6] H. A. Lucero and H. M. Kagan. Lysyl oxidase: an oxidative enzyme and effector of cell function. *Cell. Mol. Life Sci.*, 63:2304, 2006.

[7] J. M. Mäki, et al. Inactivation of the lysyl oxidase gene Lox leads to aortic aneurysms, cardiovascular dysfunction, and perinatal death in mice. *Circulation*, 106:2503, 2002.

[8] G. K. Hansson, et al. Interferon gamma inhibits both proliferation and expression of

differentiation-specific alpha-smooth muscle actin in arterial smooth muscle cells. *J. Exp. Med.*, 170:1595, 1989.

[9] E. P. Amento, N. Ehsani, H. Palmer, and P. Libby. Cytokines and growth factors positively and negatively regulate interstitial collagen gene expression in human vascular smooth muscle cells. *Arterioscler. Thromb.*, 11:1223, 1991.

[10] C. Rodriguez, et al. Regulation of lysyl oxidase in vascular cells: lysyl oxidase as a new player in cardiovascular diseases. *Cardiovasc. Res.*, 79:7, 2008.

[11] C. M. Dollery and P. Libby. Atherosclerosis and proteinase activation. *Cardiovasc. Res.*, 69:625, 2006.

[12] O. Ovchinnikova, et al. T-Cell Activation Leads to Reduced Collagen Maturation in Atherosclerotic Plaques of Apoe(-/-) Mice. *Am. J. Pathol.*, 174:693, 2009.

[13] C. Rodríguez, et al. Low density lipoproteins downregulate lysyl oxidase in vascular endothelial cells and the arterial wall. *Arterioscler. Thromb. Vasc. Biol.*, 22:1409, 2002.

[14] O. Ovchinnikova, et al. Osteoprotegerin promotes fibrous cap formation in atherosclerotic lesions of ApoE-deficient mice–brief report. *Arterioscler. Thromb. Vasc. Biol.*, 29:1478, 2009.

[15] P. S. Olofsson, et al. Genetic variants of TNFSF4 and risk for carotid artery disease and stroke. *J. Mol. Med.*, 87:337, 2009.

[16] H. Qiu, et al. Expression of 5-lipoxygenase and leukotriene A4 hydrolase in human atherosclerotic lesions correlates with symptoms of plaque instability. *PNAS*, 103:8161, 2006.

[17] T. Yoshida and G. K. Owens. Molecular determinants of vascular smooth muscle cell diversity. *Circ. res.*, 96:280, 2005.

[18] J. T. Erler, et al. Lysyl oxidase is essential for hypoxia-induced metastasis. *Nature*, 440:1222, 2006.

[19] L. C. Junqueira, G. Bignolas, and R. R. Brentani. Picrosirius staining plus polarization microscopy, a specific method for collagen detection in tissue sections. *Histochem. J.*, 11:447, 1979.

[20] L. Rich and P. Whittaker. Collagen and picrosirius red staining: a polarized light assessment of fibrillar hue and spatial distribution. *Braz. J. Morphol. Sci.*, 22:97, 2005.

[21] D. Dayan, et al. Are the polarization colors of picrosirius red-stained collagen determined only by the diameter of the fibers? *Histochem.*, 93:27, 1989.

[22] R. A. Bank, et al. Sensitive fluorimetric quantitation of pyridinium and pentosidine crosslinks in biological samples in a single high-performance liquid chromatographic run. *J. Chromatogr. B Biomed. Sci. Appl.*, 703:37, 1997.

[23] J. H. N. Lindeman, et al. Distinct defects in collagen microarchitecture underlie vessel-wall failure in advanced abdominal aneurysms and aneurysms in Marfan syndrome. *PNAS*, 107:862, 2010.

[24] E. A-Hassan, et al. Relative microelastic mapping of living cells by atomic force microscopy. *Biophys. J.*, 74:1564, 1998.

[25] I. N. Sneddon. The relation between load and penetration in the axisymmetric Boussinesq problem for a punch of arbitrary profile. *Int. J. Eng. Sci.*, 1965.

[26] J. Sader, J. Pacifico, C. Green, and P. Mulvaney. General scaling law for stiffness measurement of small bodies with applications to the atomic force microscope. *J. Appl. Phys.*, 97:124903, 2005.

[27] I. K. Piechocka, A. S. G. van Oosten, R. G. M. Breuls, and G. H. Koenderink. Rheology of heterotypic collagen networks. *Biomacromolecules*, 12:2797, 2011.

[28] C. Storm, et al. Nonlinear elasticity in biological gels. *Nature*, 435:191, 2005.

[29] J. Merlo, et al. Comparison of different procedures to identify probable cases of myocardial

infarction and stroke in two Swedish prospective cohort studies using local and national routine registers. *Eur. J. Epidemiol.*, 16:235, 2000.

[30] survival: Survival analysis, including penalised likelihood, http://cran.r-project.org/web/packages/survival/index.html.

[31] Team RDC. *R: A Language and Environment for Statistical Computing* (R Foundation for Statistical Computing, Vienna, Austria, 2010).

[32] H. M. Kagan and W. Li. Lysyl oxidase: properties, specificity, and biological roles inside and outside of the cell. *J. Cell. Biochem.*, 88:660, 2003.

[33] H. Hayenga, A. Trache, J. Trzeciakowski, and J. D. Humphrey. Regional Atherosclerotic Plaque Properties in ApoE–/– Mice Quantified by Atomic Force, Immunofluorescence, and Light Microscopy. *J. Vasc. Res.*, 48:495, 2011.

[34] H. M. Lazarus, et al. Induction of human monocyte motility by lysyl oxidase. *Matrix Biol.*, 14:727, 1995.

[35] H. A. Lucero, et al. Lysyl oxidase oxidizes cell membrane proteins and enhances the chemotactic response of vascular smooth muscle cells. *J. Biol. Chem.*, 283:24103, 2008.

[36] F. O. Martinez, A. Sica, A. Mantovani, and M. Locati. Macrophage activation and polarization. *Front. Biosci.*, 13:453, 2008.

[37] S. K. Mathai, et al. Circulating monocytes from systemic sclerosis patients with interstitial lung disease show an enhanced profibrotic phenotype. *Lab. Invest.*, 90:812, 2010.

[38] K. Yoshimura, et al. Regression of abdominal aortic aneurysm by inhibition of c-Jun N-terminal kinase. *Nat. Med.*, 11:1330, 2005.

[39] S. Glagov, et al. Compensatory enlargement of human atherosclerotic coronary arteries. *N. Engl. J. Med.*, 316:1371, 1987.

[40] G. K. Hansson, L. Jonasson, J. Holm, and L. Claesson-Welsh. Class II MHC antigen expression in the atherosclerotic plaque: smooth muscle cells express HLA-DR, HLA-DQ and the invariant gamma chain. *Clin. Exp. Immunol.*, 64:261, 1986.

[41] J. L. Martín-Ventura, et al. Increased CD74 expression in human atherosclerotic plaques: contribution to inflammatory responses in vascular cells. *Cardiovasc. Res.*, 83:586, 2009.

[42] A.-L. Hemdahl, et al. Expression of neutrophil gelatinase-associated lipocalin in atherosclerosis and myocardial infarction. *Arterioscler. Thromb. Vasc. Biol.*, 26:136, 2006.

[43] S. Khosla. Minireview: the OPG/RANKL/RANK system. *Endocrinology*, 142:5050, 2001.

[44] W. J. Sandberg, et al. Enhanced T-cell expression of RANK ligand in acute coronary syndrome: possible role in plaque destabilization. *Arterioscler. Thromb. Vasc. Biol.*, 26:857, 2006.

[45] H. M. Kagan, K. A. Sullivan, T. A. Olsson, and A. L. Cronlund. Purification and properties of four species of lysyl oxidase from bovine aorta. *Biochem. J.*, 177:203, 1979.

[46] K. Hayashi, et al. Variations in atherosclerosis and remodeling patterns in aorta and carotids. *J. Cardiovasc. Magn. Reson.*, 12:10, 2010.

[47] K. Sutton-Tyrrell, et al. Subclinical atherosclerosis in multiple vascular beds: an index of atherosclerotic burden evaluated in postmenopausal women. *Atheroscler.*, 160:407, 2002.

[48] R. Virmani, et al. Lessons from sudden coronary death - A comprehensive morphological classification scheme for atherosclerotic lesions. *Arterioscler. Thromb. Vasc. Biol.*, 20:1262, 2000.

[49] M. Naghavi, et al. From vulnerable plaque to vulnerable patient: a call for new definitions and risk assessment strategies: Part I. *Circulation*, 108:1664, 2003.

[50] R. Virmani, et al. Effect of aging on aortic morphology in populations with high and low prevalence of hypertension and atherosclerosis. Comparison between occidental and Chinese communities. *Am. J. Pathol.*, 139:1119, 1991.

[51] Pathobiological Determinants of Atherosclerosis in Youth PDAY Research Group. Natural history of aortic and coronary atherosclerotic lesions in youth. Findings from the PDAY Study. . *Arterioscler. Thromb.*, 13:1291, 1993.

[52] F. D. Kolodgie, et al. Differential accumulation of proteoglycans and hyaluronan in culprit lesions: insights into plaque erosion. *Arterioscler. Thromb. Vasc. Biol.*, 22:1642, 2002.

[53] R. A. van Dijk, et al. The natural history of aortic atherosclerosis: A systematic histopathological evaluation of the peri-renal region. *Atheroscler.*, 210:100, 2010.

[54] P. Shah. Mechanisms of plaque vulnerability and rupture. *J. Am. Coll. Card.*, 41:15S, 2003.

[55] J.-O. Deguchi, et al. Matrix metalloproteinase-13/collagenase-3 deletion promotes collagen accumulation and organization in mouse atherosclerotic plaques. *Circulation*, 112:2708, 2005.

[56] C. L. Lendon, M. J. Davies, G. V. Born, and P. D. Richardson. Atherosclerotic plaque caps are locally weakened when macrophages density is increased. *Atheroscler.*, 87:87, 1991.

[57] V. Fuster, et al. Atherothrombosis and high-risk plaque: part I: evolving concepts. *J. Am. Coll. Card.*, 46:937, 2005.

[58] R. T. Lee, et al. Structure-dependent dynamic mechanical behavior of fibrous caps from human atherosclerotic plaques. *Circulation*, 83:1764, 1991.

[59] A. P. Burke, et al. Healed plaque ruptures and sudden coronary death: evidence that subclinical rupture has a role in plaque progression. *Circulation*, 103:934, 2001.

[60] U. Sadat, et al. Finite element analysis of vulnerable atherosclerotic plaques: a comparison of mechanical stresses within carotid plaques of acute and recently symptomatic patients with carotid artery disease. *J. Neur. Neurosurg. Psychiary*, 81:286, 2010.

[61] Z.-Y. Li, et al. Stress analysis of carotid plaque rupture based on in vivo high resolution MRI. *J. Biomech.*, 39:2611, 2006.

[62] K. C. Koskinas, et al. The role of low endothelial shear stress in the conversion of atherosclerotic lesions from stable to unstable plaque. *Curr. Opin. Cardiol.*, 24:580, 2009.

[63] M. T. Dirksen, et al. Distribution of inflammatory cells in atherosclerotic plaques relates to the direction of flow. *Circulation*, 98:2000, 1998.

7 Collagen remodeling and tumor micrometastasis in a zebrafish xenograft model

Part of this chapter is currently in press as:
Neutrophil-mediated experimental metastasis is enhanced by VEGFR inhibition in a zebrafish xenograft model
S. He, G. E. M. Lamers, J. W. M. Beenakker, C. Cui, V. P. S. Ghotra, E. H. J. Danen, A. H. Meijer, H. P. Spaink and B. E. Snaar-Jagalska
Journal op Pathology, 2012

7.1 Abstract

To study the dynamic and reciprocal interactions between tumor cells and their microenvironment, we used a xenograft model by injecting tumor cells into the blood circulation of transparent zebrafish embryos. This reproducibly results in rapid simultaneous formation of a localized tumor and experimental micrometastasis, allowing time-resolved imaging of both processes at single-cell resolution within one week. The tumor vasculature was initiated de novo by remodeling of primitive endothelial cells into a functional network. Roles of myeloid cells in critical tumorigenesis steps such as vascularization and invasion were revealed by genetic and pharmaceutical approaches. We discovered that the physiological migration of neutrophils controlled tumor invasion by conditioning the collagen matrix and forming the metastatic niche, as detected by two-photon confocal microscopy and second harmonic generation.

7.2 Introduction

The dynamic and reciprocal interactions between malignant tumor cells and the non-malignant cells in their microenvironment have a central role in tumor progression.[1, 2] Tumor cells secrete pro-angiogenic factors including the vascular endothelial growth factor (VEGF) to activate the endothelial cells of neighboring blood vessels and trigger angiogenesis to form tumor neovasculatures.[3] The tumor stromal cells, including fibroblasts and bone-marrow derived cells (MBDC), can secrete pro-angiogenic factors and control the angiogenic switch.[4, 5] Bone marrow-derived endothelial progenitor cells also participate in tumor vascularization by de novo vasculogenesis and/or direct incorporation into the tumor vasculature.[6, 7] Moreover, the myeloid lineages of BMDC are recruited by tumor cells to enhance their survival and aggressiveness.[3] The CD11+GR1+ myeloid cells, including immature dendritic cells, monocytes, neutrophils and early myeloid progenitors, promote tumor progression independent of the adaptive immune system and are essential mediators of the tumor refractoriness to anti-VEGF treatment.[7]

However, as these cells usually locate in deep tissues and can be functionally interfered by invasive detection methods, in vivo kinetic study of their actual roles in tumor progression remain challenging. Therefore, non-invasive visualization of the kinetic interaction between tumor cells and their microenvironment at high resolution will largely improve our understanding of the basic cancer biology and help to design new therapeutic strategies.

The zebrafish, Danio rerio, has been an important animal model for can-

cer, immune and stem cell research over the last decade.[8–11] Many molecular and cellular components that operate during tumorigenesis are conserved between zebrafish and mammals. A wide range of pharmacologically active compounds elicit physiological responses in zebrafish embryos comparable to those in mammalian systems,[12] making zebrafish ideal for identifying clinically relevant genes and compounds that regulate tumor progression. The transparency of zebrafish, in combination with the availability of various tissue-specific fluorescent reporter transgenic lines,[13, 14] allows high resolution in vivo analysis of tumor progression and the interactions between tumor cells and the host microenvironment.[15, 16] Several tumor transplantation assays with human and mammalian cells have been developed to study different aspects of tumor malignancies in embryo and adult zebrafish, such as tumor cell migration, proliferation, angiogenesis and tumor cell extravasation.[13, 15–19] However, most of these assays are limited to one selected step of tumor development and do not represent the full complexity of tumorigenesis in one model. In addition, for zebrafish embryonic engraftment models there are no reports published describing tumor cells extravasation from the circulation and invasion into the surrounding tissue where cells proliferate to form experimental metastases.

We have established a rapid, reproducible zebrafish embryonic xenograft model for simultaneous formation of a localized tumor and experimental micrometastasis by intravascular injection of tumor cells into the blood circulation of zebrafish embryos. With non-invasive high-resolution imaging we characterized the critical steps of tumor progression, including tumor vascularization and tissue invasion. Using this model, we found that myeloid cells are involved in these tumor processes, and especially that neutrophils condition the collagen matrix to facilitate metastatic niche formation and tumor invasion.

7.3 Results

Intravascular injection of tumor cells into zebrafish embryos resulted in localized tumor growth and micrometastasis within 6 days

In order to develop an experimental metastasis model, as frequently used in mice, we implanted up to 400 fluorescent tumor cells into the blood circulation of zebrafish embryos at 2 day post fertilization (dpf). The tumor cells hematogenously disseminated in the embryo immediately after injection into the duct of Cuvier, a wide circulation channel on the embryonic yolk sac connecting the heart to the trunk vasculature (fig. 7.1A,B). When > 100 tumor cells were injected, the embryonic circulation was not sufficient to disseminate the entire bulk of implanted cells, resulting in the accumulation of non-disseminated cells close

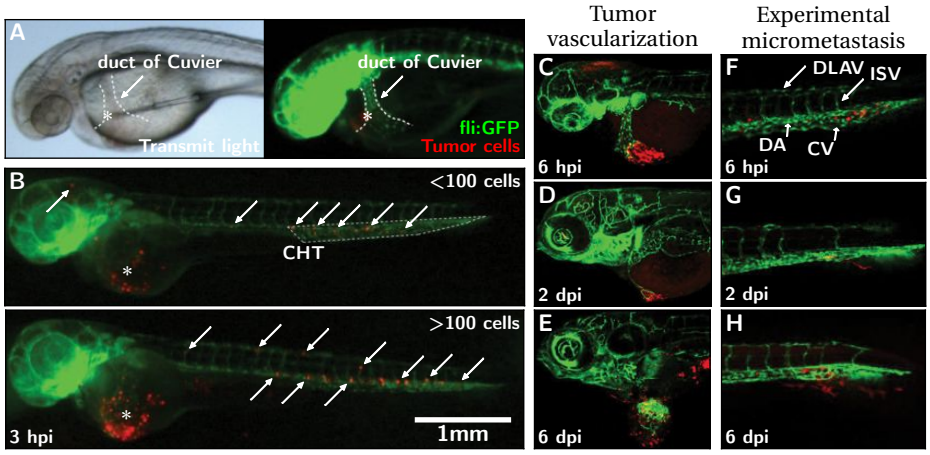

Figure 7.1:
(A) Bright field (left) and fluorescence (right) images showing the injection of tumor cells (red) into the zebrafish embryonic circulation (green) via the ventral side of the duct of Cuvier.
(B) Dissemination of implanted tumor cells in embryos injected with ≤ 100 (top) or > 100 cells. Dissemination was observed in almost all embryos (124/125) at 3 hours post implantation (hpi). The injection sites are indicated by * and disseminated tumor cells are indicated by arrows. The caudal hematopoietic tissue (CHT) is outlined (top). Note that tumors also accumulated close to the injection site in the example of an embryo injected with > 100 cells (bottom).
(C–E) Progression of tumor formation. Tumor cells accumulated close to the injection site at 6 hpi (C), induced formation of neovasculature at 2 days post implantation (dpi) (D), and displayed localized tumor growth at 6 dpi (E).
(F–H) Formation of micrometastases. Disseminated tumor cells resided in the tail at 6 hpi (F), invaded into the neighboring tail fin at 2 dpi (G), and formed micrometastasis colonies in the fin tissue at 6 dpi (H).
Red in A,B&E: tumor cells labeled with the red cell tracker CM-DiL.; Red in C,D,F–H: tumor cells stably expressing dsRed. Green in all: GFP-endothelial cells of the Tg(Fli:GFP) line. Abbreviations: DLAV: dorsal longitudinal anastomotic vessel; ISV: intersegmental vessel; DA: dorsal aorta; CV: caudal vein.

to the injection site at the duct of Cuvier (fig. 7.1B). Using a Tg(Fli:GFP) endothelial reporter transgenic zebrafish line with fluorescent vasculature,[13] we found that the accumulated tumor cells induced neovasculature formation and developed into a localized tumor (fig. 7.1C-E), whereas the disseminated tumor cells formed micrometastic colonies in the trunk of the fish (fig. 7.1F-H). Localized tumor growth and experimental micrometastases were also induced by several other types of mouse- or human-originated tumorigenic cell lines, but never by non-malignant cell lines (table 7.1). This novel experimental metastasis assay bypasses the primary tumor stage and intravasation, but opens the possibility to use this model to screen for anti metastatic agents in a few days instead of weeks in rodent models.

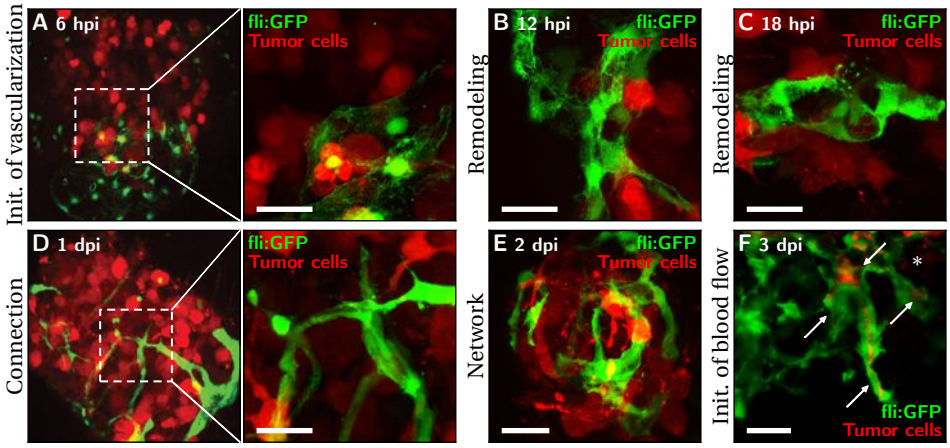

Figure 7.2:
(A–E) Initiation of tumor-induced neovasculature. Fli:GFP embryos were imaged from the ventral side to achieve a top view of dsRed labeled FGF-T-MAE tumor cells, which, after implantation, accumulated under the primitive endothelial cells of the duct of Cuvier (A, 6 hpi, with magnification in the right panel). At 12 hpi, the primitive endothelial cells in close association with the tumor cells started to change morphology (B). At 18 hpi, the primitive endothelial cells were remodeled into vessel-like structures (C; 3 connected GFP-endothelial cells). The remodeled endothelial cells were further connected within the tumor cell mass at 1 dpi (D, with magnification in the right panel). At 2 dpi, a partially lumenized vasculature network had formed within the tumor cell mass (E).
(F) Microangiography with tetramethylrhodamine dextran showing partial blood flow in the tumor vessels at 3 dpi (red, indicated by arrows). Some leakage of the tumor vessels was also observed (*).
Scale bars: 25 µm.

Cell line	Description	Vascularization/localized tumor growth	Tumor invasion/micrometastasis	*n*
KFGF-T-MAE	MAE cells transformed by FGF2 over expression	97.0%	32.8%	67
4T1	Mouse breast cancer	64.7%	15.5%	142
MDA-MB-231	Human breast cancer	0%	47.9%	48
PC3	Human prostate cancer	25.0%	0%	60
MAE	Mouse endothelial	0%	0%	>100
ZF4/PAC2	Zebrafish fibroblast cell lines	0%	0%	>100

Table 7.1:
The migratory potential of various tumor cells. For every tumor cell type the cells have been implanted in *n* different fish at 2 days post fertilization (dpf). 6 day post implantation the fish were scored for vascularization/localized tumor growth and tumor invasion/micrometastasis. (data not shown[20])

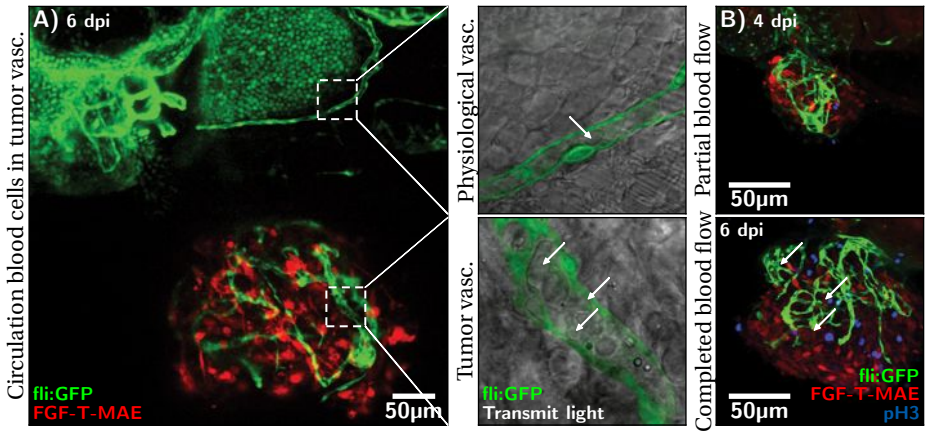

Figure 7.3:
(A) An expanded tumor mass of FGF-T-MAE-mCherry cells, supported by a functional vasculature-network, at 6 dpi. The right panel shows magnifications of a pectoral fin vessel (top) and a tumor vessel (bottom). Circulating blood cells within the vessels are indicated by arrows (overlay of transmitted light and GFP channel).
(B) Phosphohistone H3 (pH3, blue) staining of Fli:GFP embryos implanted with FGF-T-MAE-mCherry cells. The pH3+ staining, as a marker of proliferation, was increased in both mCherry+ and mCherry- cell populations after 4 dpi, when circulating blood cells started to be detected in the tumor neovasculature.

Tumor vascularization is the critical step for localized tumor growth

Taking advantage of the transparency of zebrafish embryos, we performed high-resolution confocal imaging to characterize the localized tumor growth. Shortly after implantation, the non-disseminated tumor cells locally accumulated in close association with the primitive endothelial cells of the duct of Cuvier (fig. 7.2A), which were subsequently remodeled into neo-vessel-like structures by the tumor cells (fig. 7.2B,C). Subsequently the neo-vessels connected and gradually formed an irregular, tortuous, lumenized vasculature network within 2 days (fig. 7.2D,E). Partial blood flow was detected in the tumor vasculature by microangiography from 3 days post implantation (dpi) (fig. 7.2F) and circulating erythrocytes were observed in the lumen after 4 dpi (fig. 7.3A).

Notably, only in the embryos where such functional tumor neovasculature had formed, the localized tumor cells expanded into a tumor mass of > 0.15 mm diameter by 6 dpi. Phosphorylation of histone H3 (pH3), a proliferation marker, significantly increased in both fluorescence-positive tumor cells and fluorescence-negative stromal cells of the localized tumor mass after 4 dpi (fig. 7.3B), when the tumor vasculature started to be functional. These results indicate that suc-

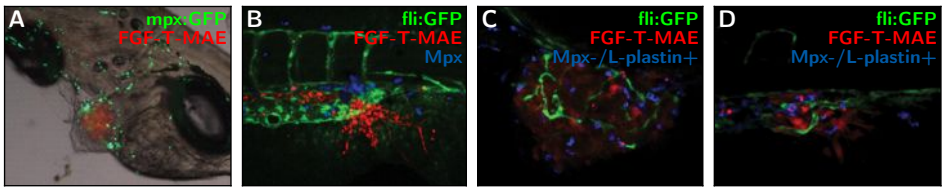

Figure 7.4:
(A) Neutrophils (green, Tg(mpx:GFP)^{i114}) associated with FGF-T-MAE tumor cells (red) at the localized tumor growth site.
(B) Neutrophils (blue, Mpx+ histochemical staining) associated with the tumor cells (red) at the micrometastasis site.
(C–D) Macrophages (blue, Mpx-/L-lpastin+) associated with the tumor cells (red) at the localized tumor (C) and the micrometastasis (D) sites.

cessful tumor vascularization was the critical step for localized tumor growth in our model. Importantly, this de novo, tumor induced vascularization represents a totally different phenomenon than a previously described angiogenesis assay, which monitors growth of new vessels from existing vessels towards tumor implant.[21]

Myeloid cells are involved in tumor vascularization and invasion

Leukocytes are known to contribute to different steps of tumor progression including the formation of tumor vasculature and metastasis.[2, 4, 5, 7] In zebrafish embryos, the caudal hematopoietic tissue (CHT) is known as a transient site of hematopoiesis and leukocyte differentiation.[17] Our observation that tumor cell invasion occurred at the posterior end of the CHT suggested involvement of leukocytes in tumor progression. In the first few days of zebrafish development, macrophages and neutrophils are the only populations of functional leukocytes in the embryos.[18] Using a combination of myeloid lineage markers (Mpx+ for neutrophils and Mpx-/L-plastin+ for macrophages[19]) we detected that FGF-T-MAE tumor cells were accompanied by cells of the myeloid lineages both at the localized tumor growth site near the site of implantation, and at the invasion site at the posterior end of the CHT (fig. 7.4).

To investigate the role of myeloid cells in tumor progression, we used morpholino oligonucleotides to knockdown the transcription factor Pu.1, which controls the development and differentiation of myeloid cells in zebrafish embryos.[22] As previously shown, Pu.1 knockdown is most effective in suppressing macrophage differentiation; while neutrophil differentiation can be suppressed only under maximal knockdown conditions.[23] In agreement, in our experiments macrophages were depleted in zebrafish embryos up to 3 dpf by a partial knock-

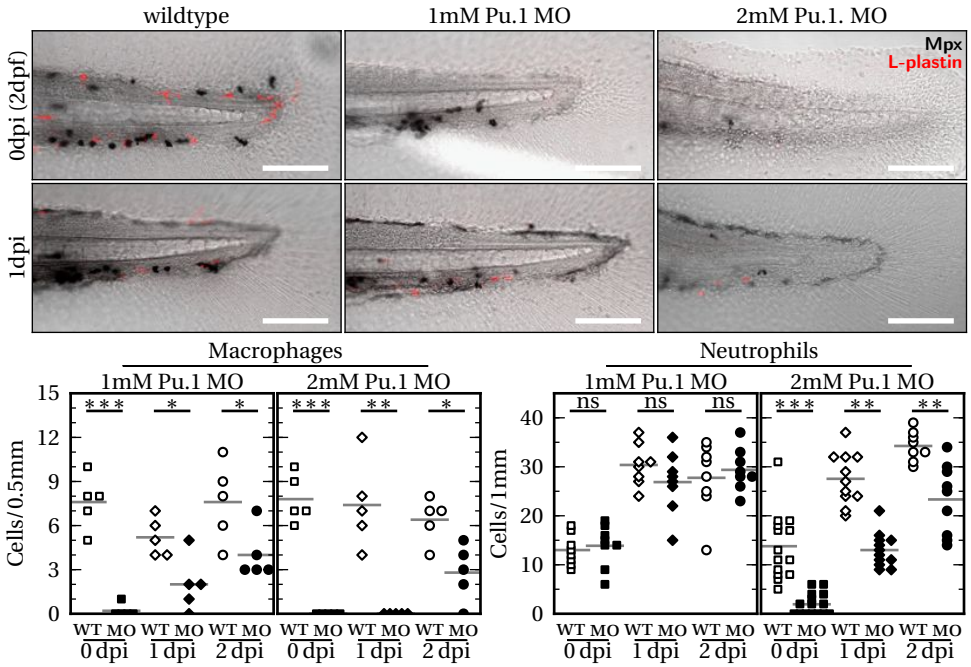

Figure 7.5:
Lineage-specific depletion of macrophages and neutrophils by dose-dependent morpholino-mediated knockdown of Pu.1. Neutrophils are shown in black (Mpx+ histochemical staining) and macrophages are shown in red (Mpx-/L-lpastin+). In each embryo, the macrophages in the region 0.5 mm from the posterior end of the tail fin and the neutrophils in the region 1 mm from the posterior end of the tail fin were quantified, which are sufficient to represent each linage distribution in the entire embryo.
Scale bars: 100 µm; ns = not significant ($p > 0.05$); * = $0.01 < p < 0.05$; ** = $0.0001 < p < 0.01$; *** = $p < 0.0001$.

down of Pu.1 (1 mM morpholino; fig. 7.5), while neutrophils were depleted by the complete knockdown of Pu.1 (2 mM morpholino; fig. 7.5). Using these different doses of Pu.1 morpholino, we found that the formation of tumor neovasculature, but not the physiological vasculature, was impaired under both partial and complete knockdown conditions of Pu.1 (fig. 7.6A, B), suggesting a major role of macrophages in the tumor vascularization. In contrast, tumor cell invasion at the posterior end of the CHT was only suppressed by complete knockdown of Pu.1, not by partial knockdown (fig. 7.6C,D), indicating that neutrophils play a predominant role in tumor cell invasion and micrometastasis. Taken together, myeloid cells are involved in the processes of both tumor vascularization and invasion, the critical steps towards localized tumor growth and micrometastasis.

A previous study of zebrafish myeloid cells sensing of HRASG12V-transformed

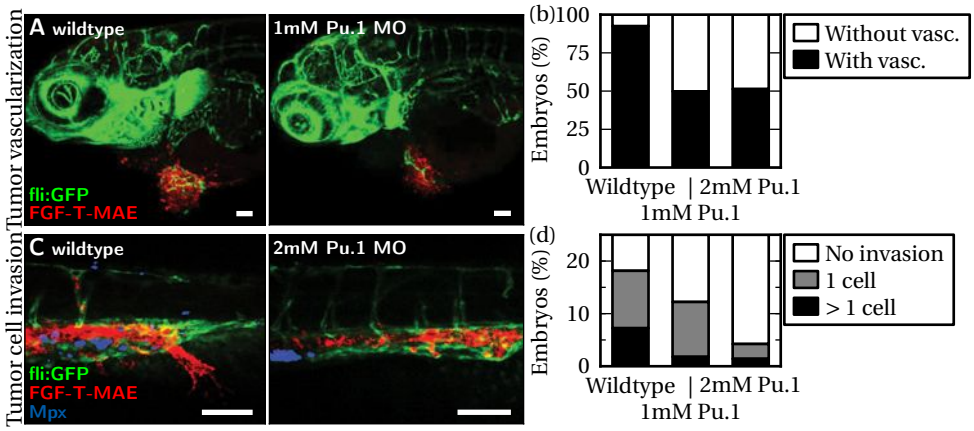

Figure 7.6:
(A,B) Suppression of FGF-T-MAE tumor vascularization under partial (1 mM) or complete (2 mM) knockdown of Pu.1 was significant (Wilcoxon test, $p < 0.01$). Representative embryos with tumor vascularization in the control and Pu.1 knockdown conditions at 3 dpi are shown in A and quantification of embryos with and without tumor vascularization at 1 dpi are shown in B.
(C,D) Suppression of FGF-T-MAE tumor cell invasion at the posterior end of the CHT under complete knockdown of Pu.1 was significant (Wilcoxon test, $p < 0.01$). Representative control and Pu.1 knockdown embryos at 1 dpi (C) and embryos scored for tumor cell invasion at 1 dpi (D). Scale bars are approximately 100 µm.

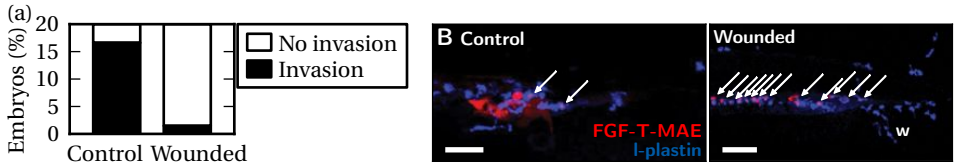

Figure 7.7:
(A) Suppression of tumor cell invasion by wound-inflammation in the tail fin at 1 dpi was significant (Wilcoxon test, $p < 0.001$). A wound in the tail fin was made mechanically (as in fig. 7.11) just after implantation of tumor cells at 2 dpf.
(B) Phagocytosis of tumor cells (indicated by arrows) around the invasion site by myeloid cells in embryos in which the tail fin was wounded (positioned by W). Tumor cells are shown in red and myeloid cells were stained for L-plastin (blue). Scale bars are approximately 200 µm.

cells suggested homologies between the myeloid cell responses towards transformed cells and wound-induced inflammation.[15] Therefore, we investigated the influence of wound-induced inflammation on tumor progression in our model. When the embryos were wounded at the tail-fin, we observed that tumor cell invasion was largely suppressed or abolished (fig. 7.7A). This suppression of tumor invasion was probably caused by inflammation-enhanced myeloid cell

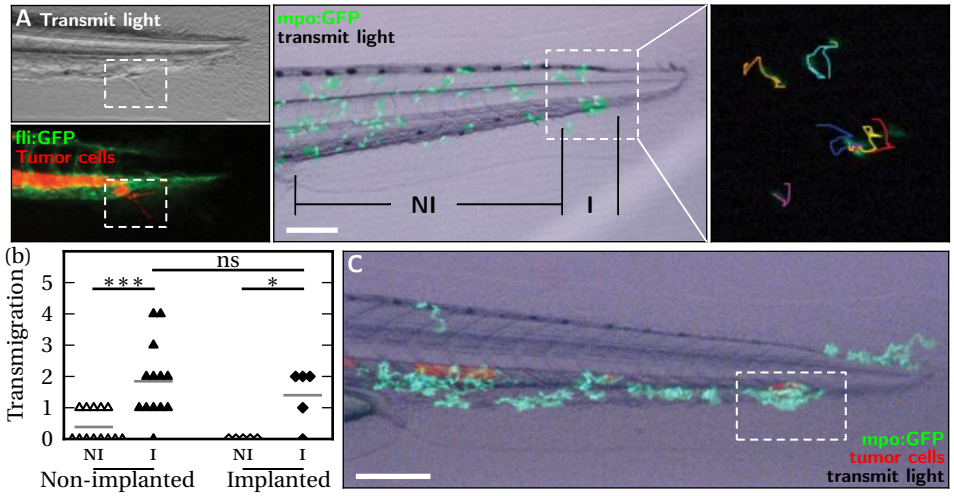

Figure 7.8:

(A) Migration tracks of GFP+ neutrophils in the tail of a Tg(mpx:GFP)^{i114} embryo (30 min time lapse with 1 min intervals). GFP+ neutrophils only transmigrated between the caudal hematopoietic tissue (CHT) and the tail fin (TF) at the site where tumor cells invaded into the tail fin. The CHT-TF transmigration area is indicated in the left panel which shows invasion of the tail fin by a dsRed-labeled FGF-T-MAE cell in a 3 dpf Tg(fli:GFP) embryo (top: bright field; bottom: fluorescence image). Manual tracking of 30 min migration patterns (right panel) of GFP+ neutrophils in the highlighted region of the tail of a 3 dpf Tg(mpx:GFP)^{i114} embryo (middle panel) showed that the transmigrating neutrophils (red, yellow and blue tracks) migrated as randomly as neighboring neutrophils in the tail (orange and light blue tracks) or already inside the fin tissue (purple track).

(B) Quantification of neutrophil transmigration (in 30 min) into the tail fin. Time lapse recordings were made of 3 dpf Tg(mpx:GFP)^{i114} embryos with or without implanted FGF-T-MAE tumor cells and the number of times that GFP+ neutrophils crossed the CHT-TF boundary was counted in two areas of the tail, the tumor invasion site (I) and the non-invasion site (NI) as indicated in A. The CHT-TF transmigration of neutrophils selectively occurred at the same site as tumor invasion. This spatial preference was not influenced by implantation.

(C) Two-hour recording of neutrophil (green) migration in Tg(mpx:GFP)^{i114} embryos after implantation of FGF-T-MAE tumor cells (red). The selective neutrophil CHT-TF transmigration site, overlapping with the tumor invasion site, is outlined.

ns = not significant ($p > 0.05$); * = $0.01 < p < 0.05$; ** = $0.0001 < p < 0.01$; *** = $p < 0.0001$.
Scale bars are approximately 200 µm.

phagocytosis, as the majority of implanted tumor cells were phagocytosed by L-plastin+ myeloid cells (fig. 7.7B). This result suggests that, in the absence of wounding, myeloid cells contribute to tumor vascularization and invasion in an inflammation-independent physiological manner.

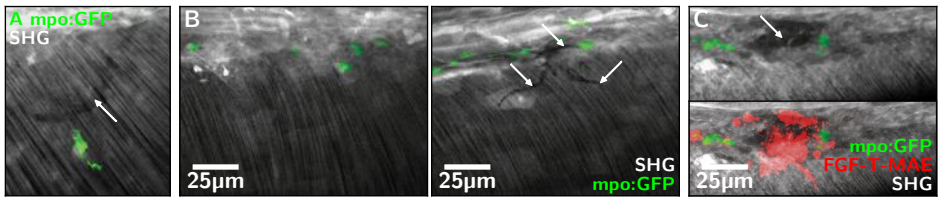

Figure 7.9:
Second harmonic generation (SHG) analysis of the fibrillar collagen matrix around the CHT-TF transmigration site. Images show an overlay of SHG signal (gray) with fluorescence of GFP+ neutrophils (TG(mpx:GFP)^{i114}) and red CM-DiL:-labelled FGF-T-MAE tumor cells.
(A) Example of a track (indicated by the arrow) of deformed collagen matrix in the tail fin created by a migrating neutrophil.
(B) Comparison of a region in the tail fin with no recent neutrophil migration events (left) and a region showing SHG-negative tracks (indicated with arrows) generated by migrating neutrophils (right).
(C) Invasion of tumor cells in an SHG-negative site in the tail fin. The image on the top shows the overlap of SHG and green fluorescence signal of neutrophils and the image on the bottom additionally shows the red fluorescence signal of tumor cells. The local loss of SHG signal is indicated with the arrow in the top image.

Physiological neutrophil migration conditions the collagen matrix for tumor cell invasion

To further investigate the involvement of neutrophils in tumor cell invasion, the physiological migration of neutrophils in 3 dpf embryos was analyzed using the TG(mpx:GFP)^{i114} neutrophil-specific zebrafish reporter line.[14] Time lapse and trajectories analysis showed that neutrophils randomly transmigrated between the caudal hematopoietic tissue and the tail fin (termed as "CHT-TF transmigration"), as a part of their physiological unrestricted random migration. This non-directional motion of neutrophils selectively occurred at the posterior end of the CHT where the perivascular tumor cells invaded into the tail fin (fig. 7.8A, B). The spatial preference for this location of CHT-TF transmigration was not altered by tumor cell implantation (fig. 7.8B,C) or by wound-induced inflammation (unpublished data and [24, 25]), suggesting that it is the normal physiological property of neutrophil migration in zebrafish embryos.

To further decipher the impact of neutrophil CHT-TF transmigration on the spatially co-localized tumor cell invasion process, two-photon excited confocal microscopy and second harmonic generation (SHG) was performed to visualize the extracellular fibrillar collagen matrix upon neutrophil migration.[26] Migrating neutrophils created transient tracks of deformed collagen matrix, as detected by the loss of SHG signal (fig. 7.9A), which was previously reported to be sufficient to support tumor cell invasion in mice models.[27] As a consequence of

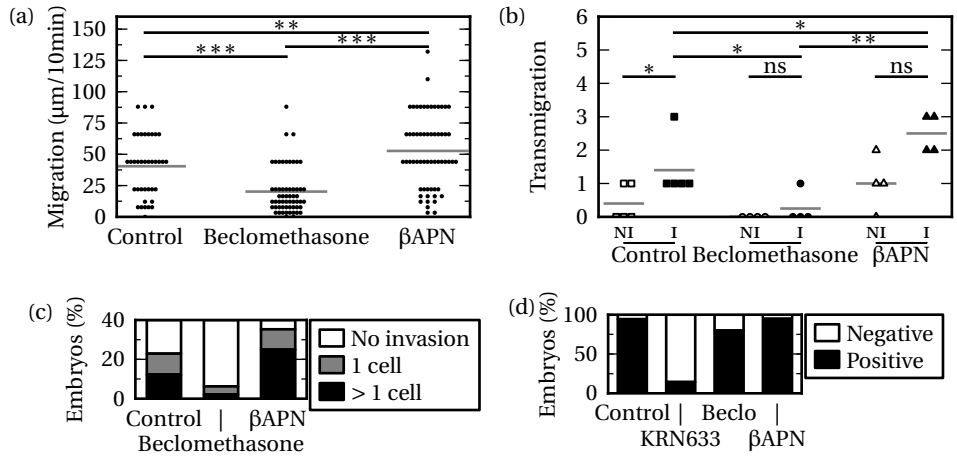

Figure 7.10:

(A) The random non-pathological migration of neutrophils was suppressed by beclomethasone (25µM) and promoted by βAPN (500µM). Migration tracks (µm) of neutrophils in 3dpf Tg(mpx:GFP)^{i114} embryos were recorded over 10min intervals.

(B) The CHT-TF transmigration of neutrophils (in 30min) was suppressed by beclomethasone and promoted by βAPN. Transmigration events in non-invasion (NI) and invasion (I) areas of the tail fin were quantified as in fig. 7.8B

(C) Tumor cell invasion at the posterior end of the CHT was significantly suppressed by beclomethasone (Wilcoxon test, $p < 0.01$) and promoted by βAPN($p < 0.01$). Embryos were scored for tumor cell invasion at 1dpi.

(D) Tumor vascularization was significantly suppressed by 0.1µM KRN633 (Wilcoxon test, $p < 0.01$), but not by 25µM beclomethasone or 500µM βAPN. Embryos were scored for vasculogenesis at 1dpi, as in fig. 7.6B.

ns = not significant ($p > 0.05$); * = $0.01 < p < 0.05$; ** = $0.0001 < p < 0.01$; *** = $p < 0.0001$.

the localized neutrophil CHT-TF transmigration, the deformation of the collagen matrix was largely enhanced at the posterior end of the CHT where the perivascular tumor cells invaded into the tail fin (fig. 7.9B). Furthermore, we observed that the tumor cells invaded into the tail fin at the exact site of local collagen deformation (fig. 7.9C). Thus, the observed tumor cell invasion was promoted by physiological neutrophil migration (the CHT-TF transmigration) which conditions the extracellular collagen matrix.

Pharmacological approaches were taken to confirm the functional involvement of neutrophil migration in tumor cell invasion. A prototype glucocorticoid receptor agonist beclomethasone, previously shown to inhibit neutrophil migration,[28] did not cause alteration of the fibrillar collagen matrix in zebrafish embryos (data not shown). We detected an inhibition of the normal physiological neutrophil migration and of neutrophil chemotaxis directed by wounding-induced inflammation[29] at 4 hours after administration of 25µM beclometha-

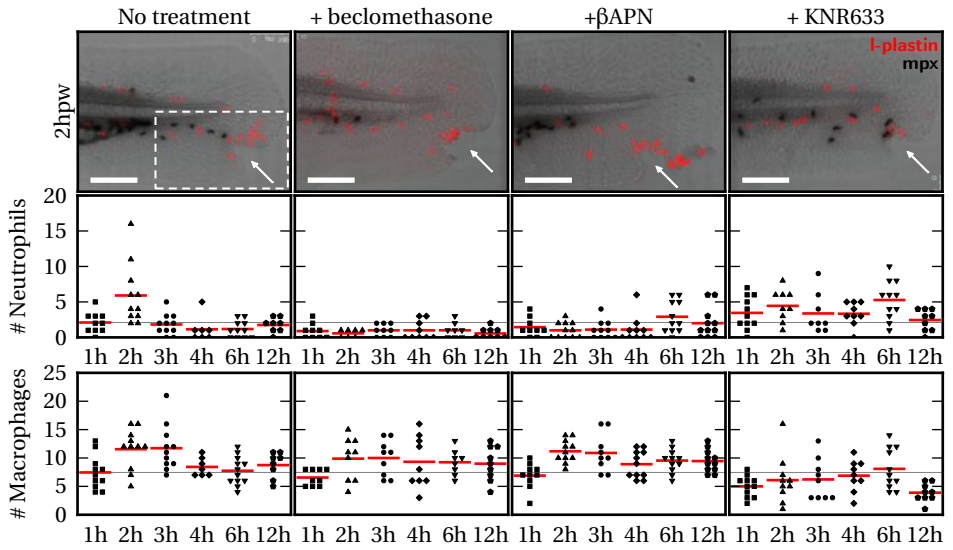

Figure 7.11:

Wounding-induced myeloid cell chemotaxis was affected by different pharmacological treatments. 3 dpf embryos were wounded on the tail fin as indicated by arrows in representative images of embryos from different treatment groups (no treatment; 25µM beclomethasone; 500µM βAPN; 1µM KRN633) at 2 hours post wounding (hpw). Embryos were fixed at different time point over a course of 12 hpw and stained for neutrophils (MPX+, histochemical staining) and macrophages (MPX-/L-lpastin+). Quantification of neutrophil and macrophage numbers was performed on $n \geq 8$ embryos per time point for each treatment group. The macrophages/neutrophils in the region outlined were quantified to measure the myeloid cell chemotaxis towards the wound.
Scale bars: 100µm

sone (fig. 7.10A,B and 7.11). Tumor cell invasion and micrometastasis was also reduced in embryos incubated in 25µM beclomethasone 4 hours before implantation (fig. 7.10C). In addition, we found that the lysyl oxidase inhibitor β-aminoproprionitrile (βAPN) largely reduced fibrillar collagen (unpublished data) and enhanced the CHT-TF transmigration of neutrophils, leading to a significant increase of tumor cell invasion and subsequent formation of micrometastases (figures 7.10A–C). Notably, βAPN inhibited neutrophil chemotaxis induced by inflammation (fig. 7.11), indicating that the increase of tumor cell invasion in βAPN-treated embryos was correlated with enhanced non-pathological neutrophil migration, but not with inflammation. Both beclomethasone and βAPN had no significant effect on macrophage chemotaxis (fig. 7.11) and tumor vascularization (fig. 7.10D). Taken together, these results reveal that only non-pathological neutrophil migration and the spatially restricted CHT-TF transmigration modify the extracellular matrix and have a major impact on tumor cell invasion and micrometastasis in this model.

7.4 Discussion

Using a novel zebrafish xenograft model that allows simultaneous single-cell resolution monitoring of multi-step tumorigenesis in vivo, including tumor vascularization, localized tumor growth, tumor invasion and micrometastasis formation, we discovered a new mechanism of the metastatic niche formation. In addition to the published roles of macrophages in this process,[2] we found that physiological migration of neutrophils controlled tumor invasion by conditioning the collagen matrix to facilitate the metastatic niche.

Recently the zebrafish myeloid cell population has been studied in detail and the similarities with the human myeloid cell functions and embryonic differentiation have been demonstrated.[30, 31] Further evidence that the zebrafish holds much potential for translational studies in cancer has been published.[32, 33] Recently it has been reported that expression of WHIM truncation mutations of CXCR4 in zebrafish neutrophils induces neutrophil retention in the caudal hematopoietic tissue, which represents a mechanism of human immunological WHIM disorder. WHIM zebrafish are neutropenic, and WHIM neutrophils show impaired recruitment to tissue inflammation sites, recapitulating the human disease. These findings support the potential of zebrafish to model primary immune disorders and underscore the translational relevance of zebrafish neutrophils transmigration in understanding of disease pathogenesis.[34, 35]

The involvement of myeloid cells in critical tumorigenesis steps such as vascularization and invasion was revealed by both genetic and pharmacological approaches. We demonstrated that myeloid cells, particularly the macrophages, are essential for tumor vascularization. Importantly, we also obtained evidence that the micrometastasis site was determined by the physiological migration of neutrophils. Our results show that yet undefined environmental cues favor neutrophil transmigration at the posterior end of the caudal hematopoietic tissue, which remodels the fibrillar collagen matrix, and in turn conditions the pre-metastatic niche for the tumor cells to invade into the tail fin. These findings support the “seed and soil” hypothesis that tumor metastasis is controlled by both the tumorigenic property of disseminated cells and their microenvironment.[36]

It is known that tumor-infiltrating immune cells can have both tumor-promoting and tumor-antagonizing roles.[37] In our model, the myeloid cells promote tumor progression under the physiological wound-free condition (fig. 7.6B,D), whereas immune-mediated destruction of tumor cells was hyper-activated by wound-induced inflammation (fig. 7.7). These results indicate that environmental factors have an impact on the balance between the conflicting immune cell responses to tumor cells. Interestingly, we found that the lysyl oxidase inhibitor

βAPN accelerates physiological neutrophil migration but decelerates pathological neutrophil chemotaxis, suggesting that different molecular mechanisms are involved in different modes of myeloid cell migration.

We propose that dual targeting of angiogenesis and myeloid cells can be beneficial in future treatments. Of course it will be only relevant for medical studies if the neutrophil transmigration is not restricted to this model. Currently the role of macrophages in intra- and extravasation of cancer cells is well established.[2] The role of neutrophils is less studied, however tumor associated neutrophils (TANS) were recently described and an increased level of neutrophils in cancer patients was shown to correlate with poor prognosis.[38] For example, a quantification of TANS in patients with renal cell carcinoma revealed that the presence of neutrophils correlated with increased mortality.[38] In addition, increased levels of TANS in the bronchioalveolar space of patients with bronchioalveolar carcinoma were significantly associated with poor outcomes.[39] In order to dissect the function of myeloid cells in human cancers live imaging of tumor-microenvironment interactions at the cellular level is required, a process severely limited in current mammalian models. This limitation strongly supports the relevance of the zebrafish model to unravel the molecular mechanisms of how tumor associated neutrophils mediate metastasis in zebrafish and mammalian models.

7.5 Materials and Methods

Zebrafish maintenance, morpholino injection and pharmacological treatment Zebrafish and embryos were raised, staged and maintained according to standard procedures in compliance with the local animal welfare regulations. The transgenic lines TG(FLI1:GFP) and TG(MPX:GFP)^{i114} were used in this study.[13, 14] 0.2mM N-phenylthiourea (PTU, Sigma) was applied to prevent pigment formation from 1 day post fertilization (dpf). For PU.1 knockdown as previously published, PU.1 MO (1MM for partial knockdown and 2MM for complete knockdown[22]) was injected into the yolk at the 1-cell stage as described.[40] For pharmacological inhibition, the VEGFR tyrosine kinase inhibitors KRN633 (0.1-1μM; Santa Cruz) or Sunitinib (0.1-1μM; Sigma), beclomethasone (25μM; Sigma), and β-aminopropionitrile (βAPN, 500μM; Sigma) were applied directly to the egg water and refreshed every two days.

Cell lines Murine aortic endothelial (MAE) cells and tumorigenic FGF2-overexpressing FGF2-T-MAE cells[21] (provided by M. Presta, University of Brescia, Italy), and the human breast carcinoma cell line MDA-MB-231[41] (provided by P. ten Dijke, Leiden University Medical Center, the Netherlands) were cultured as previously

described. 4T1 (CRL-2539, ATCC) and PC3 (CRL-1435, ATCC) cells were cultured in RPMI 1640 supplemented with 10% FBS (Invitrogen). Stable fluorescent cell lines were generated using lenti-viral vectors expressing dsRed or mCherry (provided by R. C. Hoeben, LUMC, the Netherlands). The virus-infected cells were used for experiments without FACS sorting and the fluorescence was stable in vitro for >10 passages. Zebrafish fibroblast cell lines ZF4 and PAC2 were cultured as previously described.[42]

Embryo preparation and tumor cell implantation Dechorionized 2 dpf zebrafish embryos were anesthetized with 0.003% tricaine (Sigma) and positioned on a 10 cm Petridish coated with 1% agarose. Mammalian cells were trypsinized into single cell suspensions, resuspended in PBS (Invitrogen), kept at room temperature before implantation and implanted within 3 hours. Non-fluorescent cells were labeled with the fluorescent cell tracker CM-DiL (Invitrogen) according to the manufacturer's instructions. The cell suspension was loaded into borosilicate glass capillary needles (1 mm O.D. × 0.78 mm I.D.; Harvard Apparatus) and the injections were performed using a Pneumatic Pico pump and a manipulator (WPI). 50~400 cells, manually counted, were injected at approximately 60 µm above the ventral end of the duct of Cuvier, where the duct of Cuvier opens into the heart. After implantation with mammalian cells, zebrafish embryos (including non-implanted controls) were maintained at 34 °C, to compromise between the optimal temperature requirements for fish and mammalian cells.[20] Up to 600 implantations were manually achieved per hour, with survival rates over 90% until 6 dpi. For pharmacological inhibition, beclomethasone was applied to the embryos 4 hours before implantation and KRN633, Sunitinib and βAPN were applied 4~6 hours post implantation. For each cell line or condition, data are representative of ≥3 independent experiments with ≥30 embryos per group. Experiments were discarded when the survival rate of the control group was less than 90%.

Microscopy and analysis For live imaging, embryos were anesthetized using 0.016% tricaine (Sigma) and mounted in 0.6% low melting agarose. Fixed embryos were imaged in PBST. Fluorescent image acquisition was performed using a Leica MZ16FA stereo microscope, a Leica TCS SPE confocal microscope or a Zeiss LSM exciter on an Axio Observer confocal microscope. Confocal stacks were processed for maximum intensity projections with Zeiss ZEN2009 software or ImageJ software. Images were adjusted for brightness and contrast using ImageJ. Overlays were created using Adobe Photoshop CS4 or ImageJ. 3D reconstruction and movies were assembled using ImageJ.

Multi-photon microscopy Second-harmonic generation (SHG) was used to image the helical structures of collagen fibers, which are capable of combining two photons into one.[26] The two-photon microscopy was performed on a Zeiss 710 NLO upright confocal microscope equipped with a Spectra-physics Deep See MP laser. The images were obtained with an excitation wavelength of 750 nm and only emitted light with a wavelength between 371 nm–467 nm was detected.

Myeloid cell detection In the Tg(fli1:GFP) line, the neutrophils in fixed embryos were detected using the Peroxidase/Myeloperoxidase Leukocyte Kit (Sigma) as described.[29] The embryos were imaged with transmitted light and the black stained cells were extracted using the Threshold function of ImageJ and subsequently converted into a selected color for overlay with fluorescence images. For macrophage detection, immunohistochemistry for L-plastin was performed after the myeloperoxidase activity assay and the MPX-/L-lpastin+ cells were counted as macrophages.[19] The Tg(mpx:GFP)^{i114} line was used to monitor neutrophil migration in vivo.[14] Time lapse imaging (1 minute intervals, ≥30 min) was performed using a Leica stereo fluorescence microscope. The migration tracks were generated by maximum intensity projections of the time stacks using ImageJ. For individual neutrophil tracking, the first 20 GFP+ cells from the posterior end of the tail fin in each embryo, which exhibited consistent intensity for at least 15 min, were tracked and analyzed using the Manual Tracking plugin of ImageJ.

Immunohistochemistry Whole-mount immunohistochemistry was carried out as described.[43] Primary antibodies and dilutions were used as follows: L-plastin (rabbit anti-zebrafish, 1:500; provided by A. Huttenlocher[19]), ZO-1 (mouse anti-human, 1:300; Invitrogen), phosphohistone H3 (rabbit anti-human, 1:500; Santa Cruz). 1:200 dilution of the secondary antibodies (Alexa 405 anti-mouse and Alexa 568 anti-mouse or Alexa 568 anti-rabbit; Invitrogen) was used for detection.

Tail fin wounding Zebrafish embryos at 2–3 dpf were anesthetized using 0.016% tricaine (Sigma) and then wounded on the ventral side of the tail fin with the tip of a glass capillary needle as described.[29] Wounded embryos were fixed in 4% paraformaldehyde/PBS at various time points after the wounding and stored in PBS, containing 0.01% Tween-20 (PBST) at 4 °C, for myeloid cell detection.

Microangiography Tetramethylrhodamine dextran was injected into the sinus venosus of anesthetized zebrafish embryos as described.[44] Images were acquired within ten minutes after injection.

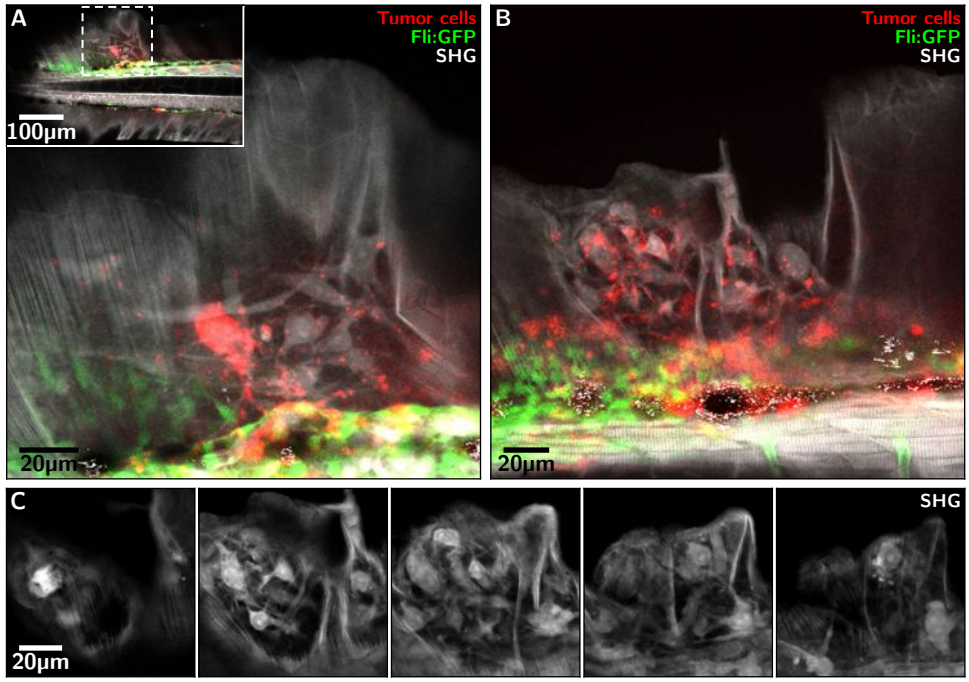

Figure 7.12:
SHG analysis of the collagen matrix around the micrometastis at 6 dpi.
(A,B) Tumor cells are labeled with the red cell tracker CM-DiL, resulting in a dotted fluorescent pattern in which proliferating cells have less signal. The vasculature is labeled green. The tumor cells seem to have pushed away the original collagen structure of the fin.
(C) Individual cross-sections from the tumor of (B), taken 7µm apart, show how the collagen structure encapsulates the tumor in all three dimensions.

Statistical analysis Statistical analysis was performed using the Prism 4 software (GraphPad), two- or one-tailed, unpaired t-tests with confidence intervals of 90% or 95%. ns = not significant ($p > 0.05$); * = $0.01 < p < 0.05$; ** = $0.0001 < p < 0.01$; *** = $p < 0.0001$.

7.6 Possibilities for new studies

The ability to non invasively image the collagen network of zebrafish, can be used to study many other processes. In this section we describe a few of the possibilities.

When tumor cells invade new tissue, the original ECM has to remodel to make space for the fast growing tumor. Figure 7.12 shows how the original collagen structure of the zebrafish fin seems to be pushed away by the new tumor tissue.

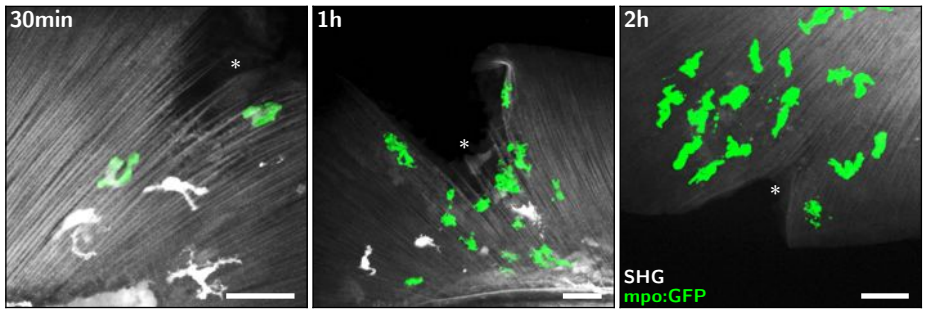

Figure 7.13:
Migrating mpo:GFP labeled neutrophils near a wound, marked by *, at 30 min, 1 h and 2 h post wounding. Already within 30 min after wounding, the first neutrophils arrive at the wounding site. Unlike the migrating neutrophils in the cancer model, fig. 7.9, these neutrophils do not seem to leave any tracks in the collagen matrix.

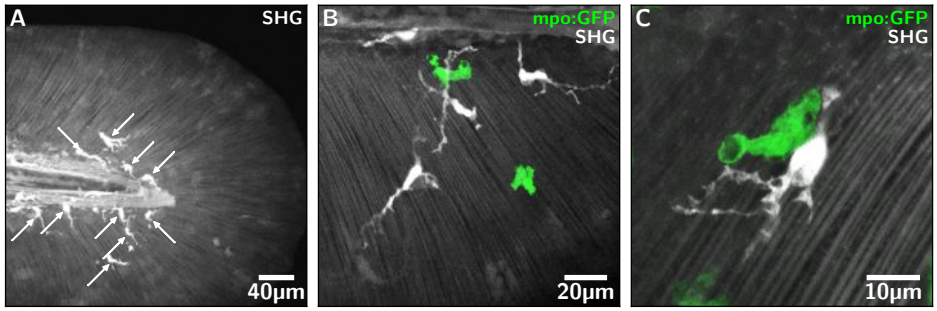

Figure 7.14:
Unknown cells, marked with arrows in (A), are visible in the second harmonic signal in the tail of zebrafish embryos. These cells seem to interact with the collagen fibers (B) and with neutrophils (C).

Figure 7.13 shows how the neutrophils indeed migrate towards the wound within 30 minutes after wounding. However, no obvious track of deformed collagen matrix was observed. It is possible that the neutrophil interact differently with collagen matrix during the pathological migration induced by wounding-induced inflammation, comparing to their physiological random migration (as shown in fig. 7.9). In addition, we noticed that the SHG signals around the wound are weaker than the non-wounded area, which makes it harder to detect deformed collagen tracks. The reduction of collagen SHG signal may be caused by the H_2O_2 production of the local tissue at the wound, which was recently discovered as the chemotractant for neutrophils to rapidly detect a wound in zebrafish.[45] We have noticed that the collagen SHG signal significantly decreased when the embryos were treated with 0.015% H_2O_2, supporting the hypothesis

that the H_2O_2 produced by wounded tissue weaken the collagen SHG signal (via an unknown mechanism).

In some of the multi-photon images, unknown cells are visible in the SHG signal, fig. 7.14. These cells seem to interact with the collagen matrix, fig. 7.14B, and possibly with neutrophils, fig. 7.14C. Immunological staining showed that these cells are neither macrophages nor fibroblasts. Further measurements are needed to understand what kind of cells these are, how they generate a second-harmonic signal and, more interestingly, what their interactions with the collagen matrix are.

7.7 Acknowledgements

We thank M. Presta and P. ten Dijke for providing cell lines; R.C. Hoeben for lenti-viral viruses; B. Weinstein and S. Renshaw for providing zebrafish lines; A. Huttenlocher for providing antibody; W. van der Ent, M.J. Rabelink and S. Rueb for assistance in cell culture and generation of stable fluorescent cell lines; A. van der Laan for support in multi-photon microscopy; D. de Witt and U. Nehrdich for zebrafish maintenance; M. Mione, P. ten Dijke and T.H. Oosterkamp for stimulating discussions; E.E. Patton for critical reading of the manuscript. This project was financially supported by the European Community under the FP7 ZF-Cancer project (HEALTH-F2-2008-201439).

7.8 References

[1] A. Patenaude, J. Parker, and A. Karsan. Involvement of endothelial progenitor cells in tumor vascularization. *Microvasc. Res.*, 79:217, 2010.

[2] J. A. Joyce and J. W. Pollard. Microenvironmental regulation of metastasis. *Nat. Rev. Cancer*, 9:239, 2009.

[3] L. M. Vecchiarelli-Federico, et al. Vascular Endothelial Growth Factor-A Positive and Negative Regulator of Tumor Growth. *Cancer Res.*, 70:863, 2010.

[4] C. Stockmann, et al. Deletion of vascular endothelial growth factor in myeloid cells accelerates tumorigenesis. *Nature*, 456:814, 2008.

[5] T. D. Tlsty and L. M. Coussens. Tumor stroma and regulation of cancer development. *Annu. Rev. Pathol.*, 1:119, 2006.

[6] M. Aghi and E. A. Chiocca. Contribution of bone marrow-derived cells to blood vessels in ischemic tissues and tumors. *Mol. Ther.*, 12:994, 2005.

[7] F. Shojaei and N. Ferrara. Refractoriness to antivascular endothelial growth factor treatment: role of myeloid cells. *Cancer Res.*, 68:5501, 2008.

[8] K. Stoletov and R. Klemke. Catch of the day: zebrafish as a human cancer model. *Oncogene*, 27:4509, 2008.

[9] G. J. Lieschke and N. S. Trede. Fish immunology. *Curr. Biol.*, 19:R678, 2009.

[10] W. Goessling, T. E. North, and L. I. Zon. New waves of discovery: modeling cancer in zebrafish. *J. Clin. Oncol.*, 25:2473, 2007.

[11] T. E. North, et al. Prostaglandin E2 regulates vertebrate haematopoietic stem cell homeostasis. *Nature*, 447:1007, 2007.

[12] L. I. Zon and R. T. Peterson. In vivo drug discovery in the zebrafish. *Nat. Rev. Drug Discov.*, 4:35, 2005.

[13] N. D. Lawson and B. M. Weinstein. In vivo imaging of embryonic vascular development using transgenic zebrafish. *Dev. Biol.*, 248:307, 2002.

[14] S. A. Renshaw, et al. A transgenic zebrafish model of neutrophilic inflammation. *Blood*, 108:3976, 2006.

[15] Y. Feng, et al. Live Imaging of Innate Immune Cell Sensing of Transformed Cells in Zebrafish Larvae: Parallels between Tumor Initiation and Wound Inflammation. *PLoS Biol.*, 8:e1000562, 2010.

[16] K. Stoletov, et al. High-resolution imaging of the dynamic tumor cell vascular interface in transparent zebrafish. *PNAS*, 104:17406, 2007.

[17] A. T. Chen and L. I. Zon. Zebrafish Blood Stem Cells. *J. Cell. Biochem.*, 108:35, 2009.

[18] F. Ellett and G. J. Lieschke. Zebrafish as a model for vertebrate hematopoiesis. *Curr. Opin. Pharmacol.*, 10:563, 2010.

[19] J. R. Mathias, et al. Live imaging of chronic inflammation caused by mutation of zebrafish Hai1. *J. Cell. Sci.*, 120:3372, 2007.

[20] M. Haldi, C. Ton, W. L. Seng, and P. McGrath. Human melanoma cells transplanted into zebrafish proliferate, migrate, produce melanin, form masses and stimulate angiogenesis in zebrafish. *Angiogenesis*, 9:139, 2006.

[21] S. Nicoli, D. Ribatti, F. Cotelli, and M. Presta. Mammalian tumor xenografts induce neovascularization in zebrafish embryos. *Cancer Res.*, 67:2927, 2007.

[22] J. Rhodes, et al. Interplay of pu.1 and gata1 determines myelo-erythroid progenitor cell fate in zebrafish. *Dev. Cell*, 8:97, 2005.

[23] F. Su, et al. Differential regulation of primitive myelopoiesis in the zebrafish by Spi-1/Pu.1 and C/ebp1. *Zebrafish*, 4:187, 2007.

[24] F. Ellett, et al. mpeg1 promoter transgenes direct macrophage-lineage expression in zebrafish. *Blood*, 117:e49, 2011.

[25] C. Gray, et al. Simultaneous intravital imaging of macrophage and neutrophil behaviour during inflammation using a novel transgenic zebrafish. *Thromb. Haemost.*, 105:811, 2011.

[26] A. Zoumi, A. Yeh, and B. J. Tromberg. Imaging cells and extracellular matrix in vivo by using second-harmonic generation and two-photon excited fluorescence. *PNAS*, 99:11014, 2002.

[27] C. Gaggioli, et al. Fibroblast-led collective invasion of carcinoma cells with differing roles for RhoGTPases in leading and following cells. *Nat. Cell Biol.*, 9:1392, 2007.

[28] L. K. Mathew, et al. Unraveling tissue regeneration pathways using chemical genetics. *J. Biol. Chem.*, 282:35202, 2007.

[29] J. R. Mathias, et al. Resolution of inflammation by retrograde chemotaxis of neutrophils in transgenic zebrafish. *J. Leukoc. Biol.*, 80:1281, 2006.

[30] K. Kissa and P. Herbomel. Blood stem cells emerge from aortic endothelium by a novel type of cell transition. *Nature*, 464:112, 2010.

[31] J. Y. Bertrand, et al. Haematopoietic stem cells derive directly from aortic endothelium during development. *Nature*, 464:108, 2010.

[32] R. M. White, et al. DHODH modulates transcriptional elongation in the neural crest and melanoma. *Nature*, 471:518, 2011.

[33] C. J. Ceol, et al. The histone methyltransferase SETDB1 is recurrently amplified in melanoma and accelerates its onset. *Nature*, 471:513, 2011.

[34] K. B. Walters, et al. Live imaging of neutrophil motility in a zebrafish model of WHIM syndrome. *Blood*, 116:2803, 2010.

[35] Q. Deng, et al. Dual roles for Rac2 in neutrophil motility and active retention in zebrafish hematopoietic tissue. *Dev. Cell*, 21:735, 2011.

[36] I. J. Fidler. The pathogenesis of cancer metastasis: the 'seed and soil' hypothesis revisited. *Nat. Rev. Cancer*, 3:453, 2003.

[37] D. Hanahan and R. A. Weinberg. Hallmarks of cancer: the next generation. *Cell*, 144:646, 2011.

[38] H. K. Jensen, et al. Presence of intratumoral neutrophils is an independent prognostic factor in localized renal cell carcinoma. *J. Clin. Oncol.*, 27:4709, 2009.

[39] M. Wislez, et al. Hepatocyte growth factor production by neutrophils infiltrating bronchioloalveolar subtype pulmonary adenocarcinoma: role in tumor progression and death. *Cancer Res.*, 63:1405, 2003.

[40] S. F. G. Krens, et al. Distinct functions for ERK1 and ERK2 in cell migration processes during zebrafish gastrulation. *Dev. Biol.*, 319:370, 2008.

[41] M. Deckers, et al. The tumor suppressor Smad4 is required for transforming growth factor beta-induced epithelial to mesenchymal transition and bone metastasis of breast cancer cells. *Cancer Res.*, 66:2202, 2006.

[42] S. He, et al. Genetic and transcriptome characterization of model zebrafish cell lines. *Zebrafish*, 3:441, 2006.

[43] S. He, et al. A ΔRaf1-ER-inducible oncogenic zebrafish liver cell model identifies hepatocellular carcinoma signatures. *J. Pathol.*, 225:19, 2011.

[44] M. Montero-Balaguer, et al. Stable Vascular Connections and Remodeling Require Full Expression of VE-Cadherin in Zebrafish Embryos. *PLoS ONE*, 4:e5772, 2009.

[45] P. Niethammer, C. Grabher, A. T. Look, and T. J. Mitchison. A tissue-scale gradient of hydrogen peroxide mediates rapid wound detection in zebrafish. *Nature*, 459:996, 2009.

8 Epilogue

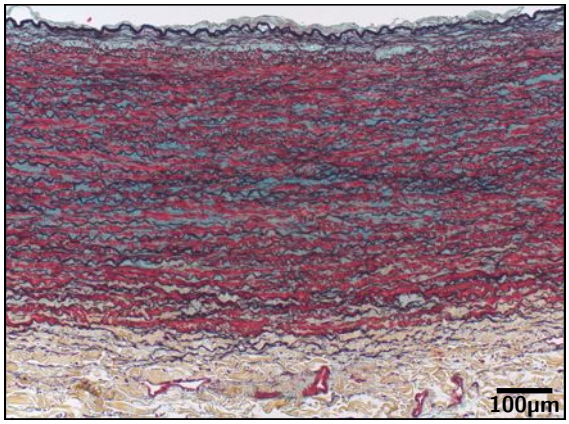

Figure 8.1: Movat stained coupe of the arterial wall.

In this thesis we have shown how the atomic force microscope, in combination with various other techniques, can be used to study the physics of the collagen network of several tissues: the aortic wall, the fibrous cap of atherosclerotic plaques in humans and the tail of zebrafish; We have also studied how the aortic tissue responds to various digestions. These studies have gained us new insights in the mechanical properties of the ECM of these tissues and how they are impaired in various pathologies.

Our experiments on aneurysms showed how the failure of the vessel wall is caused by the disruption of the spatial organization of the collagen fibers, rather than by a lower concentration of collagen.

In atherosclerosis a complex interplay between different ECM degrading enzymes on the one hand and ECM stabilizing proteins like LOX on the other, determine the mechanical stability of the fibrous cap. The AFM proved to be a valuable tool to measure local stiffness variations. This can give new clues on cap weakening by linking local stiffness variations to various inflammatory markers or ECM stabilizing proteins.

The examination of tumor development in zebrafish showed how cells from the immune system remodeled the collagen matrix, enabling the tumor cells to invade new tissue. This study revealed a new type of cell/ECM interaction in tumors which could also play a role in human cancer development

Finally we have shown how the arterial wall can be used as model system to study the effects of various proteolytic enzymes on the ECM. The measurements with the neutrophil extract showed, for example, how enzymes, produced by neutrophils, alter the tissue in such a way that it gives the same response upon indentation as aneurysmatic tissue.

This new way of studying diseases of the ECM could result in new insights in many other pathologies as well. Here we discuss possible future experiments on myocardial infarction and cervix ripening.

After a myocardial infarction the ECM of the heart has been locally disrupted. The newly formed collagen network, which has much resemblance with ordinary scar tissue, has different mechanical properties from the surrounding muscle tissue. The AFM could probe these differences, which will help to understand how the functioning of the heart is hindered by this stiffer scar tissue.

During pregnancy and delivery, the collagen network of the cervix, the lower part of the uterus, changes in such a way that the initial stiff tissue becomes soft, making it possible for the infant to be delivered. During cervix ripening, neutrophils are known to be active in the cervix, but the precise mechanism which softens the tissue is unknown. It has long been assumed that matrix metalloproteases play a major role in cervix ripening. Recent studies, however, have show that this assumption is not valid.[1] Moreover, the alteration of the ECM of the cervix is particularly interesting because of its reversibility: the ECM of the cervix is repaired within a few weeks after delivery. A combined AFM and histological study of the cervix at different stages during ripening, could link specific changes in ECM organization to the stiffness of the tissue. The AFM could furthermore be used to measure the effect of the individual proteolytic enzymes, present during cervix ripening, on the effective Young's modulus of the tissue.

Most of the biophysical research on collagen has largely focused on networks of purified collagen I, the most abundant type of collagen. In vivo, however, collagen I usually forms heterotypic fibrils together with other collagen types. The ratio between collagen V and I is known to change during tissue development and is different for various diseases, like atherosclerotic plaques and scar tissue. Piechocka et al. showed, using micro-rheology experiments, how collagen gels get softer when the ratio of collagen V to collagen I is increased.[2] It is still unknown, however, whether this effect is caused by a change in stiffness of the individual collagen fibrils or whether it is the result of a change in the connections between the fibrils. An AFM study, similar to the one we have performed on the aneurysmatic tissue, in which indenters of different sizes were used, could be used to discriminate on which length scale the network changes.

During the studies performed for this thesis, contacts have been made with a number of medical groups of different disciplines, which broadened the horizon

[1] R. A. Word, X. H. Li, M. Hnat and K. Carrick. Dynamics of cervical remodeling during pregnancy and parturition: mechanisms and current concepts. *Semin. Reprod. Med.*, 25:69, 2007

[2] I. K. Piechocka, A. S. G. van Oosten, R. G. M. Breuls, and G. H. Koenderink. Rheology of heterotypic collagen networks. *Biomacromolecules*, 12:2797, 2011

of all groups involved. The work described in this thesis fits into the growing sense among medical researchers to appreciate the ECM not only as the environment of cells, but also as an important part of tissues with its own dynamics. There is a growing awareness that for understanding the functioning of an organ the organization and characteristics of the surroundings of the cells is equally important as the cells themselves. For the physicists, these studies have been one of the first crossings of the gap between a well controlled in vitro experiment or a theoretical study to an in vivo system that involves many more components and uncertainties.

I hope that this study has contributed to the development of a new branch of multidisciplinary research, which, in the near future, will unveil exciting new physics as well as new clinically relevant insights.

Samenvatting

Het menselijk lichaam is opgebouwd uit verschillende typen weefsel, zoals bind-, zenuw- en spierweefsel. In zo'n weefsel zitten cellen met een vergelijkbare functie, die door intercellulaire contacten en een extracellulaire matrix verbonden zijn. Deze extracellulaire matrix bestaat uit verschillende soorten fibers die samen een netwerk vormen. Dit netwerk is niet alleen van belang omdat het de omgeving is waarin de cellen zich bevinden, maar ook omdat het voor een groot deel de structuur en integriteit van het weefsel bepaalt. In dit proefschrift heb ik met een aantal technieken naar de extracellulaire matrix van bloedvaten gekeken om te onderzoeken hoe dit de mechanische eigenschappen van de vaatwand bepaalt en om te zien hoe dit bij verschillende ziektebeelden verstoord is.

In dit onderzoek hebben we onze aandacht vooral gericht op de aorta, ook wel bekend als de grote lichaamsslagader. Deze slagader loopt vanaf het hart door de buik naar beneden en brengt zuurstofrijk bloed naar het grootste deel van het lichaam. De aorta heeft bij een volwassen mens een diameter van twee à drie centimeter en in rust stroomt er gemiddeld vijf liter bloed per minuut doorheen.

De aortawand is opgebouwd uit drie verschillende lagen. De binnenste laag, de intima, bestaat uit een laag endotheel-cellen die in direct contact met het bloed staan. De middelste laag, de media, is opgebouwd uit een netwerk van elastine-fibers. Deze fibers zijn zeer elastisch en kunnen tot wel 150% opgerekt worden zonder te breken. In deze laag zitten ook gladde spiercellen die het weefsel in de goede vorm houden en de extracellulaire matrix produceren. De buitenste laag van de aorta, de adventitia, bestaat uit een losmazig netwerk van collageen-fibers, die in tegenstelling tot elastine zeer stug zijn.

De buitenste twee lagen van de aortawand zorgen voor de bijzondere mechanische eigenschappen van de aorta. Bij kleine vervormingen is het bloedvat flexibel doordat de collageen-fibers dan nog niet op spanning staan en de elastine-fibers meerekken en zorgen dat het bloedvat de goede vorm behoudt. Deze flexibiliteit is cruciaal voor de aorta omdat bij elke hartslag de druk tijdelijk stijgt en het bloedvat dit kan opvangen door een beetje uit te zetten. Bij te grote vervormingen echter, komen de collageen-fibers in de buitenste laag strak te staan, waardoor het bloedvat niet verder kan rekken en scheuren. Dit is te vergelijken met een autoband die opgebouwd is uit het elastische rubber en een metalen karkas. Door het rubber kan de band gemakkelijk kleine oneffenheden in de weg

opvangen, maar het karkas voorkomt dat de band scheurt wanneer er te hard tegen een stoeprand gereden wordt.

Om de mechanische werking van de extracellulaire matrix van de aorta te doorgronden, gebruiken we voornamelijk twee technieken. Door het weefsel onder een optische microscoop te leggen, zien we hoe de verschillende soorten fibers in het weefsel geweven zijn tot een netwerk. Hiervoor maken we enerzijds gebruik van de optische eigenschappen van de fibers; elastine licht bijvoorbeeld op als het met groen licht beschenen wordt. Anderzijds gebruiken we speciale labels om de fibers te kunnen onderscheiden, bijvoorbeeld een antilichaam dat aan een specifiek type collageen plakt en dat onder rood licht zichtbaar wordt. In het bijzonder hebben we veel gebruik gemaakt van een confocale microscoop. Deze microscoop maakt het mogelijk om een drie-dimensionale weergave van het weefsel te maken, waardoor we precies zien hoe de verschillende fibers door elkaar heen geweven zijn. Daarnaast hebben we de optische microscoop ook gebruikt om andere onderdelen van de vaatwand, bijvoorbeeld cellen van het immuunsysteem, te volgen en te kijken hoe zij de extracellulaire matrix beïnvloeden.

De andere techniek die we in dit onderzoek veelvuldig gebruikt hebben, is de atomaire kracht microscoop (AFM). De kern van dit apparaat is een klein hefboompje, zo'n 40µm breed (de dikte van een haar) en 1µm dik, met aan het einde een minuscuul scherp puntje. Met deze hefboom kunnen we op individuele fibers van het weefsel drukken om zo te meten hoe stijf zo'n fiber is of hoeveel kracht het netwerk kan hebben voordat het scheurt. Door deze informatie te combineren met de gegevens over de opbouw van het weefsel, proberen we te begrijpen wat de mechanische eigenschappen van de aorta zijn, hoe deze tot stand komen en hoe deze eigenschappen bij sommige ziektebeelden aangetast zijn.

Het eerste ziektebeeld waarbij wij dit gedaan hebben, is een aneurysma van de abdominale aorta. Bij deze aandoening zwelt het onderste deel van de aorta lokaal op tot een ballon totdat hij, indien hij niet geopereerd wordt, uiteindelijk scheurt met de dood als gevolg. Hoewel het een relatief veel voorkomende ziekte is, ongeveer 1 op de 20 personen boven de 60 heeft een aneurysma, en er al tientallen jaren onderzoek naar gedaan wordt, was het tot een paar jaar geleden nog onduidelijk wat de oorzaak van deze lokale verzwakking is. Zo bleek de hoeveelheid collageen-fibers en het aantal verbindingen tussen deze fibers niet noemenswaardig te verschillen tussen een gezonde en een aneurysmatische aorta. Onze drie-dimensionale weergave van de collageen-fibers in het gezonde weefsel, laat zien hoe de individuele fibers samen dikke collageen-bundels vormen en dat deze bundels samen een hecht netwerk vormen. Bij het aneurysmatische weefsel

echter, blijkt alle organisatie verloren te zijn en zien we een ongestructureerde aggregatie van collageen-fibers. Wanneer we de gezonde weefsels met de AFM indrukken, blijken de fibers in het gezonde weefsel op zo'n manier met elkaar verbonden te zijn, dat ze samen de kracht verdelen waardoor het weefsel intact blijft. Bij het aneurysma is het netwerk van een dusdanig slechte kwaliteit, dat de fibers alle deformatie zelfstandig moeten dragen, waardoor ze breken en het netwerk beschadigd raakt. Deze studie laat hiermee het belang van de netwerkstructuur van de collageen-fibers in de vaatwand zien en toont hoe een verlies in de organisatie van dit netwerk het opzwellen en uiteindelijk scheuren van de aorta tot gevolg kan hebben.

In een vervolgonderzoek hebben we met dezelfde technieken gekeken welke bijdrage de afzonderlijke componenten van de vaatwand leveren aan de mechanische eigenschappen van het geheel. Dit deden we door afzonderlijke bouwstenen met enzymen af te breken. Zo zagen we bijvoorbeeld dat er na het afbreken van al het collageen in de adventitia, de buitenste laag van de aorta, nog steeds een coherent netwerk overblijft, dat ongeveer 50 maal minder stijf is dan het intacte weefsel. Eén van de opmerkelijke resultaten van dit onderzoek is het effect van een neutrofiel extract op het weefsel. Neutrofielen zijn immuuncellen en van dit type cellen is het bekend dat ze in verhoogde aantallen in aneurysma's aanwezig zijn. AFM-metingen op de adventitia lieten zien dat het neutrofiel extract de mechanische eigenschappen van het weefsel binnen 24 uur zodanig verandert dat het grote overeenkomsten vertoont met het aneurysmatische weefsel. Verder onderzoek moet uitwijzen welke specifieke elementen uit het extract hiervoor verantwoordelijk zijn en of dit mogelijkheden voor de behandeling van aneurysma's biedt.

Na de succesvolle metingen op aneurysma's, hebben we deze manier van het bestuderen van weefsels op andere ziektebeelden toegepast. Atherosclerose, ook wel aderverkalking genoemd, is een langzaam voortschrijdende ziekte, die begint met het ophopen van vetten in de vaatwand. Bij de ontsteking die dit tot gevolg heeft, komen veel afbraakstoffen vrij. Om te voorkomen dat deze stoffen in de bloedbaan komen, worden ze afgedekt door een laag collageen. Tijdens de progressie van de ziekte, kan deze laag echter verzwakt raken en uiteindelijk zelfs scheuren. Als de afbraakstoffen vervolgens in de bloedbaan komen, starten zij een stollingsreactie die leidt tot een bloedstolsel. Dit stolsel kan tenslotte de bloedtoevoer tot bijvoorbeeld het hart of de hersenen blokkeren en daardoor een hartinfarct of een beroerte veroorzaken. Recente studies bij muizen hebben aangetoond dat lysyl-oxidase, een eiwit dat bijdraagt aan de verbindingen tussen collageen-fibers (LOX), het collageen-omhulsel van atherosclerotische plaques verstevigt. Wij zijn op deze studie verder gegaan door ten eerste te laten zien dat plaques met meer LOX stabieler zijn dan plaques met minder LOX. Dat deden we

opnieuw door zowel met een optische microscoop te kijken, door bijvoorbeeld de hoeveelheid collageen met de hoeveelheid LOX te vergelijken, alsook door met behulp van de AFM aan te tonen dat binnenin een plaque plekken met meer LOX steviger zijn dan plekken met minder LOX. Vervolgens lieten we zien hoe de hoeveelheid LOX negatief correleert met verschillende tekenen die een verslechterd ziektebeeld geven, zoals bijvoorbeeld de maat waarin het weefsel ontstoken is. Tenslotte toonden we aan dat patiënten die meer LOX produceren minder atherosclerotische complicaties, zoals een hartinfarct, hebben dan patiënten die minder LOX produceren.

In de voorgaande ziektebeelden spelen steeds de interactie tussen immuuncellen en de extracellulaire matrix een belangrijke rol bij de progressie van de ziekte. Door middel van een nieuw diermodel, waarbij menselijke tumorcellen in zebravis embryo's geïnjecteerd worden, hebben we bestudeerd hoe tumorcellen de extracellulaire matrix van tot dan toe nog gezond weefsel binnendringen. Met verschillende optische technieken toonden we aan hoe de neutrofielen, dezelfde immuuncellen die ook bij aneurysma's aanwezig zijn, het collageennetwerk van de zebravis veranderen en dat dit het voor de tumorcellen mogelijk maakt om het nieuwe weefsel binnen te dringen. Wanneer de neutrofielen door medicijnen geïnactiveerd werden, zagen we geen tumorcellen het weefsel binnendringen. Hoewel de resultaten van dit onderzoek nog zeer pril zijn, openbaren ze tot nu toe onbekende processen, die mogelijk ook bij tumorprogressie bij mensen een belangrijke rol spelen.

Met dit onderzoek hebben we laten zien welke belangrijke rol de extracellulaire matrix voor de de integriteit van het weefsel heeft, en hoe deze bij verschillende ziektebeelden aangetast is. Hiermee is een heel nieuwe manier om ziektes en processen binnen het menselijk lichaam te bestuderen geopend. Een voorbeeld van een mogelijke vervolgstudie is de verweking, ofwel het zachter worden, van de cervix (baarmoederhals) rond de bevalling. Het cervixweefsel bestaat voornamelijk uit collageen, maar de manier waarop dit initieel stijve weefsel verandert in zacht weefsel, zodat de baby geboren kan worden, is nog onbekend. Dit proces is des te meer interessant, omdat het reversibel is: het collageennetwerk is binnen enkele weken na de bevalling weer in haar oorspronkelijke staat terug.

Summary

The human body contains various types of tissues, such as connective, nervous and muscle tissue. Each type of tissue consists of an ensemble of cells that, together, carry out a specific function. These cells are connected by intercellular contacts and through the extracellular matrix (ECM), which is constructed of different types of fibers that form a network. This network is not only valuable because it defines the surrounding of the cells, but also because it defines to a great extent the structure and integrity of the tissue as a whole. In this thesis I have employed a variety of techniques to look at the extracellular matrix of blood vessels, to find out how it defines the mechanical properties of the vascular wall, and to see how this is disrupted in a number of pathologies.

In this study I have mainly focused my attention on the aorta. This artery originates at the heart and extends down through the belly, and brings oxygen rich blood to a large portion of the body. The aorta of an adult human has a diameter of two to three centimeters and, at rest, has a blood flow of about five liters per minute.

The aortic wall is composed of three different layers. The inner layer, the intima, consists of a layer of endothelial cells which are in direct contact with the blood. The middle layer, the media, is constructed of a network of elastin fibers. These fibers are very elastic and can be stretched up to 150% without breaking. In this layer, smooth muscle cells are also present. They keep the tissue in the correct shape and produce the components of the extracellular matrix. The outer layer of the aorta, the adventitia, is composed of a loose network of collagen fibers, which, in contrast to the elastin fibers, are very stiff.

The outer two layers of the aortic wall give rise to its remarkable mechanical properties. The blood vessel is flexible at small deformations because the collagen fibers are not yet strained. The elastin fibers, however, will stretch a bit and ensure that the vessel maintains its shape. This flexibility is of great importance for the aorta because by expanding slightly it can respond to the temporal rise in blood pressure at every heart beat. At large deformations, however, the collagen fibers in the outer layer are put under tension, preventing the blood vessel to stretch too much and rupture. A similar principle is applied to the construction of a car tire, which is composed of elastic rubber and a metal framework. The rubber allows the tire to adsorb small bumps in the road, but the metal framework

prevents the tire from rupturing when it hits the kerb.

To comprehend the mechanical functioning of the extracellular matrix of the aorta, we mainly use two, complementary, techniques. By examining the tissue with an optical microscope, we can see how the different types of fibers are woven into a network. To this end we use the optical properties of the fibers themselves. Elastin, for example, lights up when it is illuminated with green light. We also use special labels to distinguish different types of fibers, for example an antibody that sticks to a specific type of collagen and which becomes visible in red light. In this study we have made much use of confocal microscopy. This type of microscopy allows for the generation of a three-dimensional representation of the tissue, making it possible to precisely determine how the different types of fibers are interwoven. In addition, we have used the optical microscope to image other components of the vascular wall, for example cells of the immune system, in order to see how they influence the extracellular matrix.

The other technique which we have used in this study is the atomic force microscope (AFM). The central element of this instrument is a small cantilever, about 40µm wide (the thickness of a hair) and 1µm thick, with at the end a sharp tip. With this cantilever we push on the individual fibers of the tissue to measure their stiffness and to determine how much force the network can carry before it breaks. By combining these measurements with information about the construction of the network, we try to come to a rational explanation for the mechanical properties of the aorta and to see how these properties have been affected in certain pathologies.

The first pathology for which we have used this approach, is an aneurysm of the abdominal aorta. In this disease, the lower part of the aorta locally swells up like a balloon, until it ruptures, which is almost always lethal. Despite the fact that this is a relatively common pathology — about 1 out of 20 adults above 60 years old have an aneurysm — and decades of research have been spent on this specific disease, the cause of this local weakening of the vessel wall was not known until a few years ago. There is, for example, no remarkable difference in the number of collagen fibers and the connections between these fibers between a healthy and an aneurysmatic aorta. Our three-dimensional representation of the collagen fibers in the healthy tissue showed how the individual collagen fibers together form thick bundles and that those bundles together form a dense network. For the aneurysmatic tissue, however, this arrangement appears to be completely lost and we only observed an unstructured aggregation of collagen fibers. When we indented the healthy tissue with the AFM, all the individual fibers in the tissue appeared to be connected in such a way that they shared the load, keeping the tissue intact. The network of the aneurysmatic tissue

was of such poor quality that all the fibers had to bear the load independently, causing the fibers to break, thereby damaging the network. This study shows the importance of the network structure of the collagen fibers in the vascular wall and demonstrates how a loss in the organization of the network can result in the local swelling and even rupturing of the aorta.

In a follow-up study, we used the same approach to examine the contribution of the individual components of the vascular wall to the mechanical properties of the whole tissue. This was done by selectively removing the individual building blocks of the tissue using enzymes and subsequently using optical imaging and AFM measurements to observe the effect of the treatment. This showed, for example, how after removing collagen from the adventitia, a coherent network remained, which was about 50 times less stiff than the original tissue. One of the remarkable results of our study was the effect of a neutrophil extract on the tissue. Neutrophils are cells of the immune system and it is known that this type of cells is present in elevated numbers in aneurysms. AFM measurements on the adventitita showed how the neutrophil extract changed, within 24 hours, the mechanical properties of the adventitia in such a way, that it showed large similarities with the aneurysmatic tissue. Further research has to clarify which specific elements of this extract cause this change and whether this carries a promise for the treatment of aneurysms.

After the successful measurements on aneurysms, we have extended the same approach of studying tissues towards other pathologies. Atherosclerosis is a slowly progressing disease, which starts with the accumulation of lipids in the vessel wall. The resulting inflammatory reaction produces a plethora of breakdown products of cells and the extracellular matrix. These products are covered by a layer of collagen to prevent them from entering the bloodstream. During the progression of the disease, however, this collagen layer becomes weaker and can eventually rupture. The breakdown products will then enter the blood, which will start clotting. This blood clot can ultimately block the blood supply to the heart or brain and cause a myocardial infarction or stroke. Recent studies in mouse models showed that lysyl oxidase, a protein which facilitates the connection between collagen fibers (LOX), reinforces the collagen cap of atherosclerotic plaques. We continued this study by first showing that human plaques with more LOX are more stable than plaques with less LOX. We did this both optically, for example by comparing the amount of collagen with the local LOX concentration, as well as with the AFM by showing that plaque regions with more LOX tend to be stiffer as compared to regions with less LOX. Subsequently, we showed that the amount of LOX is inversely correlated with adverse clinical symptoms, like, for example, the level of inflammation within the tissue. Lastly, we showed that patients who produce more LOX suffer less from atherosclerotic complications,

like a myocardial infarction, compared to patients who produce less LOX.

In the pathologies discussed above, the interactions between immune cells and the extracellular matrix play an important role in the progression of the disease. By means of a new animal model, in which human tumor cells are injected into zebrafish embryos, we studied how tumor cells infiltrate the extracellular matrix of, until then, healthy tissue. Using various optical techniques, we showed how neutrophils, the same immune cells which are present in aneurysms, alter the collagen network of the zebrafish and that this enables the tumor cells to invade new tissue. When we inactivated the neutrophils using various drugs, the tumor cells were no longer able to infiltrate the tissue. Although the results of this study are very fresh, they reveal hitherto unknown processes, that could possibly also play an important role in human tumor progression.

With this research we have seen that the extracellular matrix plays an important role in the integrity of tissues and that this is impaired in certain pathologies. This study opens a new way to analyze pathologies and processes in the human body. An example of a possible future study could be the ripening, or softening, of the cervix (the lowerpart of the uterus) during delivery. The cervix tissue consists mainly of collagen, but the mechanism in which the initial stiff tissue transforms into soft tissue, enabling the infant to be delivered, is still unknown. This process is even more interesting because of its reversibility: within a few weeks after birth the collagen network is back in its original state.

Curriculum Vitæ

Jan Willem Maria Beenakker is geboren op 17 augustus 1984 in Leiden. In 2003 rondde hij de gymnasiumopleiding aan het Stedelijk Gymnasium Leiden af, waarna hij wis- en natuurkunde ging studeren aan de Universiteit Leiden. Nadat hij voor beide vakken het propedeuse diploma behaald had, vervolgde hij de studie natuurkunde en studeerde in 2008 cum laude af, waarvoor hij twee onderzoeksprojecten deed. Het eerste onderzoek betrof een samenwerking tussen de "Interface Physics" groep en de onderzoeksafdeling vaatchirurgie van het Leids Universitair Medisch Centrum. Onder de begeleiding van prof. dr. ir. T. H. Oosterkamp en dr. J. H. N. Lindeman bestudeerde hij de mechanische eigenschappen van de menselijke aorta met de atomaire-krachtmicroscoop (AFM) en verschillende optische technieken. Zijn tweede onderzoek vond plaats op het FOM instituut AMOLF te Amsterdam, waar hij onder de supervisie van prof. dr. G. H. Koenderink de dynamica van microtubili in een actine/myosine netwerk bestudeerde.

Na zijn afstuderen begon hij zijn promotieonderzoek aan de Universiteit Leiden als lid van de Interface Physics groep, waar hij, onder begeleiding van prof. dr. ir. T. H. Oosterkamp, de studie van zijn eerste onderzoeksproject voortzette. De resultaten van dit onderzoek staan beschreven in dit proefschrift.

Naast zijn promotieonderzoek, is Jan-Willem verantwoordelijk (geweest) voor verscheidene nationale en internationale projecten binnen de Gemeenschap Emmanuel, een internationale Katholieke vereniging. Hij is getrouwd en heeft één dochter.

List of publications

1. J. H. N. Lindeman, B. A. Ashcroft, J. W. M. Beenakker, M. van Es, N. B. R. Koekkoek, F. A. Prins, J. F. Tielemans, H. Abdul-Hussien, R. A. Bank and T. H. Oosterkamp. Distinct defects in collagen microarchitecture underlie vessel-wall failure in advanced abdominal aneurysms and aneurysms in Marfan syndrome.
   Proceedings of the National Academy of Sciences 107:862, 2010.

2. S. He, G. E. M. Lamers, J. W. M. Beenakker, C. Cui, V. P. S. Ghotra, E. H. J. Danen, A. H. Meijer, H. P. Spaink and B. E. Snaar-Jagalska. Neutrophil-mediated experimental metastasis is enhanced by VEGFR inhibition in a zebrafish xenograft model.
   Journal op Pathology, in press, 2012.

3. J. W. M. Beenakker, B. A. Ashcroft, J. H. N. Lindeman and T. H. Oosterkamp. Mechanical properties of the extra cellular matrix of the aorta studied by enzymatic treatments.
   Biophysics Journal, in press, 2012.

4. O. A. Ovchinnikova, L. Folkersen, J. W. M. Beenakker, J. Persson, J. H. N. Lindeman, T. Ueland, P. Aukrust, R. Hanemaaijer, N. A. Gavrisheva, E. V. Shlyakhto, G. Berne, P. S. Olofsson, U. Hedin, and G. K. Hansson. The collagen cross-linking enzyme lysyl oxidase is associated with a stable phenotype of human atherosclerotic lesions.
   In preparation, 2012.

Dankwoord

Tijdens mijn promotie heb ik het geluk gehad om met veel verschillende mensen te mogen samenwerken. Zonder hen was niet alleen dit proefschrift niet tot stand gekomen, zonder hun gezelligheid was ik deze vier jaren lang niet zo opgewekt doorgekomen.

Ik wil als eerste alle collega's van het LUMC bedanken voor hun gastvrijheid en geduld om mij als fysicus te ontvangen en de fijne kneepjes van het medische onderzoek te leren. In het bijzonder denk ik dan aan Adri Mulder, geweldig dat je tussendoor altijd nog tijd wist te vinden om snel een paar coupes te snijden of een nieuw protocol te proberen, Rogier van Dijk, door jou lukt het me nu eindelijk ook om coupes van verschillende stadia atherosclerotische plaques te "lezen", en Jos Onderwater en Annelies van der Laan, bedankt voor jullie vertrouwen en hulp bij het gebruik van de SEM en intravirale multi-photon microscoop! Zonder de hulp van Sandro Schaapherder, die voor ons het menselijke weefsel uit de kliniek verzamelde, had een groot deel van dit onderzoek nooit plaats kunnen vinden. Een bijzonder woord van dank wil ik richten tot Frans Prins: het was goed om te zien hoe jij je microscopen door en door kent en er ook aan durft te sleutelen.

Ook binnen het LION was de samenwerken altijd erg prettig. De technische ondersteuning van Fred Kranenburg, Dian van der Zalm, Gert Koning en Raymond Koehler stond er altijd voor garant dat zelfs de meest ingewikkelde wensen gerealiseerd konden worden. Voor bijna alle andere ondersteuning kon ik altijd bij Ellie van Rijsewijk terecht, of er nu een ticket geboekt moest worden of ik een obscuur medisch artikel uit de jaren 70 nodig had, Ellie wist het altijd te regelen. Ook wil ik de biofysica groep bedanken voor hun gastvrijheid wanneer ik weer eens wat ijs, 'n pipet of ultracentrifuge nodig had.

Dear Shunning and Ewa, thank you for inviting me to join your zebrafish experiments. Apart from learning many things from doing my first in vivo experiments, the measuring in the animal facility of the LUMC itself, has also been an unforgettable experiment. Olga thank you for the nice collaboration on the plaques project and your openness to try a relatively unknown technique like the AFM. Janneke en Annemieke, bedankt voor jullie enthousiasme en inzet om het onderzoek naar de atherosclerotische plaques op te zetten. Ik heb het erg gezellig gevonden om met jullie samen te mogen werken.

Tijdens dit onderzoek heb ik regelmatig verrijkende gesprekken gehad met fysici die vergelijkbare systemen vanuit een in vitro of theoretische hoek bekijken. De gesprekken met Kees Storm, Liesbeth Huisman en Gijsje Koenderink hebben me erg geholpen om de fysica van deze systemen beter te doorgronden. The stimulating discussions with Tony Cerami have also shaped the direction of this project. His biochemical view on things and eagerness to try new techniques really pushed this study forward. Karel, Willem en Guus, de gesprekken met jullie

als geneeskundige broer/zwagers, hebben me erg geholpen om de vertaalslag van de natuurkunde naar de geneeskunde te maken. Thomas, bedankt dat ik altijd met mijn, soms erg basale, scheikundige vragen bij je terecht kon en zonodig gelijk wat chemicaliën kon lenen.

Beste leden van de IP groep, jullie steun en gezelligheid zijn voor mij van grote waarde geweest, daarnaast hebben jullie ideeën me zeker geholpen om verder te komen in dit onderzoek. In het bijzonder wil ik Allard en Brian bedanken voor hun hulp bij het opzetten van dit project en Joost voor zijn frisse blik op de resultaten van dit onderzoek. Gert-Jan, de gesprekken bij de koffie waren voor mij altijd een leuke manier om de werkdag te beginnen. Federica, het was leuk om met jou de verantwoordelijkheid voor het bioafm-lab te delen e mi piaciuto parlare dell' origine Italiana che abbiamo in comune. Femke, Sander en Guocai, bedankt voor alle momenten samen in HL704, het was geweldig om met jullie de kamer te mogen delen. Ik wens jullie nog veel zegen bij het afronden van jullie promotie.

Jan, je openheid naar de fysische manier van denken en de wil om bestaande paradigma's te doorbreken, hebben ervoor gezorgd dat we de afgelopen jaren een hoop verschillende fysisch interessante ziektebeelden zijn tegen gekomen. Tjerk, bedankt voor je steun en vertrouwen om zelf de inrichting en koers van dit project te mogen bepalen.

Pappa en mamma, bedankt voor jullie onvoorwaardelijke aanmoediging en waardering voor alles wat ik doe. Loes, ik ben je heel dankbaar dat je me niet alleen hielp om door de dipjes in het onderzoek heen te bijten, maar ook dat ik de hoogtepunten met jou kon vieren en je je altijd interesseerde in wat ik nu precies aan het onderzoeken was. Chiara, dank je dat je thuis altijd vrolijk op me wacht als ik thuiskwam en dat je me helpt het werken los te laten.

Tenslotte, maar zeker niet op de laatste plaats, wil ik mijn dankbaarheid uitspreken ten aanzien van Degene die alles in allen mogelijk maakt, de Schepper, in wie wijsheid, waarheid en wetenschap samenkomen.

Dit dankwoord maakt geen deel uit van het proefschrift van J.W.M. Beenakker.